THE UNIVERSITY *of* EDINBURGH

The Physics and Chemistry of Gas in Discs

Ian Tilling

A thesis submitted in fulfilment of the requirements
for the degree of Doctor of Philosophy
to the
University of Edinburgh
April 2012

Abstract

Protoplanetary discs set the initial conditions for planet formation. By combining observations with detailed modelling, it is possible to constrain the physics and chemistry in such discs.

I have used the detailed thermo-chemical disc model ProDiMo to explore the characteristics of the gas in protoplanetary discs, particularly in Herbig Ae objects. I have assessed the ability of various observational data to trace the disc properties. This has involved a number of different approaches. Firstly I compute a series of disc models with increasing mass, in order to test the diagnostic powers of various emission lines, in particular as gas mass tracers. This approach is then expanded to a large multi-parameter grid of $\sim 10^5$ disc models. I have helped to develop a tool for analysing and plotting the huge quantity of data presented by such a model grid.

Following this approach I move on to a detailed study of the Herbig Ae star HD 163296, attempting to fit the large wealth of available observations simultaneously. These include new Herschel observations of the far-infrared emission lines, as well as interferometric CO observations and a large number of continuum data. This study addresses the topical issues of the disc gas/dust ratio, and the treatment of the disc outer edge. It explores the effects of dust settling, UV variability and stellar X-ray emission on the disc chemistry and line emission. There is possible evidence for gas-depletion in the disc of HD 163296, with the line emission enhanced by dust settling, which would indicate a later evolutionary stage for this disc than suggested by other studies.

Finally, I work to improve the treatment of the gas heating/cooling balance in ProDiMo, by introducing a non-LTE treatment of the atomic hydrogen line transitions and bound-free continuum transitions. I explore the effects of this on the disc chemical and thermal structure, and assess its impact in terms of the observable quantities.

Declaration

Except where otherwise stated, the research undertaken in this thesis was the unaided work of the author. Where the work was done in collaboration with others, a significant contribution was made by the author.

Acknowledgements

Firstly I would like to thank my supervisors Peter Woitke, Ken Rice and Wing-Fai Thi, whose help and support have been invaluable throughout my PhD studies, and without whom I could never have made it to this stage. I would also like to thank Inga Kamp for her collaboration, her advice and for her patience throughout. I also appreciate the help given to me by my other collaborators, and in particular would like to thank Christophe Pinte, François Ménard, Gwendolyn Meeus, Benjamin Montesinos, Gaspard Duchêne and Bill Dent for their useful comments and advice.

I would like to thank everyone at the Royal Observatory for making my time here so enjoyable, and for keeping my seat warm the rest of the time. I also acknowledge the Science and Technology Facilities Council (STFC) for giving me the opportunity to complete this PhD.

Thanks to my parents Steve and Lesley, my sister Rachel, and to all the friends in Edinburgh and elsewhere who have supported and humoured me throughout, regardless of whether or not they had any idea what “The Prof” was up to. Finally I would like to thank the members of Trapped Mice and Seneka for the music, memories, and for keeping me sane.

Contents

List of Figures

List of Tables

Chapter 1

Introduction

1.1 The Importance of Protoplanetary Discs

The search for life outside our solar system is surely one of our most exciting scientific endeavours. It is known already that at least 10% of nearby Solar-like stars harbour a planetary system [Fischer and Valenti, 2005], and every month the tally of detected exoplanets creeps upwards. The prospect of discovering a habitable Earth-like planet seems tantalisingly close, although the likelihood of this is still pure speculation. There are a number of criteria we think a planet would have to satisfy before the genesis of life. We believe it should lie in the "Goldilocks zone", with temperatures neither too hot nor too cold, and indeed just right for the accumulation of liquid water. Early life would also need to avoid the myriad hazards of a young planetary system, including harmful X-rays and ultra-violet (UV) radiation from the central star, as well as potential asteroid bombardment.

In order to begin to predict how frequently such life-friendly conditions might occur in our Galaxy and beyond, it is important to understand the process by which planetary systems form. Our current view of planet formation leaves many questions unanswered, but one way in which all contemporary models agree is that planets were born out of a disc of gas and dust orbiting young stars (see Fig. 1.1). Such "protoplanetary discs" are a key feature in our picture of star formation, surviving for around ten million years in the crucial intermediate phase between the initial collapse of a molecular cloud to form the star, and the eventual formation of a stable planetary system [Hartmann, 1998].

Protoplanetary discs are characterised observationally by an excess emission in the

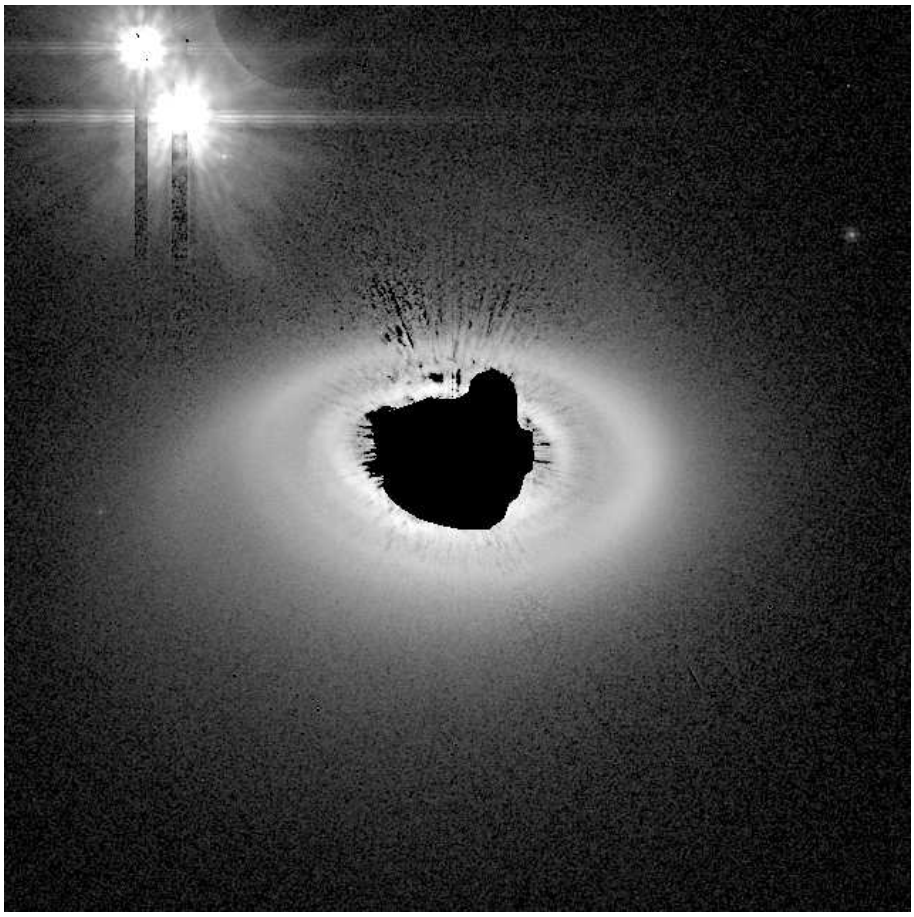

Figure 1.1: HST ACS optical image of the dust disc around the star HD 141569A. This is a young, 5 million year old object which appears to be part of a triple-star system. The disc exhibits a tightly wound spiral structure, and there is evidence that this is associated with the nearby binary system (HD 141569BC) [Clampin et al., 2003].

infra-red (IR) over that which would be expected from the stellar photosphere (see Fig. 1.2). Early disc models [Lynden-Bell and Pringle, 1974, Shakura and Syunyaev, 1973] predicted such emission as a natural consequence of warm dust in the discs, heated at the disc surface by stellar radiation, and from within by viscous dissipative processes.

One way to gather information about the structure of such discs is to analyse this dust emission, and compare it to that predicted by computational models. While dust observations alone can give us some insight into the physical conditions around young stars, a much more powerful option is to couple these with observations of the gas in discs. The warm, bright conditions in protoplanetary discs lead to a rich and complex chemistry, and the various chemical species can be studied through line emission to build up a detailed picture of the disc composition. This is technically quite demanding, requiring extensive chemical and thermal modelling of the discs in order to predict the extent to which the various observational signatures should be detected. At present there have been many large-scale surveys of the dust content of discs, but the gas content is less well-understood. This is despite the gas mass in discs dominating over the dust mass by a factor of 100 or more. Figure 1.2 gives an example of the combined modelling of gas and dust in discs. It predicts both the thermal dust emission and the gas line emission from a specific object, and these can be compared with observations of that object in order to constrain the disc properties.

One important property is the amount of gas present in the disc at different stages in its evolution, from an initially gas-rich disc through to a gas-poor debris disc. Knowledge of the disc gas mass can help to distinguish between different planet formation models, but it is currently unclear to what extent the observed gas emission lines can be used to infer the gas mass. It is clear that the “inversion” of observable quantities to yield the disc properties requires a detailed understanding of the physical processes at work in the disc, and the conditions under which the observed emission is formed. Observations of atomic and molecular emission lines with a new generation of instruments, coupled with detailed thermo-chemical disc modelling, allow us to vastly improve our understanding of the composition of discs, and therefore constrain current models of planet formation.

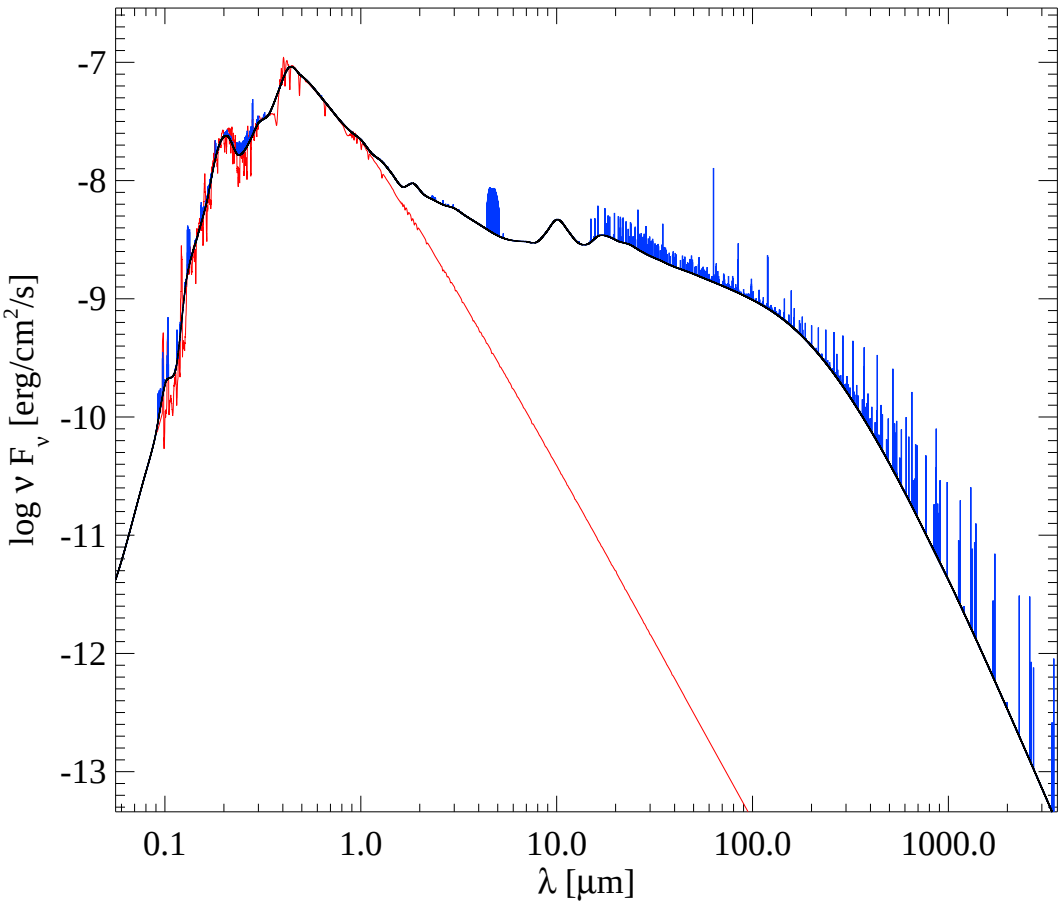

Figure 1.2: Synthetic Spectral Energy Distribution (SED) from the young Herbig Ae star HD 163296, highlighting the excess emission arising from the circumstellar disc (black line) relative to the stellar spectrum (red). The gas emission lines from the disc are shown in blue.

1.2 Thesis Outline

In this thesis, I use detailed disc modelling to attempt to improve our understanding of the physical and chemical processes which determine the emission we see from discs. This involves a number of different approaches, with a common aim to assess the power of observations to accurately probe the disc properties.

In Chapter 2 I summarise the major developments in disc modelling which are relevant to the work described in this thesis, and outline the key observational studies which have led to our current understanding of disc structure. In Chapter 3 I describe the key features of ProDiMo, a thermo-chemical disc code which has been used as the basis for the modelling carried out in the following work.

Chapter 4 uses ProDiMo to assess the diagnostic power of various gas emission lines, in particular attempting to determine the extent to which the line emission can probe the gas mass present in the disc. I compute a series of models with increasing gas mass, to see if it is possible to infer the mass from the predicted line emission. In Chapter 5 this approach is expanded to a large multi-parameter study, in which a grid of ~ 300000 models spanning parameter space is computed, in order to seek trends in the observable quantities, and so attempt to infer the disc properties from observations.

In Chapter 6 I turn my attention to a single object, the Herbig Ae star HD 163296. I attempt simultaneous model fits to the large wealth of available data for this object, in order to derive the disc properties.

In Chapter 7 I describe developing work in which I examine the impact of introducing the bound-free continuum and bound-bound line transitions of atomic hydrogen as heating and cooling processes, and the effect this has on the disc thermal and chemical structure. The overall conclusions from this thesis are summarised in Chapter 8.

Chapter 2

A Review of Protoplanetary Disk Studies

In this chapter I explore and summarise previous efforts to further our understanding of circumstellar discs. I outline the development of disc modelling towards its current state, as well as the key observational evidence which underpins our current picture of protoplanetary discs.

2.1 Disc Modelling

It has long been of interest to model circumstellar discs, from their formation through to eventual planetary systems and debris discs. As a protostellar cloud collapses a shock wave is formed causing the initially supersonic in-falling gas to thermalise and find itself in hydrostatic equilibrium in the midplane. Any initial net angular momentum of the collapsing molecular cloud will be conserved during collapse, resulting in a flattened disc structure [Hartmann, 1998].

Since the 1970s astronomers have been interested in the evolution of these circumstellar discs. Early models by Lynden-Bell and Pringle [1974] and Shakura and Syunyaev [1973] treat the matter in the disc as evolving through viscous accretion. In a disc with matter in Keplerian rotation, there is a natural velocity gradient between matter in adjacent orbits. This coupled with some form of viscosity causes angular momentum to be transferred outwards through the disc, while the matter in the disc accretes inwards, eventually falling onto the central star.

The exact nature of this viscosity is unclear even today, and current models often

utilise the 'α-viscosity' of Shakura and Syunyaev [1973], where the viscosity in a steady (constant accretion rate, $\dot{M}$) disc is given by $\nu = \alpha c_s H$. Here c_s is the sound speed in the disc, H is the disc scale height and $\alpha << 1$ is a parameter which determines the efficiency of angular momentum transport.

Using this formalism, as well as the assumption of a thin disc, Lynden-Bell and Pringle [1974], and later Pringle [1981] were able to determine analytic expressions describing the evolution of the disc density distribution with time. The thin disc approximation assumes that $H << R$ at all radii, so that the disc can be described by a vertically-integrated surface density, $\Sigma(R)$. This was found to evolve according to a viscous diffusion equation, with self-similar solutions for the disc structure.

At early stages of disc evolution matter is accreted through the disc, dissipating its gravitational potential energy as it is processed at smaller and smaller radii. This heats the disc, and at early stages forms the main source of power for the emitted disc SED. Pringle [1981] calculated analytically the shape of the emitted spectrum for a disc heated internally by viscous dissipation.

At later stages $\dot{M}$ falls off, and the disc heating becomes dominated by radiation from the central star. Circumstellar discs are characterised by emission in the infra-red in excess of that expected from the stellar photosphere. In addition, the SED shape of this excess emission is flatter than the $\lambda^{-4/3}$ dependence predicted by thin disc models [Rydgren and Zak, 1987]. This led Kenyon and Hartmann [1987] to propose a "flared" disc structure, whereby the disc scale height increases with radius. This allows the disc to be heated more efficiently by stellar radiation than for a thin disc, and SEDs calculated from such models are able to reproduce observations. Other models, such as those by Adams et al. [1987] had to resort to large dusty discs with larger mass then expected in order to explain the IR excess.

Chiang and Goldreich [1997] developed semi-analytical models for such "passive" discs where the disc heating is dominated by stellar irradiation. They utilised an optically thin surface layer of "superheated" dust grains which regulate the interior temperature of the disc. With this simple two-layer model, they again found that disc heating causes the disc to flare, which in turn leads to more efficient irradiation and further flaring, reproducing the observed SED slope in the IR.

While early disc models treated discs as being geometrically thin, with their properties expressed as functions of radius alone, the thin disc approximation is inherently limited when trying to probe the detailed disc structure. By considering

the disc properties (temperature, density, ionisation etc.) as a function of height, z, we open up a plethora of potential observational diagnostics to constrain the structure and composition of the disc.

Studies such as those of D'Alessio et al. [1998] and Bell et al. [1997] have attempted to model the detailed vertical structure of circumstellar discs. This is achieved by solving the equations of pressure balance coupled to the equations of radiative transfer. D'Alessio et al. [1998] considered a disc heated both by viscous dissipation and by irradiation from its central star. The gas and dust in the disc was assumed to be well mixed and thermally coupled, so that the gas temperature T_g and dust temperature T_d are equal at any given location in the disc. They found that stellar irradiation was the dominant heating agent except for in the inner disc ($R < 2$AU). By comparing an irradiated model disc to the purely viscous case, they found that the irradiated disc had a flatter temperature distribution with radius in both the midplane and photosphere, $T \propto R^{-1/2}$, as well as a smaller surface density Σ at given radius. Stellar irradiation also had the effect of stabilising the disc against gravitational perturbations, increasing the Toomre criterion to a value $Q = \frac{c_s \Omega}{\pi G \Sigma} > 1$. Here c_s is the gas sound speed, Ω the Keplerian angular frequency and Σ the disc surface density. One weakness of the D'Alessio et al. [1998] model is the assumption of thermal coupling between gas and dust. The disc photosphere, where most of the stellar radiation is absorbed, has low pressure and density, and so coupling should not be very efficient. Chiang and Goldreich [1997] commented that one should allow for different gas and dust temperatures when considering processes such as molecular line emission, and this is something that will prove key to my project.

Another weakness of these models [D'Alessio et al., 1998, Bell et al., 1997] is their simplified treatment of radiative transfer, which uses the frequency-integrated moment equations in the Eddington approximation with Planck and Rosseland-mean opacities. Indeed, D'Alessio et al. [1998] found the temperature in the upper disc atmosphere to be very sensitive to the assumed values of mean opacity. The reason for this simplification is that solving the full angle and frequency-dependent radiative transfer equations was (and still is, to a lesser extent) a challenging technical problem.

The Eddington approximation assumes isotropic frequency-independent scattering. From the radiative intensity J one can define the angle-integrated moments of radiation, H (first moment) and K (second moment). The Eddington approximation assumes a constant value for the "Eddington factor", $f = 1/3$, such that $K = f \times J = J/3$.

This approximation makes it far easier to solve the radiative transfer, but is valid only in the diffusion regime where $\tau >> 1$. Care should be taken when attempting to apply the Eddington approximation under standard disc conditions. An improved version of this treatment was utilised by Malbet et al. [2001]. The Variable Eddington Factor method calculates the Eddington factors on the fly, as a function of height z, as opposed to assuming one constant value. This allowed Malbet et al. [2001] to solve the angle-dependent transfer problem (instead of assuming an isotropic radiation field), giving analytical formulae for the disc temperature distribution as a function of optical depth, τ. They assumed a radial distribution given by a modified version of the analytical Shakura and Syunyaev [1973] formulation, and used this coupled with their radiative transfer calculations to give two-dimensional maps of temperature, pressure and density in the disc. From these they computed predicted SEDs and high resolution images for comparison with observations, although they didn't perform these comparisons themselves.

While Malbet et al. [2001] took the step of including angle-dependent radiative transfer calculations (albeit simplified) in their models, they were still reliant on "grey" mean opacities. The actual dust opacities in discs are known to vary considerably with frequency, and Dullemond et al. [2002] went one better than previous studies by including full frequency and angle-dependent radiative transfer. They computed the vertical temperature and density structure of passive (i.e. negligible heating by viscous dissipation) irradiated discs around T Tauri and Herbig Ae/Be stars. They found that the full radiative transfer treatment gave a lower midplane temperature over most of the disc when compared to the previous moment equations treatment, a difference of up to 70%. The frequency dependent opacities had more of an effect on the results than the inclusion of angle-dependent radiative transfer, leading Dullemond et al. [2002] to conclude that it is OK to employ the Eddington approximation as long as frequency-dependent opacities are used. Malbet et al. [2001] argue that it is important to consider the detailed vertical structure when interpreting disc SED observations, as opposed to the practice of using ad-hoc power laws to extract surface density, scale height etc. from the data. Dullemond et al. [2002], however, find that their more sophisticated radiative transfer treatment has only a minor effect on the predicted SED when compared to more basic models. This is despite the differences in internal structure. Their SED results are similar even to those of Chiang and Goldreich [1997], with their analytical disc models. Dullemond et al. [2002] conclude that it is

not possible to learn much about the vertical structure of a passive disc from its SED alone, and suggest than molecular line emission would be a better probe of the vertical temperature and density structure.

Dullemond et al. [2002] computed predicted line fluxes and line profiles for CO, ^{13}CO and C^{18}O as a way of determining the vertical temperature profile, as these species probe successively deeper disc layers. Their treatment was illuminating as a first order approximation, however the assumptions used would preclude the use of their results when interpreting real observations. They assumed a flaring disc shape, with the disc illuminated by its star at all radii, ignoring any self-shadowing effects due to a puffed-up inner rim etc. Also they assumed constant chemical abundances throughout the disc, ignoring various microphysical processes which would affect the abundances of their species (e.g. photodissociation, chemical freeze-out on grains). In order to compute line transfer results for comparison with observations, it is desirable to obtain a disc model where all (or much) of the microphysics, such as chemistry and gas energy balance, is considered.

2.2 PDR Modelling

The low-density, irradiated disc surface, where most of the spectral lines form, resembles photon dominated regions or photodissociation regions (PDRs), which are responsible for many emission characteristics of the ISM. PDRs are traditionally defined as regions where hydrogen-non-ionising far-ultraviolet photons (FUV, $6 < h\nu < 13.6$ eV) from stellar sources control the gas heating and chemistry. Ionising radiation is assumed to be absorbed in a narrow ionisation front between a H II region and a PDR. PDRs are cooled via atomic and molecular line emission from the gas component, and by continuum emission from dust. There are a number of specific mechanisms by which the gas is heated. These include photoelectric emission from grains, triggered by absorption of FUV photons. Photoelectric heating is also provided by polycyclic aromatic hydrocarbons (PAHs), which at present are treated simply as microscopic dust grains, although their precise role is far from understood [Shaw, 2006, Geers et al., 2009]. Other sources of gas heating are turbulence, cosmic ray heating and chemical heating.

The chemical structure of the gas in a PDR is determined largely by the FUV intensity. At low visual extinction A_V into the cloud, the high FUV intensity induces

ionisation and photodissociation reactions. At larger optical depth where the FUV intensity drops off, more complex species can be formed without being destroyed immediately by FUV photons. This produces the classic layered structure of PDRs, with transitions H $\rightarrow$ H_2 and $C^+ \rightarrow C \rightarrow CO$ with increasing A_V [Hollenbach et al., 1971, Glassgold and Langer, 1975]. This in turn affects the cooling. At low extinctions, the gas is cooled by emission of atomic fine-structure lines, mainly [O I]63μm and [C II]158μm. At larger depths molecular rotational line cooling in the millimetre, sub-millimetre and far infra-red becomes important (CO, OH, H_2,H_2O etc).

In order to model a PDR it is necessary to compute all relevant local properties of the cloud such as the gas and dust temperature, gas pressure, relative abundance of each chemical species and their level populations, dust composition, as well as the local radiation field. The local wavelength-dependent radiation intensity affects the gas and dust heating, photochemical reaction rates, and molecular excitation levels. It is coupled in general to remote parts of the cloud, and depends on the integrated absorption (again wavelength-dependent) along different lines of sight to the local position. This non-local coupling makes numerical PDR calculations computationally expensive.

In order to solve for the chemical abundances throughout a PDR, it is necessary to amass a database of astrochemical reactions, with rates for reactions between the various species in the chemical network. One such database is the UMIST 2006 compilation [Woodall et al., 2007]), which contains data for 420 species, including 4573 chemical reactions. For gas-phase reactions the rate coefficients are parameterised as functions of temperature, in an Arrhenius law. The database also includes photoreactions, cosmic-ray ionisation and cosmic-ray-induced photoreactions (see Chapter 3). The rate coefficients are obtained from various sources, for instance from direct laboratory measurement or theoretical calculation, and come with an estimate of their accuracy. This is a valuable tool when attempting to model chemical networks, although care should be taken when applying the rate coefficients outside ISM conditions. Each reaction has a temperature range for which the given formula is valid, and conditions in a protoplanetary disc may well fall outside of this range. It is also important to consider non-gas-phase processes such as grain chemistry.

The majority of PDR models feature plane-parallel geometry, illuminated either from one side or both sides, and either isotropically or with directed light perpendicular to the slab. The latter case simplifies the problem by considering a single line of sight

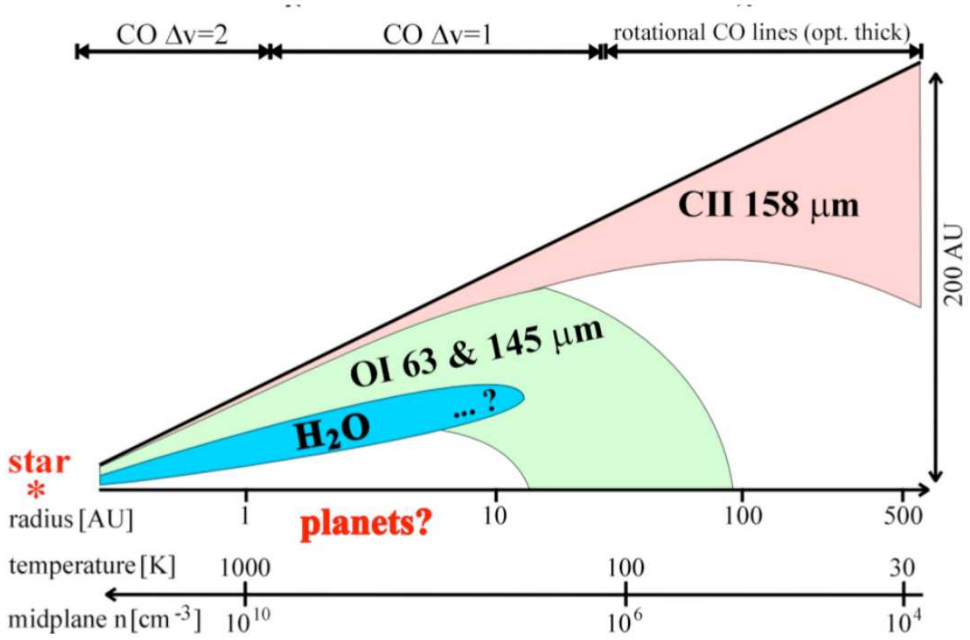

Figure 2.1: Schematic diagram of a circumstellar disc, showing the dominant observable gas lines in the various disc regions, and typical gas temperatures and densities at each disc radius.

[Flannery et al., 1980]. Another common geometry employed is the spherical case, and there are also a number of specialist PDR models employing disc geometry. A schematic diagram for the disc geometry case is shown in Figure 2.1, illustrating the typical PDR transition from ionised gas in the disc surface layer, through to atomic and molecular gas at progressively greater depth. This stratification allows us to probe conditions in different disc regions by observing the various gas emission lines (see Figure 2.1).

Röllig et al. [2007] carried out a comparison of 11 different PDR codes, in an attempt to determine their agreement under various benchmark settings. The codes were designed for a wide range of specific applications, with different treatments and priorities (e.g. model geometry, detailed microphysics versus computational speed). Even so, the models were all in reasonable agreement after benchmarking, with a couple of exceptions for the more ‘extreme’ conditions. There was some uncertainty in the temperature profiles at low density and high UV intensity, where the tenuous ionised gas can be sensitive to the assumed values of rate coefficients etc. Also there was some uncertainty in the H_2 density profile at high density, where the large optical

depth requires long integrations when calculating the radiative transfer and so can be computationally expensive.

2.3 Thermo-chemical Disc Modelling

Thermo-chemical Disc Models are a class of protoplanetary disc model where the detailed microphysics are computed, with a view to calculating the chemical and physical composition of the gas and dust in a disc. The main improvement on previous models is in modelling the disc properties in 2D, as opposed to approximating the disc as a 1D structure with discrete layers. By modelling the chemical abundances along with the temperature and density distribution, it is possible to predict the level populations of the various chemical species in order to carry out line transfer calculations for comparison with atomic and molecular emission line observations. This has vast potential for probing the internal structure and dynamics of discs, to a far greater extent than offered by dust continuum modelling. The ultimate aim is to obtain a set of diagnostic gas emission lines such that observed disc spectra can be inverted to reliably infer the disc composition, mass, temperature profile etc.

Najita et al. [2007] reviewed some of the developments in modelling the gas in circumstellar discs, with particular reference to the inner disc ($R < 10$AU) where planets are likely to form. Indeed, the inner disc is a potentially fertile pasture for the study of planet formation, since the lifetime of gas in the inner disc places an upper limit on the timescale for planet formation. Also the amount of residual gas in the terrestrial planet region may help define the final mass and eccentricity of such planets, and so could affect the likelihood of finding solar systems like ours. The inner disc is difficult to model due to its high temperature and density, as well as uncertainties in the truncation of gas and dust at the inner radius. The inner disc is also too small to resolve spatially for systems of interest, although differential rotation can be utilised to study discs using high resolution spectroscopy.

Najita et al. [2007] stress that while some conclusions can be drawn directly from observational data combined with simple spectral synthesis modelling, harnessing the full diagnostic potential of disc observations will likely rely on detailed models of their thermal and chemical structure.

A popular simplification is to adopt a specified density distribution, and to solve the chemical rate equations assuming a vertically isothermal disc. An improved method

(see Section 2.1) removes the assumption of vertical isothermality and calculates the vertical thermal structure of the disc including viscous accretion heating and stellar radiative heating under the assumption that the gas and dust temperatures are the same [Calvet et al., 1991, D'Alessio et al., 1999]. From about 2001 onwards, theoretical models showed that the gas temperature can become much larger than the dust temperature in the disc atmosphere [Kamp and van Zadelhoff, 2001, Glassgold and Najita, 2001], suggesting the need to treat gas and dust as two independent but coupled thermodynamic systems.

There are a number of recurring questions hanging over the field of thermo-chemical disc modelling. One of these is the treatment of chemistry. Our knowledge of astrochemistry is based mainly on the ISM, whereas disc conditions are significantly warmer and more dense. It is also not obvious how much of an effect grain evolution in discs has on the grain chemistry, or to what extent vertical and radial mixing affects the distribution of the different chemical species. The dust and gas heating and chemistry are strongly dependent on the stellar UV flux, and the data for this are currently quite sparse, with a need for more measurements as a function of stellar age and evolutionary state. It is important to use realistic fluxes in the FUV band (912 - 1100 Å) where C can be photoionised and CO and H_2 photodissociated. It is currently a matter of debate whether stellar FUV or X-rays dominate the ionisation, chemistry and heating in the gas [Meijerink et al., 2008]. This is important due to the difference in photon energy. FUV photons are unable to ionise H, and are absorbed much more readily by dust than X-rays.

Kamp and Bertoldi [2000] developed a thermo-chemical disc model in order to investigate CO in the circumstellar discs of Vega and β Pictoris, the most prominent A stars with gas discs. CO radio line observations by Zuckerman et al. [1995] of A stars had failed to detect CO in these stars, suggesting that the gas was dissipated over a timescale less than 10^7 years, not long enough to form a Jupiter-like planet. In order to try and explain this apparent gas underabundance, Kamp and Bertoldi [2000] used a simple thin hydrostatic disc model with a specified density distribution, with the coupled dust and gas temperatures from radiative equilibrium with the stellar photospheric UV flux. They used a chemical network with 47 species linked by 260 reactions. Their chemical modelling showed that photodissociation by stellar UV can destroy CO, with the extent of this strongly dependent on the disc mass. In Vega the CO is completely dissociated, suggesting this is not a suitable gas tracer in this

case. In the more massive β Pictoris disc, the stellar UV field alone was unable to dissociate all of its CO, although by adding an isotropic ISM UV field Kamp and Bertoldi [2000] were able to reproduce the observed CO underabundances. They also recognised that the midplane temperature dropped below 20K, the critical temperature at which CO molecules start to freeze-out on grains. This could provide another source of CO depletion. These results indicate that the non detection of individual molecular lines does not necessarily imply a general gas depletion.

Hersant et al. [2009] is another example of disc modelling being used to study CO, although this time to try and explain the opposite problem: the presence of gas-phase CO below its freezing temperature. Millimeter interferometric observations of several circumstellar discs around T Tauri stars revealed that large amounts of CO remained gaseous at these temperatures, as low as 10K. This suggested that some non-thermal desorption process was acting to remove CO from grains and replenish the gas-phase CO. Hersant et al. [2009] investigated two of these processes: turbulent mixing and photodesorption. They used a simple disc model with all parameters expressed as radial power laws. The vertical temperature distribution was given two distinct layers, a cold midplane layer with $T = 10$K and a warm upper layer in radiative equilibrium with the central star. The chemical evolution was calculated using a one-dimensional vertical time-dependent model run for 10^5 years. This was repeated with and without photodesorption and turbulent mixing, where the latter was implemented using a vertical viscous diffusion equation. Hersant et al. [2009] found that photodesorption significantly enhances the gas-phase CO abundance when the visual extinction, $A_V < 5$, whereas turbulent mixing had only a minor effect on its abundance. This would seem to suggest photodesorption as the likely source of gas-phase CO at $T < T_{\rm freeze}$, although the resulting dependence of column density, N, on radius was not consistent with observations. Their results were also sensitive to the choice of transition height between the warm and cold layers, suggesting a more sophisticated model is needed in order to reliably explain the presence of this cold gas-phase CO.

Kamp and Dullemond [2004] computed disc models where the gas and dust temperatures were allowed to decouple, and the gas temperature T_g computed in a self-consistent manner, featuring detailed heating and cooling mechanisms from PDR modelling. These included photoelectric heating, dissociative heating, dust-gas thermal heat exchange and line cooling. They found that the gas and dust temperatures

were equal to within 10% in the surface region where the dust continuum emission features are produced. High above the disc, however, T_g increased above T_d, as high as $\sim 10^4$K in the inner disc. Kamp and Dullemond [2004] concluded that in order to accurately determine the thermal behaviour of the disc gas when allowed to decouple from the dust, it was necessary to develop models with self-consistent disc structure, where the structure and gas temperature determination are solved iteratively.

ProDiMo [Woitke et al., 2009a,b] is a high-level radiation thermo-chemical disc model where the disc structure is solved iteratively with the 2D radiative transfer, chemistry and thermal balance in order to give fully self-consistent models. ProDiMo is used extensively throughout this thesis, and the features most relevant to this work are outlined in Chapter 3. Firstly, however, I will review the key observational studies which have shaped our current understanding of discs, and their gas.

2.4 Disc Observations

In 1985 IRAS observations yielded the first indication of the presence of circumstellar matter around A-type stars. Aumann [1985] reported a significant infra-red excess in the two bright stars Vega and β Pictoris, and this has been widely interpreted as coming from circumstellar dust which is heated by stellar radiation to temperatures of order 100K. Many disc models have made predictions about the nature of this excess SED emission, or otherwise attempted to fit existing observations [Lynden-Bell and Pringle, 1974, Kenyon and Hartmann, 1987]. Calculations in general give clear IR signatures, underpinning continuum observations. Strom et al. [1989] used IR excess emission to infer the presence of circumstellar discs around 60% of the youngest pre-main sequence stars in their sample.

Beckwith et al. [1990] carried out a survey for circumstellar discs around young stellar objects (YSOs). Their continuum observations at 1.3mm in the Taurus-Auriga dark clouds indicated that 42% of objects have detectable emission from small particles. They calculated dust masses in the range $10^{-5} < M_{\rm dust} < 10^{-2}$ M$_\odot$. The dust-to-gas ratio is usually assumed to have a value of 0.01, giving disc masses of $10^{-3} < M_{\rm disc} < 1$ M$_\odot$. By observing stars with different ages, Beckwith et al. [1990] concluded that $M_{\rm disc}$ doesn't decrease with increasing stellar age up to at least 10^7 years. However, care should be taken when trying to determine disc masses from continuum observations. Discs are opaque for $\lambda < 100\mu$m, meaning infra-red and

visible continuum emission are insensitive to $M_{\rm dust}$, and are suitable for probing only the surface temperature structure of discs. Dust emission is however optically thin for $\lambda \sim$ 1mm, hence proportional to the dust column density, and so should be a good way to measure dust mass (though not necessarily gas mass). One problem with this method, however, is its reliance on an assumed dust opacity at mm wavelengths, whereas in reality this can be a strong function of dust composition, grain size etc.

Other observational signatures can indicate the presence of a circumstellar disc. Discs can shield receding portions of stellar mass loss from view, giving preferentially blue-shifted lines [Reipurth et al., 1996]. Also anomalously large extinction may be observed for discs seen edge-on [Schneider et al., 2012], as well as asymmetrical scattering of visual and near infra-red from stars, and large degrees of polarisation of starlight [Min et al., 2012].

In general SED fits are unable to give a unique solution for the temperature and density structure of a disc. There are typically a number of configurations of dust distribution, composition, grain size etc. that are able to fit an SED. One robust result however is the presence of high temperature dust in the surface layers of discs, suggesting more efficient stellar irradiation than for a thin disc. This has been interpreted as evidence for a common flaring disc shape [Kenyon and Hartmann, 1987]. In order to probe the inner layers of a disc it is desirable to observe molecular line transitions. By observing lines that become optically thick at different heights in the disc, it is possible to constrain the vertical temperature and density structure independently. Also high resolution spectra can yield positional information through interpretation of line profiles.

van Zadelhoff et al. [2001] observed the sub-mm lines of CO, HCO^+ and HCN from discs around low mass pre-main sequence stars, up to the J=6-5 transition in CO and J=4-3 in HCO^+ and HCN. By interpreting the ratios between various line fluxes, and the $\tau = 1$ surfaces of the lines, van Zadelhoff et al. [2001] proposed that most of the observed line emission originated in an intermediate disc layer in the outer disc regions, with moderately warm temperature and density $n = 10^6 - 10^8$ cm^{-3}. The ^{13}CO isotope lines were optically thin and so capable of probing the cold disc midplane, unless these molecules are frozen out completely. The computed molecular abundances indicated large depletions compared to dark cloud abundances, > 100 in some cases. This suggests a significant freeze out of all the observed species at $T <$ 22K. Depletions were also observed in the warm upper layer, due to photodissociation

by stellar and interstellar UV (see Section 2.3). The highest depletions were observed in the active X-ray and UV star TW Hya.

A more ambitious study was carried out by Thi et al. [2004], using single dish millimetre and sub-mm observations to search for various transitions around two T Tauri and two Herbig Ae stars. Some more complex molecules were included in the study, with H_2CO lines found towards one star, however there were no detections for CH_3OH, SO and CS. As for the van Zadelhoff et al. [2001] study, a lower species abundance was observed than in the envelope around a low mass protostar (IRAS 16293-2422), suggesting depletion due to freeze-out on grains (in the midplane) and photodissociation (in the upper layers). Thi et al. [2004] propose that studying the similarities and differences between discs and protostellar envelopes can allow us to constrain chemical models. They also suggest comparison with comets, as these could give a chemical record of the primitive sola nebula due to spending most of their time in the cold outer regions of the Solar System.

Thi et al. [2004] analysed the line profiles of the various lines to yield information about the disc structure. Disc size estimates were obtained from model fits to the ^{12}CO J=3-2 line profiles. This profile was observed to be double peaked for three of the objects, with velocity width $\sim$ 2km/s, interpreted as discs undergoing Keplerian rotation viewed at an inclination angle *i*. The fourth object, TW Hya, had a single Gaussian line profile for the ^{12}CO J=3-2 line, indicating a disc seen face-on. The absence of any extended velocity wings in the profiles suggests that no molecular outflows are present in any of the objects. Mean kinetic temperatures were estimated from the line ratios. For instance, the ^{13}CO J=3-2/1-0 ratio of 1.35 $\pm$ 0.4 gave a temperature $T_k \sim 20 - 40$K, assuming both lines were optically thin. Thi et al. [2004] noted that the detection of molecules in discs is often hampered by the small size of a disc compared to the beam size of a single dish telescope. Also the total amount of material present is small (a few $\times 10^{-2} M_\odot$ at most), and so observations are limited to the most abundant species.

Piétu et al. [2007] carried out sub-arcsecond CO observations of the low transition millimeter lines. They found evidence for a vertical temperature gradient in two of their three objects. The data were fitted to a simple disc model where all parameters were expressed as power laws in *R*, in order to try and constrain the disc parameters. They justified the use of this ad-hoc model, without any dependence on height, *z*, by the limitations of current sub-mm and millimeter arrays, although this will be rectified

by upcoming instruments e.g. ALMA.

Chapter 3

ProDiMo

3.1 Introduction

ProDiMo (Protoplanetary Disc Model, Woitke et al. 2009a,b) is a radiation thermo-chemical disc model, based on the models of Inga Kamp [Kamp and van Zadelhoff, 2001, Kamp and Dullemond, 2004]. It improves on previous models by including an option to calculate the disc structure fully self-consistently. ProDiMo uses the solution of radiative transfer, chemistry and thermal balance to in turn determine the new gas sound speeds and adjust the hydrostatic disc structure accordingly. These global iterations allow the fully consistent calculation of the physical, chemical and thermal structure of the gas in protoplanetary discs. Another major improvement of this model is the inclusion of additional high density/high temperature heating and cooling processes. These are relevant to the inner part of the disc, where the conditions are analogous to those in the tenuous atmospheres of cool stars. This allows the models to extend closer to the star and include modelling of the disc inner rim.

The model iterates through the calculations of 2D dust continuum radiative transfer, solution of the chemical network, calculation of heating and cooling balance, before re-calculating the hydrostatic disc structure.

I have used ProDiMo extensively for the modelling efforts described in later chapters. I have also modified the code, introducing the bound-bound and bound-free continuum transitions of atomic hydrogen as a high temperature heating and cooling process. The approach I have adopted for these improvements is described in Section 3.6, but first I will briefly outline the core methods used in ProDiMo.

3.2 Hydrostatic Disc Structure

The disc is modelled as being in vertical hydrostatic equilibrium in axial symmetry, with Keplerian rotation about the z-axis. This ignores the effect of self-gravity, and assumes the radial pressure gradient is small compared to the centrifugal acceleration and gravity. The vertical component of the equation of motion is then given by

$$\frac{1}{\rho}\frac{dp}{dz} = -\frac{z\,G\,M_\star}{(r^2+z^2)^{3/2}} \tag{3.1}$$

which can be integrated from the midplane upwards by substituting $p = c_T^2\rho$, and assuming the isothermal sound speed c_T is a known function of z. The density results are then scaled to achieve the desired column density at distance r

$$\Sigma(r) = 2\int_0^{z_{max}(r)} \rho(r,z)dz \tag{3.2}$$

ProDiMo assumes a power law distribution of the column density, $\Sigma = \Sigma_0 r^{-\epsilon}$ for the main part of the disc, where ϵ is specified as program input, and Σ_0 is determined from the specified disc mass $M_{\rm disc}$:

$$M_{\rm disc} = 2\pi\int_{R_{\rm in}}^{R_{\rm out}} \Sigma(r)\,r\,dr \tag{3.3}$$

Due to the artificial nature of an abrupt cutoff in density at $R_{\rm in}$ and $R_{\rm out}$, the model has the option to employ ‘soft edges’, where the density cutoff is smoothed in a manner consistent with angular momentum conservation at such a boundary.

3.3 Continuum Radiative Transfer

The local continuous radiation field $J_\nu\,(r,z)$ determines the local dust temperature $T_{\rm d}\,(r,z)$, which in turn affects the heating and cooling balance through gas-dust collisions, as well as the grain surface chemistry. J_ν itself determines the photo-chemical reaction rate (e.g. photodissociation, photoionisation), as well as the rate of photoelectric heating. J_ν also affects the level populations in the statistical equilibrium calculations, through the escape probability method (see Section 3.5.1).

The radiative transfer is solved at each grid point in the disc by tracing 153 rays

backwards along the direction of photon propagation, while solving the radiative transfer equation,

$$\frac{dI_\nu}{d\tau_\nu} = S_\nu - I_\nu, \tag{3.4}$$

assuming LTE and coherent isotropic scattering,

$$S_\nu = \frac{\kappa_\nu^{\rm abs} B_\nu(T_{\rm d}) + \kappa_\nu^{\rm sca} J_\nu}{\kappa_\nu^{\rm ext}}. \tag{3.5}$$

Here, I_ν is the spectral intensity, $J_\nu = \frac{1}{4\pi}\int I_\nu d\Omega$ the mean intensity, S_ν the source function, B_ν the Planck function, and $\kappa_\nu^{\rm abs}$, $\kappa_\nu^{\rm sca}$ and $\kappa_\nu^{\rm ext} = \kappa_\nu^{\rm abs} + \kappa_\nu^{\rm sca}[{\rm cm}^{-1}]$ are the dust absorption, scattering and extinction coefficients respectively. The dust at a given grid point has a unique temperature $T_{\rm d}$ in modified radiative equilibrium,

$$\Gamma_{\rm dust} + \int \kappa_\nu^{\rm abs} J_\nu d_\nu = \int \kappa_\nu^{\rm abs} B_\nu(T_{\rm d}) d\nu \tag{3.6}$$

where the additional heating rate $\Gamma_{\rm dust}$ accounts for non-radiative heating and cooling processes such as thermal accommodation with gas particles. An accelerated Λ-iteration scheme is used to achieve converged results for $J_\nu(r,z)$ and $T_{\rm d}(r,z)$.

The ray directions are chosen such that there are more rays pointing towards the hot inner regions than the cool interstellar side, with one "core ray" reserved for the solid angle occupied by the central star as seen from a particular grid point.

From every grid point $\boldsymbol{r_0}$=(x_0, y_0, z_0) along each ray in direction $\boldsymbol{n} = (n_x, n_y, n_z)$ ProDiMo solves the radiative transfer equation (Eq. 3.5) backwards along the photon propagation direction. The optical depth along the ray is given by

$$\tau(s) = \int_0^s \kappa_\nu^{\rm ext}(\boldsymbol{r_0} + s'\boldsymbol{n}) ds'. \tag{3.7}$$

The formal solution of the transfer equation Eq. 3.5 is

$$I_\nu = I_\nu^{\rm inc} e^{-\tau_\nu(s_{\rm max})} + \int_0^{s_{\rm max}} \kappa_\nu^{\rm ext}(s)\, S_\nu(s)\, e^{-\tau_\nu(s)}\, ds \tag{3.8}$$

and this is integrated numerically using a suitable step size Δs for a ray starting at $s=0$ with $\tau_\nu = 0$ and $I_\nu = 0$. For the core ray, the incident intensity from the end of the ray at $s_{\rm max}$ is given the value of the stellar intensity $I_\nu^{\rm inc} = I_\nu^\star$, whereas for all other rays

the interstellar intensity $I_\nu^{\rm inc} = I_\nu^{\rm ISM}$ is used. The stellar intensity is calculated using a model spectrum from a stellar atmosphere code (e.g. PHOENIX), with extra UV flux to allow for the accretion luminosity.

Having solved all rays from all points for all frequencies, the mean intensities J_ν at each point are updated. If the maximum relative change in J_ν is larger than some threshold value, the source functions are re-calculated and the radiative transfer is solved again.

The opacities used for the radiative transfer calculations are defined by the dust grain size distribution. The dust particle number density is given by

$$n_d = \int_{a_{\rm min}}^{a_{\rm max}} f(a)\, da\ , \tag{3.9}$$

where a is the particle radius and $f(a) \propto a^{-a_{\rm pow}}$ is the dust size distribution function [cm^{-4}]. The dust opacities are calculated as

$$\kappa_\lambda^{\rm ext} = \int_{a_{\rm min}}^{a_{\rm max}} \pi a^2\, Q_{\rm ext}(a,\lambda)\, f(a)\, da\ , \tag{3.10}$$

where $Q_{\rm ext}(a,\lambda)$ is the extinction efficiency. Similar formulae apply for the absorption and scattering opacities, $\kappa_\nu^{\rm abs}$ and $\kappa_\nu^{\rm sca}$.

The simple ray-based method used for the solution of the radiative transfer can lead to convergence issues at large optical depth in the disc midplane. Also the assumption of isotropic scattering, while reasonable at long wavelengths, is possibly insufficient in the optical and near-infrared, and a more sophisticated Monte Carlo method with angle-dependent scattering and better treatment at large optical depth would be preferable in these cases [Pinte et al., 2006, Harries, 2000, Harries et al., 2004, Min et al., 2009].

3.4 Chemistry

The chemistry model in PRODIMO considers 992 reactions involving 10 elements and $N_{\rm sp} = 76$ gas phase and solid ice species. It includes a detailed treatment of UV-photorates [see Kamp et al., 2010], H_2 formation on grain surfaces, vibrationally excited $H_2^\star$ chemistry, and ice formation (adsorption, thermal desorption, photo-desorption and cosmic-ray desorption) for a limited number of ice species.

The net formation rate of a chemical species i is calculated as

$$\frac{dn_i}{dt} = \sum_{jk\ell} R_{jk\to i\ell}(T_g)\, n_j n_k + \sum_{j\ell} (R^{ph}_{j\to i\ell} + R^{cr}_{j\to i\ell})\, n_j - n_i \left(\sum_{jk\ell} R_{i\ell\to jk}\, n_\ell + \sum_{jk} (R^{ph}_{i\to jk} + R^{cr}_{i\to jk}) \right) \tag{3.11}$$

where $R_{jk\to i\ell}$ designates (two-body) gas phase reactions between two reactants j and k, forming two products i and ℓ. $R^{ph}_{i\to jk}$ indicates a photo-reaction which depend on the local strength of the UV radiation field, and $R^{cr}_{j\to i\ell}$ a cosmic ray induced reaction.

Photon-induced reaction rates can generally be written as

$$R^{ph} = 4\pi \int \sigma(\nu) \frac{J_\nu}{h\nu}\, d\nu = \frac{1}{h} \int \sigma(\lambda)\, \lambda u_\lambda\, d\lambda \tag{3.12}$$

where the spectral photon energy density λu_λ is taken from the 2D continuum radiative transfer calculations and the cross-sections $\sigma(\lambda)$ from the Leiden database [van Dishoeck et al., 2008].

The chemical network is solved by assuming kinetic chemical equilibrium such that $\frac{dn_i}{dt} = 0$ in Eq. 3.11, giving $i = 1 \ldots N_{sp}$ non-linear equations for the unknown particle densities n_j ($j = 1 \ldots N_{sp}$). Imposing element conservation removes degeneracies between individual reactions, and the reaction system becomes well-defined. The non-linear equation system is solved using a Newton-Raphson method, and the resulting particle densities are stored and used as initial guesses for the next global iteration, in order to improve computational speed. In cases where the Newton-Raphson method fails, the model falls back to the time-dependent case and uses an ODE solver for 10^7 years. This is much slower but in practice gives the same results as the Newton-Raphson method.

3.5 Gas Thermal Balance

The net gain of thermal kinetic energy is written as

$$\frac{de}{dt} = \sum_k \Gamma_k(T_g, n_{sp}) - \sum_k \Lambda_k(T_g, n_{sp}) \tag{3.13}$$

where Γ_k and Λ_k are the various heating and cooling rates [erg cm^{-3} s^{-1}]. Assuming thermal energy balance, $de/dt = 0$ gives an implicit equation for T_g. Since the heating and cooling rates depend on the particle densities n_sp as well as on T_g, an iterative process is required whereby T_g is varied and the chemistry re-solved until T_g satisfies Eq. 3.13.

3.5.1 Non-LTE treatment of atoms, ions and molecules

The disc gas is able to exchange energy with the local radiation field through the absorption and emission of line photons by gas particles. In order to calculate the net gas heating or cooling rate due to such line transitions, it is necessary to determine the excitation level of the various gas particles (atoms, ions and molecules) throughout the disc. Considering for now an N-level system with bound-bound transitions only (bound-free transitions will be addressed in Section 3.6), we calculate the level populations n_j [cm^{-3}] by means of the statistical equations

$$n_i \sum_{j \neq i} R_{ij} = \sum_{j \neq i} n_j R_{ji} \quad , \tag{3.14}$$

which are solved together with the equation for the conservation of the total particle density of the considered species $\sum_i n_i = n_\mathrm{sp}$. The rate coefficients are given by [Mihalas, 1978]:

$$\begin{aligned} R_{ul} &= A_{ul} + B_{ul}\overline{J}_{ul} + C_{ul} \\ R_{lu} &= B_{lu}\overline{J}_{ul} + C_{lu} \quad , \end{aligned} \tag{3.15}$$

where u and l label an upper and lower level, respectively. A_{ul}, B_{ul}, B_{lu}, C_{ul} and C_{lu} are the Einstein coefficients for spontaneous emission, stimulated emission, absorption and the rate coefficients for collisional (de-)excitation, respectively. Additionally we have the Einstein relations $B_{ul}/A_{ul} = c^2/(2h\nu_{ul}^3)$, $B_{lu}/B_{ul} = g_u/g_l$ and the detailed balance relation $C_{lu}/C_{ul} = g_u/g_l \cdot \exp(-\Delta E_{ul}/kT_\mathrm{g})$, where ν_{ul}, g_u, g_l and ΔE_{ul} are the line centre frequency, the statistical weights of the upper and lower level and the energy difference, respectively. The line integrated mean intensity is given by

$$\overline{J}_{ul} = \frac{1}{4\pi} \iint \phi_{ul}(\nu, \boldsymbol{n})\, I_\nu(\boldsymbol{n})\, d\nu\, d\Omega \tag{3.16}$$

where $\phi_{ul}(\nu, \boldsymbol{n})$ is the line profile function in direction $\boldsymbol{n}$.

Escape-probability treatment

The spectral intensity I_ν in Eq. (3.16) is affected by line absorption and emission. Assuming that the line source function (Eq. 3.18) varies slowly in a local environment where the line optical depths (Eq. 3.19) build up rapidly, we can approximate for a static, plane-parallel medium

$$I_\nu(\mu) \approx I^{\rm cont}_{\nu_{ul}}(\mu) \exp\left(\frac{\phi_{ul}(\nu)\,\tau^{\rm ver}_{ul}}{\mu}\right) + S^{\rm L}_{ul}\left(1 - \exp\left(\frac{\phi_{ul}(\nu)\,\tau^{\rm ver}_{ul}}{\mu}\right)\right) \tag{3.17}$$

where $I^{\rm cont}_{\nu_{ul}}(\mu)$ is the continuous background intensity which propagates backward along the ray in direction μ. The direction μ=1 points "outward" ($\mu = \cos\theta$). The line source function and the perpendicular line optical depth are given by [Mihalas, 1978]

$$S^{\rm L}_{ul} = \frac{2h\nu^3_{ul}}{c^2}\left(\frac{g_u n_l}{g_l n_u} - 1\right)^{-1} \tag{3.18}$$

$$\tau^{\rm ver}_{ul} = \frac{A_{ul}\,c^3}{8\pi\nu^3_{ul}\Delta{\rm v}_D}\int_z^{z_{\rm max}}\left(n_l(z')\frac{g_u}{g_l} - n_u(z')\right)dz' \tag{3.19}$$

where $\Delta{\rm v}_D$ is the (turbulent + thermal) velocity Doppler width of the line, assumed to be constant along the line of sight in Eq. (3.19). Equations (3.16) and (3.17) can be combined to find

$$\overline{J}_{ul} = \frac{1}{2}\int_{-1}^{1} p^{\rm esc}_{ul}(\mu)\, I^{\rm cont}_{\nu_{ul}}(\mu) + (1 - p^{\rm esc}_{ul}(\mu))\, S^{\rm L}_{ul}\, d\mu \tag{3.20}$$

$$\approx P^{\rm pump}_{ul}\, J^{\rm cont}_{\nu_{ul}} + (1 - P^{\rm esc}_{ul})\, S^{\rm L}_{ul} \tag{3.21}$$

where the direction-dependent and the mean escape probabilities are found to be

$$p^{\rm esc}_{ul}(\mu) = \int_{-\infty}^{+\infty}\phi(x)\,\exp\left(-\frac{\tau^{\rm ver}_{ul}\,\phi(x)}{\mu}\right)dx \tag{3.22}$$

$$P^{\rm esc}_{ul} = \frac{1}{2}\int_{-1}^{1} p^{\rm esc}_{ul}(\mu)\, d\mu \tag{3.23}$$

with dimensionless line profile function $\phi(x) = \exp(-x^2)/\sqrt{\pi}$, $x = (\nu - \nu_{ul})/\Delta\nu_D$ and frequency width $\Delta\nu_D = \nu_{ul}\Delta{\rm v}_D/c$. Using Eq. (3.21), it is

straightforward to show that the unknown line source function S_{ul}^{L} can be eliminated, and the leading term $n_u A_{ul}$ cancels out, when considering the net rate $n_u A_{ul} + (n_u B_{ul} - n_l B_{lu})\,\overline{J}_{ul} = n_u A_{ul} P_{ul}^{\mathrm{esc}} + (n_u B_{ul} - n_l B_{lu}) P_{ul}^{\mathrm{pump}} J_{\nu_{ul}}^{\mathrm{cont}}$. Thus, we can solve the statistical rate Eqs. (3.14) with modified rate coefficients

$$\begin{aligned} \tilde{R}_{ul} &= A_{ul} P_{ul}^{\mathrm{esc}} + B_{ul} P_{ul}^{\mathrm{pump}} J_{\nu_{ul}}^{\mathrm{cont}} + C_{ul} \\ \tilde{R}_{lu} &= B_{lu} P_{ul}^{\mathrm{pump}} J_{\nu_{ul}}^{\mathrm{cont}} + C_{lu} \quad , \end{aligned} \tag{3.24}$$

which is known as escape-probability formalism [Avrett and Hummer, 1965, Mihalas, 1978]. P_{ul}^{esc} is the mean probability for line photons emitted from the current position to escape the local environment and P_{ul}^{pump} the mean probability for continuum photons to arrive at the current position. $J_{\nu_{ul}}^{\mathrm{cont}}$ is the continuous mean intensity at line centre frequency ν_{ul}, as would be present if no line transfer effects took place. In semi-infinite slab symmetry, all directions $\mu < 0$ have infinite line optical depth and can be discarded from the calculation of the escape probabilities

$$P_{ul}^{\mathrm{esc}}(\tau_{ul}^{\mathrm{ver}}) = \frac{1}{2} \int_{-\infty}^{+\infty} \phi(x) \int_0^1 \exp\Big(- \frac{\tau_{ul}^{\mathrm{ver}} \phi(x)}{\mu} \Big)\, d\mu\, dx \tag{3.25}$$

$$= \frac{1}{2} \int_{-\infty}^{+\infty} \phi(x)\, E_2(\tau_{ul}^{\mathrm{ver}} \phi(x))\, dx \tag{3.26}$$

This function is numerically fitted as

$$P_{ul}^{\mathrm{esc}}(\tau) = \begin{cases} 0.5 & , \tau = 0 \\ 0.5 + (0.1995 \ln \tau - 0.2484)\tau - 0.04594\tau^2 & , 0 < \tau \leq 0.6 \\ \dfrac{1 - \exp(-1.422\tau)}{3.324\tau + 0.2852\tau^2} & , 0.6 < \tau \leq 9 \\ \dfrac{0.1999}{\tau} \big(\ln(0.4799\tau) \big)^{-0.4195} & , 9 < \tau \end{cases} \tag{3.27}$$

Considering the pumping probability as defined by Eq. (3.21), it is noteworthy that $P_{ul}^{\mathrm{pump}} \approx P_{ul}^{\mathrm{esc}}$ is only valid in an almost isotropic background radiation field. In disc symmetry, much of the pumping is due to direct star light, which has a very pointed character. In the optically thick midplane, the continuous radiation field is almost isotropic, but here the pumping is pointless, because the radiation is thermalised and the collisional processes dominate. Considering near to far IR wavelengths at a certain height above the midplane, the irradiation from underneath plays a role, but these

directions are just the opposite of what is considered in Eq. (3.26), and so using $P_{ul}^{\mathrm{pump}} \approx P_{ul}^{\mathrm{esc}}$ would be strongly misleading. Thus, we approximate

$$P_{ul}^{\mathrm{pump}}(\tau_{ul}^{\mathrm{rad}}) \;=\; \int_{-\infty}^{+\infty} \phi(x)\, \exp\left(-\tau_{ul}^{\mathrm{rad}}\phi(x)\right)\, dx \tag{3.28}$$

with τ_{ul}^{rad} now being the radially inward line optical depth. This function is numerically fitted as

$$P_{ul}^{\mathrm{pump}}(\tau) = \begin{cases} 1 & ,\tau = 0 \\ 1 - 0.3989\tau + 0.09189\tau^2 - 0.01497\tau^3 & ,0 < \tau \leq 0.9 \\ \dfrac{1 - \exp(-0.6437\tau)}{0.6295\tau + 0.07008\tau^2} & ,0.9 < \tau \leq 9 \\ \dfrac{0.8204}{\tau}\left(\ln(0.3367\tau)\right)^{-0.4306} & ,9 < \tau \end{cases} \tag{3.29}$$

Background radiation field

The continuum background mean intensities $J_{\nu_{ul}}^{\mathrm{cont}}$ have an important impact on the gas energy balance. For example, in strong continuum radiation fields, the reverse process to line cooling, namely line absorption followed by collisional de-excitation, dominates. $J_{\nu_{ul}}^{\mathrm{cont}}$ is identified to be just given by the mean intensities calculated from the dust continuum radiative transfer (see Section 3.3). In order to obtain the required monochromatic mean continuum intensities at the line centre positions, we apply a cubic spline interpolation to the calculated local continuum $J_{\nu}^{\mathrm{cont}}(r,z)$ in frequency space.

Solving the statistical equations

Equations (3.14, 3.19, 3.24) form a system of coupled equations for the unknown population numbers n_i. Since the line optical depths (Eq. 3.19) depend partly on the local n_i, these equations must be solved iteratively. We apply a fully implicit integration scheme for the numerical solution of (Eq. 3.19) where the line optical depth increment along the last downward integration step, between the previous and the current grid point, is given by the local populations, i. e.

$$\Delta\tau_i^{\mathrm{ver}} = \frac{A_{ul}\, c^3}{8\pi\nu_{ul}^3 \Delta \mathrm{v}_D} \frac{n_l \frac{g_u}{g_l} - n_u}{n_{\langle \mathrm{H} \rangle}} \left(N_{\langle \mathrm{H} \rangle}(z_i) - N_{\langle \mathrm{H} \rangle}(z_{i+1})\right) . \tag{3.30}$$

where $N_{\langle \mathrm{H} \rangle}(z_i)$ is the vertical hydrogen column density at grid point z_i, and n_u, n_l and $n_{\langle \mathrm{H} \rangle}$ refer to the current grid point i. A simple Λ-type iteration scheme is found to converge within typically 0 to 20 iterations. The outward radial line optical depth increments $\Delta\tau_j^{\mathrm{rad}}$ between r_{j-1} and r_j are calculated in a similar fully implicit fashion.

Calculation of the heating/cooling rate

Once the statistical equations (Eqs. 3.14) have been solved, the radiative heating and cooling rates can be determined. There are two valid approaches. For the net cooling rate, one can either calculate the net creation rate of photon energy (radiative approach), or one can calculate the total destruction rate of thermal energy (collisional approach).

$$\Gamma_{\mathrm{rad}} = \sum_{u>l} n_l \Delta E_{ul} P_{ul}^{\mathrm{pump}} B_{lu} J_{\nu_{ul}}^{\mathrm{cont}} \tag{3.31}$$

$$\Lambda_{\mathrm{rad}} = \sum_{u>l} n_u \Delta E_{ul} \left(P_{ul}^{\mathrm{esc}} A_{ul} + P_{ul}^{\mathrm{pump}} B_{ul} J_{\nu_{ul}}^{\mathrm{cont}} \right) \tag{3.32}$$

$$\Gamma_{\mathrm{col}} = \sum_{u>l} n_u C_{ul} \Delta E_{ul} \tag{3.33}$$

$$\Lambda_{\mathrm{col}} = \sum_{u>l} n_l C_{lu} \Delta E_{ul} \tag{3.34}$$

Both approaches must yield the same net result $\Gamma_{\mathrm{rad}} - \Lambda_{\mathrm{rad}} = \Gamma_{\mathrm{coll}} - \Lambda_{\mathrm{coll}}$, which can be used to check the quality of the numerical solution. In practice, one pair of these heating/cooling rates is often huge in comparison to the other pair, e. g. $\{\Gamma_{\mathrm{rad}}, \Lambda_{\mathrm{rad}}\} \gg \{\Gamma_{\mathrm{col}}, \Lambda_{\mathrm{col}}\}$ in a thin gas with radiatively controlled populations, and $\{\Gamma_{\mathrm{rad}}, \Lambda_{\mathrm{rad}}\} \ll \{\Gamma_{\mathrm{col}}, \Lambda_{\mathrm{col}}\}$ in a dense gas with close to LTE populations. Thus, it is numerically favourable to choose

$$\Gamma = \begin{cases} \Gamma_{\mathrm{col}} & , \Gamma_{\mathrm{rad}} > \Gamma_{\mathrm{col}} \\ \Gamma_{\mathrm{rad}} & , \Gamma_{\mathrm{rad}} \leq \Gamma_{\mathrm{col}} \end{cases} \tag{3.35}$$

$$\Lambda = \begin{cases} \Lambda_{\mathrm{col}} & , \Gamma_{\mathrm{rad}} > \Gamma_{\mathrm{col}} \\ \Lambda_{\mathrm{rad}} & , \Gamma_{\mathrm{rad}} \leq \Gamma_{\mathrm{col}} \end{cases} \tag{3.36}$$

There are a number of further specific heating and cooling processes not covered by the escape probability treatment of line transfer. Photoelectric heating, cosmic ray ionisation, carbon photo-ionisation and H_2 photo-dissociation are still radiative

heating processes, while other heating mechanisms are of chemical nature, such as H_2 formation heating, or of dynamical nature, such as viscous heating. One heating mechanism of note is PAH heating. Very small dust grains such as polycyclic aromatic hydrocarbons (PAHs) are an extremely efficient heating source for the gas, ejecting super-thermal electrons via the photoelectric effect which then thermalise through collisions with the gas. The heating and cooling balance also takes into account the process of thermal accommodation, which refers to the exchange of energy between gas and dust particles through inelastic collisions.

After the chemistry (see Section 3.4) and the thermal gas energy balance (see Section 3.5) have been solved throughout the disc volume, all particle densities n_i and the kinetic temperature of the gas T_g are known, and ProDiMo can update the isothermal sound speeds on the numerical grid $c_T^2(r_j, z_k)$ as preparation for the next iteration of the hydrostatic disc structure (see Section 3.2).

$$\rho = n_e m_e + \sum_i n_i m_i \tag{3.37}$$

$$p = \left(n_e + \sum_i n_i\right) kT_g \tag{3.38}$$

$$c_T^2 = p/\rho \tag{3.39}$$

3.6 Atomic Hydrogen bound-free transitions

At present ProDiMo includes the non-LTE treatment of bound-bound line transitions for 47 chemical species. I have modified the code to include atomic hydrogen as an N-level system plus continuum. These modifications have yet to be implemented for the modelling described in Chapters 4–6, but I examine the effects of introducing these bound-free hydrogen transitions in Chapter 7. Previously the only contribution from HI to the gas heating/cooling was through a simple parameterisation of the Lyman-α cooling rate.

The atomic data [Cunto et al., 1993] include 140 bound-bound radiative transitions between 36 atomic levels, up to and including principal quantum number $n = 8$. The bound-bound electron collision rates are taken from Vernazza et al. [1981]. In addition to these bound-bound transitions, I have implemented the bound-free processes of photoionisation, radiative recombination, collisional ionisation and three body (dielectric) recombination.

3.6.1 Rate coefficients

In addition to the rate coefficients for bound-bound coefficients (Eq. 3.24), it is necessary to consider the ionisation and recombination rates for the various excitation states, i. These are formulated according to Mihalas [1978]:

$$R_{i\mathrm{II}} = 4\pi \int_{\nu^i_{\mathrm{thr}}}^{\infty} \frac{J_\nu}{h\nu} \sigma_i(\nu)\, d\nu + n_e \beta_i(T_\mathrm{g}) \tag{3.40}$$

$$R_{\mathrm{II}i} = \frac{n_e}{S_i(T_\mathrm{g})} \left[4\pi \int_{\nu^i_{\mathrm{thr}}}^{\infty} \left(\frac{2\nu^2}{c^2} + \frac{J_\nu}{h\nu} \right) \exp\left(-\tfrac{h\nu}{kT_\mathrm{g}} \right) \sigma_i(\nu) d\nu + n_e \beta_i(T_\mathrm{g}) \right] \tag{3.41}$$

$$S_i(T_\mathrm{g}) = \frac{n_{\mathrm{II}} n_e}{n_i} = \frac{2Z_{\mathrm{II}}}{g_i} \frac{(2\pi m_e kT_\mathrm{g})^{3/2}}{h^3} \exp\left(-\frac{\chi_i}{kT_\mathrm{g}} \right) \tag{3.42}$$

$$\tag{3.43}$$

where J_ν is the angle-averaged intensity and $\sigma_i(\nu)$ the ionisation cross-section at frequency ν (taken from Cunto et al. [1993]). β_i is the rate coefficient for collisional ionisation. At present only collisions with electrons are considered, and the collisional ionisation rates are taken from Vernazza et al. [1981]. χ_i is the energy difference between excitation level i and the continuum, and $\nu^i_{\mathrm{thr}} = \chi_i / h$ the corresponding threshold frequency. S_i is the Saha function, g_i the statistical weight of level i, and Z_{II} the partition function for the ionised states, taken equal to unity in this case.

3.6.2 Hydrogen shielding

The background radiation field for the non-LTE calculation comes from the solution to the dust continuum radiative transfer. In the absence of a full gas+dust continuum calculation in ProDiMo, I have implemented the following treatment to attempt to take into account continuum absorption by neutral hydrogen. The intensities J_ν in Eqns. 3.40 & 3.41 are attenuated by $e^{-\tau_\nu}$, with an optical depth

$$\tau_\nu = \sum_{i=1}^{N_{\mathrm{lev}}} (N_{\mathrm{HI}} + \Delta x\, n_{\mathrm{HI}})\, p_i^{\mathrm{bf}}\, \frac{n_{\mathrm{HI}} + n_{\mathrm{HII}}}{n_{\mathrm{HI}}}\, \sigma_i^{\mathrm{bf}}(\nu) \tag{3.44}$$

where N_{HI} is the neutral hydrogen column density (taken from the chemistry solution), n_{HI} and n_{HII} are the local neutral and ionised hydrogen number density respectively, and p_i^{bf} is the local population of level i relative to $n_{\mathrm{tot}} = n_{\mathrm{HI}} + n_{\mathrm{HII}}$. This is repeated in

the radial and vertical directions, and the total shielding factor is a scaled combination of the two. The scaling is determined by the relative dust attenuation of the UV field strength in the radial and vertical directions. Equation 3.44 makes the assumption that the local neutral hydrogen level populations are replicated along the line of sight.

3.6.3 External chemical rates

The bound hydrogen level populations and ionisation fraction are calculated simultaneously, relative to $n_{\rm tot} = n_{\rm HI} + n_{\rm HII}$, where $n_{\rm HI}$ and $n_{\rm HII}$ are the abundances calculated in the solution of the chemical network. The non-LTE treatment described in this section will in general yield a different hydrogen ionisation fraction to the chemistry solution, unless some way is found to take into account the various external chemical rates involving H and H^+, in addition to the bound-bound and bound-free transition rates.

The only bound-free reaction included in the ProDiMo chemical network is the direct recombination of hydrogen, taken from the Umist database [Le Teuff et al., 2000]:

$$H^+ + e^- \rightarrow H + h\nu \tag{3.45}$$

The condition of kinetic chemical equilibrium requires that

$$\frac{dn_{\rm H_II}}{dt} = \sum_i R_i - R_{\rm rec} = 0, \tag{3.46}$$

where $R_{\rm rec}$ is the Umist recombination rate and the R_i are all other chemical rates affecting the H^+ abundance. It follows that $\sum_i R_i = R_{\rm rec}$, and so the various chemical rates can be accounted for in the non-LTE solution by de-populating the bound states of hydrogen at a rate equal to $R_{\rm rec}$, and populating the ionised state accordingly.

3.6.4 Heating and cooling rates

In addition to the radiative and collisional bound-bound heating/cooling rates described in Section 3.5.1, the atomic hydrogen treatment takes into account cooling by radiative recombination and collisional ionisation, and heating by photoionisation and dielectric recombination. The problem is slightly more complicated than the purely bound-bound case, since the radiative processes affect both the thermal and photon energy, with an energy deficit/surplus equal to the binding energy of the corresponding atomic level.

The rate of destruction of photon energy due to photoionisation, and the corresponding rate of creation of thermal energy, are given by:

$$Q_{\rm heat}^{\rm phot,rad} = 4\pi \sum_{i=1}^{N_{\rm lev}} \int_{\nu_{\rm thr}^i}^{\infty} J_\nu \, \sigma_i(\nu) \, d\nu \tag{3.47}$$

$$Q_{\rm heat}^{\rm therm,rad} = 4\pi \sum_{i=1}^{N_{\rm lev}} \int_{\nu_{\rm thr}^i}^{\infty} J_\nu \, \sigma_i(\nu) \, \frac{(\nu - \nu_{\rm thr}^i)}{\nu} \, d\nu \tag{3.48}$$

The rate of creation of photon energy and rate of destruction of thermal energy due to radiative recombination are given by:

$$Q_{\rm cool}^{\rm phot,rad} = 4\pi \sum_{i=1}^{N_{\rm lev}} \frac{n_e}{S_i(T_{\rm g})} \int_{\nu_{\rm thr}^i}^{\infty} \left(\frac{2h\nu^3}{c^2} + J_\nu \right) \exp\left(-\tfrac{h\nu}{kT_{\rm g}} \right) \sigma_i(\nu) d\nu \tag{3.49}$$

$$Q_{\rm cool}^{\rm therm,rad} = 4\pi \sum_{i=1}^{N_{\rm lev}} \frac{n_e}{S_i(T_{\rm g})} \int_{\nu_{\rm thr}^i}^{\infty} \left(\frac{2h\nu^3}{c^2} + J_\nu \right) \exp\left(-\tfrac{h\nu}{kT_{\rm g}} \right) \sigma_i(\nu) \, \frac{(\nu - \nu_{\rm thr}^i)}{\nu} \, d\nu \tag{3.50}$$

We also need to take into account the cooling and heating rates due to collisional ionisation and dielectric recombination respectively, given by:

$$Q_{\rm cool}^{\rm therm,col} = \sum_{i=1}^{N_{\rm lev}} n_e \beta_i(T_{\rm g}) \chi_i \tag{3.51}$$

$$Q_{\rm heat}^{\rm therm,col} = \sum_{i=1}^{N_{\rm lev}} \frac{n_e^2}{S_i(T_{\rm g})} \beta_i(T_{\rm g}) \chi_i \tag{3.52}$$

The total heating and cooling rates are then given by

$$\Gamma_{\rm rad}^{\rm bf} = \Gamma_{\rm rad} + Q_{\rm heat}^{\rm phot,rad} + Q_{\rm heat}^{\rm chem} \tag{3.53}$$

$$\Lambda_{\rm rad}^{\rm bf} = \Lambda_{\rm rad} + Q_{\rm cool}^{\rm phot,rad} \tag{3.54}$$

$$\Gamma_{\rm therm}^{\rm bf} = \Gamma_{\rm col} + Q_{\rm heat}^{\rm col} + Q_{\rm heat}^{\rm therm,rad} \tag{3.55}$$

$$\Lambda_{\rm therm}^{\rm bf} = \Lambda_{\rm col} + Q_{\rm cool}^{\rm col} + Q_{\rm cool}^{\rm therm,rad} \tag{3.56}$$

$$\tag{3.57}$$

where $\Gamma_{\rm rad}$, $\Lambda_{\rm rad}$, $\Gamma_{\rm col}$ and $\Lambda_{\rm col}$ are the bound-bound radiative and collisional heating and cooling rates as defined in Eqns. 3.31–3.34, and $Q_{\rm heat}^{\rm chem}$ is the chemical heating rate from pumping the ionised state at a rate equal to the UMIST recombination rate, as described

in Section 3.6.3.

As in the purely bound-bound case (see Section 3.5.1), the smaller pair of heating/cooling rates is selected, either $\{\Gamma_{\rm rad}, \Lambda_{\rm rad}\}$ or $\{\Gamma_{\rm col}, \Lambda_{\rm col}\}$. The level populations are then solved iteratively, including the $(N_{\rm lev}+1)$ ionised state, until there is no change in the net heating/cooling rate between iterations.

Chapter 4

Line Diagnostics in Herbig Ae Discs

4.1 Introduction

The work described in this chapter aims to assess the diagnostic power of various gas emission lines, and in particular their ability to trace the disc gas mass. This material is taken from work published in the *Astronomy & Astrophysics* paper "Radiation thermochemical models of protoplanetary disks, II. Line diagnostics" by Kamp, Tilling, Woitke, Thi, and Hogerheijde [2010]. My contribution to this work was to run all of the described models (Sections 4.2 & 4.3), and to carry out the ray-tracing and subsequent analysis for the CO lines (Sections 4.4.2 & 4.5.2). The ray-tracing and analysis of the far-infrared OI and CII fine structure lines (Sections 4.4.1 & 4.5.1), and the comparison with observations (Section 4.5.3), were carried out by Inga Kamp, and so I give less emphasis to these results, although all the key points from Kamp et al. [2010] are included for purposes of context.

Observations of gas in protoplanetary discs are intrinsically difficult to interpret as they reflect the interplay between a complex chemical and thermal disc structure, statistical equilibrium and optical depth effects. This is particularly true if non-thermal excitation such as fluorescence or photodissociation dominate the statistical equilibrium.

The first studies of gas in protoplanetary discs concentrated on the rotational transitions of abundant molecules such as CO, HCN and HCO^+ [e.g. Beckwith et al., 1986, Koerner et al., 1993, Dutrey et al., 1997, van Zadelhoff et al., 2001, Thi et al., 2004]. Those lines originate in the outer regions of discs, $r > 100$ AU, where densities are at most $n \sim 10^7$ cm^{-3}. The interpretation of those lines was mainly based on tools

and expertise developed for molecular clouds. Using the CO J=3-2 line, Dent et al. [2005] inferred for a sample of Herbig Ae and Vega-type stars a trend of disc outer radius with age; on average, the outer disc radius in the 7-20 Myr range is three times smaller than that in the < 7 Myr range. Also, the disc radii inferred from the dust spectral energy distribution (SED) are generally smaller than those derived from the gas line [Isella et al., 2007, Piétu et al., 2005]. Hughes et al. [2008a] suggest a soft outer edge as a solution to the discrepancy. Comparison of CO J=3-2 maps of four discs to different types of disc models strongly supports a soft edge in favor of a sharp cutoff. Piétu et al. [2007] use the CO and HCO^+ lines to probe the radial and vertical temperature profile of the disc. Simple power law disc models and LTE radiative transfer provides best matching results for radial temperature gradients around $r^{-0.5}$. The ^{12}CO J=2-1 line, ^{13}CO J=2-1 and ^{13}CO J=1-0 lines used in their analysis probe subsequently deeper layers and reveal a vertical temperature gradient ranging from 50 K in the higher layers to below the freeze-out temperature of CO in the midplane. This confirms earlier findings by Dartois et al. [2003].

However, disc masses derived from the CO lines are in general lower than disc masses derived from dust observations [e.g. Zuckerman et al., 1995, Thi et al., 2001]. Possible explanations include CO ice formation in the cold midplane and photodissociation in the upper tenuous disc layers. Any single gas tracer alone can only provide gas masses of the species and volume from which it originates, the same way as dust masses derived from a single photometric measurement are only sensitive to grains of a particular size range, namely those grain sizes that dominate the emission at that photometric wavelength. Hence individual gas tracers are more valuable for probing the physical conditions of the volume where they arise than the total disc mass. A combination of suitable gas tracers can then allow us to characterize the gas properties in protoplanetary discs and study it during the planet formation process.

This work aims to explore the diagnostic power of the fine structure lines of [O I] and [C II], in addition to the low rotational transitions of CO. It was carried out prior to obtaining Herschel observations of the far-IR lines in Herbig Ae discs, but these data are fully utilised in later chapters. Earlier modelling of these lines indicated that they should be detectable down to disc masses of 10^{-5} $M_\odot$ of gas, so also in the very gas-poor debris discs [Kamp et al., 2005]. More recent work by Meijerink et al. [2008] presents fine structure lines from the inner 40 AU disc of an X-ray irradiated T Tauri disc; the models indicate that the [O I] emission originates over a wide range of radii

and depth and is sensitive to the X-ray luminosity. However, most of the C II and O I line emission comes from larger radii where the gas temperature is dominated by UV heating processes. Jonkheid et al. [2007] find from thermo-chemical models of UV dominated Herbig Ae discs that the [O I] lines are generally a factor 10 stronger that the [C II] line. An initial exploration of the origin of the fine structure lines was carried out in Woitke et al. [2009a] and it was found that The [C II] 157.7 μm line probes the upper flared surface layers of the outer disc while the [O I] 63.2 μm line originates from the thermally decoupled surface layers inward of about 100 AU, above $A_V \approx 0.1$. The latter line is very sensitive to the gas temperature and can be used to distinguish between hot ($T_{\rm gas} \approx 1000$ K) and cold ($T_{\rm gas} = T_{\rm dust}$) disc atmospheres. Since the fine structure lines generally originate from a wider radial and vertical range than for example the CO rotational lines, they are potentially more suitable gas mass tracers.

This chapter uses ProDiMo to study the gas line emission from discs around Herbig Ae stars. The disc parameters were chosen to resemble the disc around MWC480. According to previous work by Mannings et al. [1997], Thi et al. [2001] and Piétu et al. [2007], the disc around this star extends from ≈ 0.5 AU to 700 AU. We choose here a surface density profile $\Sigma \sim r^{-1.0}$. The central star is an A2e Herbig Ae star with a mass of 2.2 $M_\odot$ and an effective temperature of 8500 K.

4.2 Methods

I compute a series of Herbig Ae disc models with masses between 2.2×10^{-2} and 10^{-6} $M_\odot$. The parameters are summarized in Table 4.1. The dust used in this model is typically larger than ISM dust and generates the $\sim \lambda^{-1}$ opacity law as derived from dust observations [e.g. Beckwith and Sargent, 1991, Mannings and Emerson, 1994, Rodmann et al., 2006].

A Phoenix stellar model Brott and Hauschildt [2005] with an effective temperature of 8500 K is used to represent the stellar irradiation, and a highly diluted 20000 K black body for the interstellar radiation field, that penetrates the disc from all sides. The dust opacities are computed using Mie theory and optical constants from Draine and Lee [1984]. The chemical network contains 71 species (built from 9 elements) connected through 950 reactions (photo reactions, CR ionization, neutral-neutral, ion-molecule, as well as grain adsorption and desorption processes for CO, CO_2, H_2O, CH_4 and NH_3 ice).

There are a number of features not yet present in ProDiMo which are utilised in later chapters. The atomic hydrogen heating and cooling processes outlined in Section 3.6 aren't yet implemented. Also ProDiMo is not yet able to perform the ray tracing calculations to determine the line emission, and the seperate Monte Carlo radiative transfer code Ratran is used in this instance. All of the models described in this chapter have dust grains which are homogeneously mixed with the gas, i.e. no dust settling is implemented. The code does not yet include X-ray heating, although this seems a minor issue for Herbig stars that generally have quite moderate X-ray luminosities, $L_X \ll 10^{30}$ erg s^{-1}.

The disc models described here are fully converged models, for which the hydrostatic pressure balance has been solved iteratively with the radiative transfer, chemistry and heating/cooling balance. This is in contrast to later models, for which prescribed disc structures are adopted for reasons of efficiency.

4.2.1 Line radiative transfer

The line emission from the disc models is computed using the two-dimensional Monte Carlo radiative transfer code Ratran developed by Hogerheijde and van der Tak [2000]. The code uses a two-step approach to solve the non-LTE line radiative transfer, Amc, and Sky. The first code solves the level population numbers for a given model atom/molecule within an arbitrary two-dimensional density and temperature distribution. The second one performs the ray tracing to derive the emission for a given line, distance and disc inclination.

Ratran requires a grid of rectangular cells in cylindrical coordinates $r \in \{r_i, r_{i+1}\}$ and $z \in \{z_j, z_{j+1}\}$ which is different from the grid of points used in ProDiMo. It is therefore necessary to create a suitable grid of cells for Ratran and "fill" the cells in a physically sensible way, which will involve some kind of averaging for the physical quantities. The details of this re-gridding process can be found in Kamp et al. [2010]. In addition, the Ratran code was modified to obtain the following line transfer results, in order to improve its performance in the context of the complex chemical environments found in discs. These modifications are also detailed in Kamp et al. [2010].

Table 4.1: Parameters of the Herbig Ae model series.

Quantity	Symbol	Value
stellar mass	$M_\star$	$2.2\,\mathrm{M}_\odot$
effective temperature	T_{eff}	8500 K
stellar luminosity	$L_\star$	$32\,L_\odot$
disc mass	M_{disc}	2.2×10^{-2}, 10^{-2}, 10^{-3}, 10^{-4}, 10^{-5}, $10^{-6}\,\mathrm{M}_\odot$
inner disc radius	R_{in}	0.5 AU (1)
outer disc radius	R_{out}	700 AU
radial column density power index	ϵ	1.0
dust-to-gas mass ratio	ρ_d/ρ	0.01
minimum dust particle radius	a_{min}	$0.05\,\mu$m
maximum dust particle radius	a_{max}	$200\,\mu$m
dust size distribution power index	a_{pow}	3.5
dust material mass density	ρ_{gr}	$2.5\,\mathrm{g\,cm^{-3}}$ (2)
strength of incident ISM UV	χ^{ISM}	1 (3)
cosmic ray ionization rate of H_2	ζ_{CR}	$5\times10^{-17}\ \mathrm{s^{-1}}$
abundance of PAHs relative to ISM	f_{PAH}	0.1
α viscosity parameter	α	0.0

(1): soft inner edge applied, see Sect. 3.1 of Woitke et al. [2009a]

(2): the dust optical properties are taken from Draine and Lee [1984]

(3): here $\chi^{\mathrm{ISM}} = 1$ corresponds to a "unit Draine field", as adopted by Röllig et al. [2007], Woitke et al. [2009a] etc.

Ray tracing

We assume for our generic disc a distance of 131 pc and and inclination of 45 degrees. The pixel size (spatial resolution) is 0.05“ and the entire box has a size of 13×13” to ensure that no emission is lost (disc diameter is 10”). The velocity resolution is set to 0.05 km/s and the total range is from -25 to 25 km/s for the C II line and -40 to 40 km/s for the O I lines. The different velocity ranges reflect the differences in radial origin of the lines. For the oxygen fine structure lines, oversampling of the central pixels (out to 1.6”) was used, i.e. an additional 2 rays generated per pixel.

The CO lines were computed within the same box of 13×13”, but with a spatial resolution of 0.12” and a spectral resolution of 0.2 km/s. No oversampling was used in this case.

Atomic and molecular data

Energy levels, statistical weights, Einstein A coefficients and collision cross sections are taken from the Leiden LAMBDA database [Schöier et al., 2005a]. Table 4.2 provides an overview of the C II, O I and CO data used in this work.

Table 4.2: Atomic and molecular data taken from the LAMBDA database [Schöier et al., 2005a].

Species	# Lev.	# Lines	Collision partner	Reference
C^+	2	1	H	Launay and Roueff [1977]
			e^-	Wilson and Bell [2002]
			o-H_2	Flower and Launay [1977]
			p-H_2	Flower and Launay [1977]
O	3	3	H	Launay and Roueff [1977]
			e^-	Bell et al. [1998]
			o-H_2	Jaquet et al. [1992]
			p-H_2	Jaquet et al. [1992]
			H^+	Chambaud (1980)(1)
CO	26	25	H	Chu and Dalgarno [1975]
			H_2	Schinke et al. [1985]

(1): private communication

Table 4.3: Atomic and molecular data for the oxygen and carbon fine structure lines and the CO rotational lines.

Line identification			E_u	E_l	A_{ul}	$n_{\rm crit}$
	[μm]		[K]	[K]	[s^{-1}]	[cm^{-3}]
O I	63.2	$^3P_1 - {}^3P_2$	227.7	0.0	8.865(-5)	5(5)
O I	44.1	$^3P_0 - {}^3P_2$	326.6	0.0	1.275(-10)	0.5
O I	145.5	$^3P_0 - {}^3P_1$	326.6	227.7	1.772(-5)	6(4)
C II	157.7	$^2P_{\frac{3}{2}} - {}^2P_{\frac{1}{2}}$	91.2	0.0	2.300(-6)	3(3)
Line identification			E_u	E_l	A_{ul}	$n_{\rm crit}$
	[GHz]		[K]	[K]	[s^{-1}]	[cm^{-3}]
CO	115. 3	J = 1 – 0	5.53	0.0	7.203(-8)	(1) 5.0(3) $T_{\rm g}^{-0.66}$
CO	230.5	J = 2 – 1	16.60	5.53	6.910(-7)	(1) 1.9(4) $T_{\rm g}^{-0.45}$
CO	345.8	J = 3 – 2	33.19	16.60	2.497(-6)	(1) 4.6(4) $T_{\rm g}^{-0.35}$

(1): CO critical densities from Kamp and van Zadelhoff [2001]
The notation 5(5) stands for 5×10^5.
Oxygen levels 2, 1, 0 correspond to $^3P_2$, $^3P_1$, and $^3P_0$, respectively.

Dust opacities

The dust opacities used in the radiative transfer code are consistent with the opacities used in the computation of the disc model with ProDiMo. The choice of opacities impacts the continuum around the line, i.e. the dust thermal emission. For oxygen, the low fine structure levels can be pumped by the thermal dust background. We see differences of up to 50 % in the continuum fluxes around the O I fine structure lines and up to 20 % differences in the line emission itself when we choose either the grain size distribution from Table 4.1 using optical constants from Draine and Lee [1984] or opacity tables from Ossenkopf and Henning [1994]. The latter are based on an MRN size distribution for interstellar medium grains $f(a) \sim a^{-3.5}$ with sizes 5 nm $< a <$ 0.25 μm. In this paper, the possibility of icy grain mantles or non-spherical shapes is not explored.

4.3 The disc models

I compute a series of six disc models with different disc masses (2.2×10^{-2}, 10^{-2}, 10^{-3}, 10^{-4}, 10^{-5} and 10^{-6} $M_\odot$) and all other parameters remaining fixed. It is important to stress that this series of models is not intended to reflect an evolutionary sequence as

the dust properties are not changed accordingly (e.g. dust grain sizes, dust-to-gas mass ratio, settling). The goal is to explore a range of physical conditions, study their impact on the disc chemistry and analyze how this impacts the cooling radiation that will be probed e.g. with the Herschel satellite.

4.3.1 Physical structure

Fig. 4.1 provides an overview of the computed physical quantities such as gas density, UV radiation field strength, optical extinction, gas temperature and dust temperature resulting from our series of Herbig disc models; each row presents a model with different mass and shows three quantities, total hydrogen number density, UV radiation field strength, and gas temperature. The white dashed lines in the second column of this figure indicate the $A_V = 1$ and $A_V = 10$ surfaces. The 2.2×10^{-2} $M_\odot$ model is optically thick in the vertical direction out to $\sim$ 400 AU. Reducing the disc mass by a factor 200 leaves only a dense $\sim$ 10 AU wide optically thick ring and the low mass disc models ($\leq 10^{-4}$ $M_\odot$) have very low vertical extinction, $A_V \lesssim 0.1$, throughout the entire disc.

The high mass models show two vertically puffed up regions, one around 0.5 AU (the classical "inner rim"), the other one more radially extended between 5 and 10 AU. The very low mass models (10^{-5} $M_\odot$ and below) do not show the typical flaring disc structure as observed in optically thick disc models, but they are still very extended in the vertical direction. The extreme gas temperatures in these low mass models are a result of direct heating by the photoelectric effect on small dust grains (PAHs) and pumping of Fe II by the stellar radiation field. In these optically thin discs, coupling between gas and dust grains is not efficient.

4.3.2 Chemical structure

The particle densities of ionized carbon, oxygen and the abundance of CO are shown in Fig. 4.2. The oxygen abundance is rather constant throughout the discs (C/O ratio $\sim$ 0.45), being only lower by a factor of two where the CO and OH abundances are high; OH forms at high abundance inside 30 AU above an A_V of a few, thus co-spatial with the warm (> 200 K) CO gas. Extremely low abundances occur only if significant amounts of water form close to the midplane inside 1-10 AU ($2.2 \times 10^{-2} - 10^{-3}$ $M_\odot$ models).

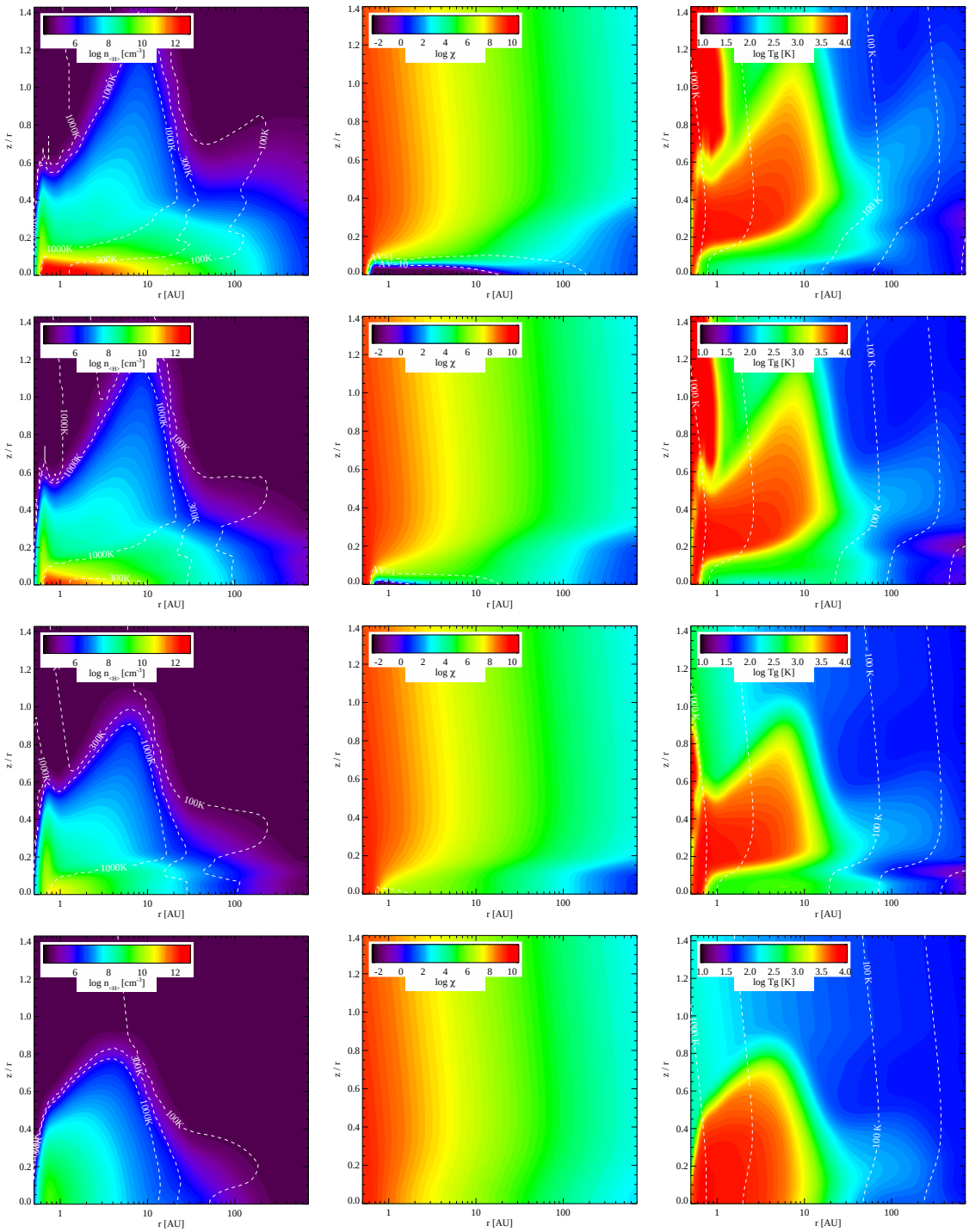

Figure 4.1: From top to bottom row: disc models with 10^{-2}, 10^{-3}, 10^{-4} and 10^{-5} $M_\odot$. The first column shows the total hydrogen number density $\log n_{\langle \mathrm{H} \rangle}$ with white contours indicating gas temperatures of 100, 300, and 1000 K. The second column shows the UV radiation field strength χ (91.2 – 205.0 nm) from full 2D radiative transfer. The third column shows the gas temperature $\log T_\mathrm{g}$ with white contours indicating dust temperatures of 20, 40, 100, 300 and 1000 K.

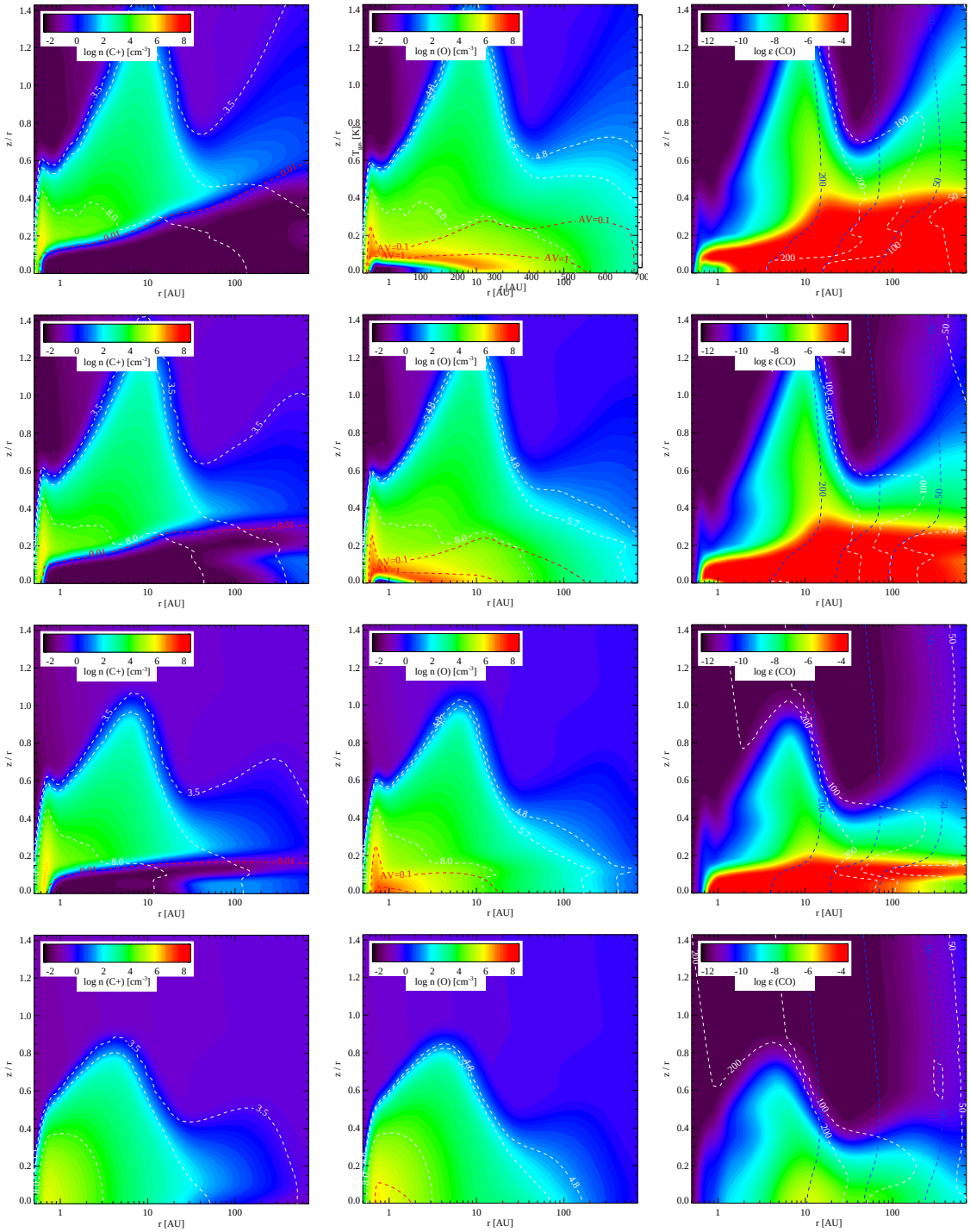

Figure 4.2: From top to bottom row: disc models with 10^{-2}, 10^{-3}, 10^{-4} and 10^{-5} $M_\odot$. The first column shows the C^+ density with white contours indicating the critical density for the [C II] line and densities of 10^6 and 10^8 cm^{-3} and a red contour line where the PDR parameter $\chi/n_{\langle H\rangle} = 0.01$. The second column shows the O density with white contours indicating the critical densities for the two oxygen lines, $n_{\langle H\rangle} = 6 \times 10^4$ and 5×10^5 cm^{-3}, and a density of 10^8 cm^{-3}. Extinctions of $A_V = 0.1$ and 1 are denoted by the red contour lines. The third column shows the CO abundance with white contours indicating gas temperatures of 50, 100, and 200 K and the blue contours indicating dust temperatures of 50, 100, and 200 K).

Carbon is fully ionized in the disc models with masses below 10^{-4} $M_\odot$. The C^+ abundance is complementary to the CO abundance as the neutral carbon layer between them is very thin. The C^+/C/CO transition is governed by photon dominated region (PDR) physics and can be well defined using the classical PDR parameter $\chi/n_{\langle H\rangle}$. Above $\chi/n_{\langle H\rangle} = 0.01$ (see Fig. 4.2), carbon is fully ionized and its density structure resembles that of the total gas density (two puffed up inner rims). The column density of the ionized carbon layer is always smaller than a few times 10^{17} cm^{-3}. The mass of C^+ in the irradiated layers of the disc is roughly constant until the optically thin disc limit is reached in which case it is given by $M_{\rm gas}\epsilon(\text{carbon})\,(m_C/\mu m_H)$ (see Table 4.4).

High abundances of CO can be found down to disc masses of 10^{-4} $M_\odot$. Below that, the entire disc becomes optically thin (radially and vertically), thus reducing the CO abundances even in the midplane to values below 10^{-6}. In the models with masses above 10^{-3} $M_\odot$, densities in the innermost region are high enough to form a large water reservoir [Woitke et al., 2009b]. At densities in excess of $\sim 10^{11}$ cm^{-3}, the water formation consumes all oxygen, thus limiting the amount of CO that can form in the gas phase. In the upper disc layers, the CO abundance is very low due to the combined impact of UV irradiation from the inside (central star) and outside (diffuse interstellar radiation field). Fig. 4.2 also shows that the temperature of CO in the outer disc decouples from the dust temperature (white contours: gas, blue contours: dust), even though differences are generally within a factor two ($T_{\rm gas} > T_{\rm dust}$). This is relevant for the CO low rotational lines that are predominantly formed in those regions (see Sect. 4.4.2).

4.3.3 Self-similarity

The six disc models show a large degree of self-similarity in their temperature and chemical structure. Lowering the disc mass removes mainly the thick midplane and the innermost dense regions. In that sense, this series of decreasing mass zooms in into disc layers further away from the star and at larger heights. The reason for this self-similarity lies partly in the two-direction escape probability used to compute the gas temperature and partly in the chemistry being independent of neighboring grid points (no diffusion or mixing). The solution in the disc is mostly described by the local $\chi/n_{\langle H\rangle}$.

Table 4.4: Characteristics of selected species in the Herbig disc models. $\langle T_g \rangle$ and $\langle T_d \rangle$ are the mass averaged gas and dust temperature(1).

M_{disc} [$M_\odot$]	Species	Mass [$M_\odot$]	$\langle T_g \rangle$ [K]	$\langle T_d \rangle$ [K
$2.2\,10^{-2}$	O	4.2(-5)	61	34
	C^+	1.3(-7)	96	46
	CO	6.0(-5)	62	35
10^{-2}	O	2.1(-5)	61	35
	C^+	1.1(-7)	99	46
	CO	2.7(-5)	61	35
10^{-3}	O	2.5(-6)	64	34
	C^+	9.7(-8)	79	34
	CO	1.8(-6)	79	42
10^{-4}	O	3.2(-7)	77	39
	C^+	4.9(-8)	75	37
	CO	9.2(-8)	103	51
10^{-5}	O	7.0(-8)	92	50
	C^+	2.0(-8)	91	48
	CO	3.6(-12)	576	126
10^{-6}	O	5.1(-8)	53	43
	C^+	1.7(-8)	53	43
	CO	6.1(-15)	89	54

(1): $\langle T \rangle = \frac{\int_V T(r,z) n_{sp}(r,z) dV}{\int_V n_{sp}(r,z) dV}$, species density n_{sp} and volume element dV.

4.3.4 Strength of UV field

To assess the impact of the UV field on the disc structure and line ratios, I compute two additional disc models with 10^{-2} $M_\odot$ disc masses, using effective temperatures of 9500 and 10500 K. This range reflects the typical temperatures encountered for Herbig Ae stars. To isolate the effect of UV irradiation, the luminosity is kept constant, so that a change in effective temperature changes only the fraction of UV versus optical irradiation.

Increasing the stellar effective temperature to 10500 K leads to a vertically more extended disc structure, thus pushing the H/H_2 transition slightly outwards. Though the dust temperatures are unaffected (they depend rather on total luminosity), the mass averaged gas temperatures increase by up to a factor two for certain species such as CO and O. The change for C^+ being in the uppermost tenuous surface is more dramatic; its mass averaged temperatures increase from $\sim$ 100 K (T_{eff} = 8460 K, Table 4.4) to

330 K ($T_{\rm eff}$ = 10500 K).

4.3.5 Dust opacities

In a similar way, I have varied the dust opacity in the 10^{-2} $M_\odot$ disc mass model, using first very small grains $a_{\rm min}$ = 0.05 to $a_{\rm max}$ = 1 micron and then only large grains $a_{\rm min}$ = 1 to $a_{\rm max}$ = 200 micron. They represent the two extremes of grain size distribution ranging from pristine ISM grains to conditions appropriate for more evolved dust in very old discs.

Dust opacities impact disc physics in two ways. First, increasing the average grain size decreases the opacity and thus the optical depth in the models. The dust temperature decreases mostly, except for the midplane regions inside 100 AU. However, the second — more important — effect is a decrease of effective grain surface area, thus decreasing the efficiency of gas-dust collisional coupling. As a consequence, the gas temperature decouples from the large grains even in the disc midplane, leading to higher gas temperatures everywhere and thus a vertically more extended disc. Given the fact that gas dust coupling is no longer efficient, the initial assumption that gas and dust are homogeneously mixed would have to be revisited. If most heating is provided by PAHs, this is not an issue as those will stay well mixed with the gas.

4.4 Line emission

In the following, we performed radiative transfer calculations on the grid of Herbig Ae disc models to understand the spatial and physical origin of the two GASPS tracers [C II], [O I], and the frequently observed sub-mm lines of CO. Besides a wealth of published CO observations of protoplanetary discs to compare to and test the physics and chemical networks of our models, the low rotational CO lines are part of ancillary projects to complement the Herschel GASPS project with tracers of the outer cold gas component in discs.

4.4.1 Far-infrared fine structure lines

[C II] 158 μm line

The fine structure line of ionized carbon arises in the outer surface layer of the disc. For values of $\chi/n_{\langle \rm H \rangle}$ smaller than 0.01, carbon turns atomic/molecular (see Fig. 4.2, left

Table 4.5: Results for the fine structure emission lines from various disc models. In the model column, MC, LTE and ES denote the use of level populations from Monte Carlo line radiative transfer, LTE and escape probability, respectively. Line and continuum fluxes are shown for a distance of 131 pc and an inclination of 45 degrees. Numbers in parentheses indicate powers of ten, i.e. 1.93(3) denotes 1.93×10^3.

		O I 63 μm		O I 145 μm		C II 157.7 μm	
M_{disc} [$M_\odot$]	Model	F_{line} [10^{-18} W/m^2]	F_{cont} [Jy]	F_{line} [10^{-18} W/m^2]	F_{cont} [Jy]	F_{line} [10^{-18} W/m^2]	F_{cont} [Jy]
$2.2\,10^{-2}$	MC	1.93(3)	1.44(2)	2.13(2)	1.25(2)	5.39(1)	1.14(2)
10^{-2}	MC	1.29(3)	1.03(2)	1.18(2)	6.57(1)	4.69(1)	5.91(1)
10^{-3}	MC	6.57(2)	2.58(1)	3.89(1)	8.84	2.98(1)	7.69
10^{-4}	MC	2.65(2)	4.56	8.06	9.09(-1)	1.40(1)	1.01
10^{-5}	MC	4.19(1)	9.89(-1)	1.11	1.72(-1)	4.53	2.71(-1)
10^{-6}	MC	1.99	1.50(-1)	5(-2)	3(-2)	2.77	1.43(-1)
10^{-2}	LTE	2.25(3)	1.05(2)	1.30(2)	6.63(1)	5.22(1)	5.96(1)
10^{-2}	ES	1.27(3)	1.05(2)	1.23(2)	6.63(1)	4.93(1)	5.96(1)
10^{-2}	T_{eff} = 9500 K	5.53(3)	1.68(2)	4.56(2)	8.60(1)	1.50(2)	7.63(1)
10^{-2}	T_{eff} = 10500 K	9.03(3)	1.78(2)	6.75(2)	8.85(1)	3.17(2)	7.84(1)
10^{-2}	$a_{min,max} = 0.01, 1$ μm	6.48(2)	1.42(2)	3.24(1)	3.53(1)	6.30(1)	2.85(1)
10^{-2}	$a_{min,max} = 1, 200$ μm	3.22(3)	1.44(2)	3.17(2)	7.21(1)	2.39(1)	6.42(1)

column). This limits the C^+ column density and hence the [C II] 158 μm line emission. Except in the very inner disc, $r < 1$ AU, the line never becomes optically thick. The line can be easily excited ($E_u = 91.2$ K) even in the disc surface at the outer edge; hence the total [C II] emission from the disc is dominated by the 100-700 AU range and probes the gas temperature in those regions ($T_{gas} \neq T_{dust}$). At these distances, the column density of C^+ decreases with disc mass leading to a potential correlation of the [C II] 158 μm line emission with total disc gas mass. However, it can also be shown that the total line emission depends sensitively on the outer disc radius (see Kamp et al. [2010]). The total [C II] line emission is thus degenerate for disc mass and outer radius. Due to the low critical density of this line, the emission forms largely under LTE conditions.

[O I] 63 and 145 μm lines

The [O I] emission is dominated by the 30-100 AU range, with gas temperatures of a few hundred K. For these regions, the 145 μm line becomes optically thin in the 10^{-3} and 10^{-4} $M_\odot$ disc models. LTE level population numbers systematically overestimate line fluxes by up to 70%. In the regions where most of the O I emission arises, the upper levels are significantly less populated than in LTE while the ground state is overpopulated with respect to LTE. The level population numbers computed with the simple escape probability assumption in ProDiMo yield only slightly higher line fluxes

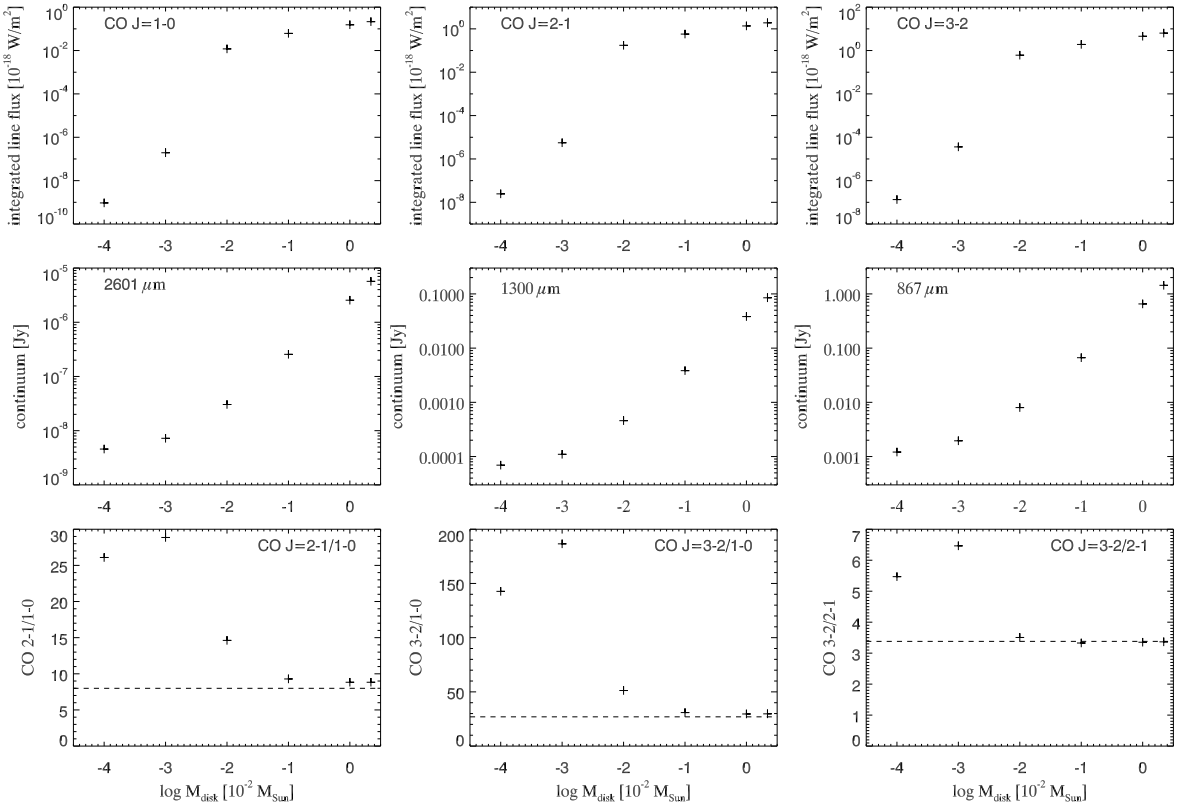

Figure 4.3: The top row shows integrated line fluxes as a function of disc mass, for (from left to right) the CO J=1-0, J=2-1 and J=3-2 rotational lines. The second row shows the continuum fluxes at the corresponding line center wavelengths as a function of disc mass. The third row shows the CO line ratios as a function of disc mass:(from left to right) J=2-1/1-0, J=3-2/1-0, J=3-2/2-1. Dashed lines indicate computed line ratios for optically thick lines in LTE.

than full Monte Carlo radiative transfer calculations, within 10 % for the O I lines and $\sim$ 5 % higher continuum fluxes. Since continuum differences should largely be due to the re-gridding, the estimated error stemming from the interpolation onto a different grid is of the order of 5 %.

4.4.2 CO sub-mm lines

Line fluxes have been calculated for the first three molecular transitions in CO, across the full mass range of disc models. The line fluxes and continuum fluxes are plotted as a function of disc mass in Fig. 4.3, and the J=3-2 line profiles from the 2.2×10^{-2} $M_\odot$, 10^{-3} $M_\odot$ and 10^{-4} $M_\odot$ models are plotted in Fig. 4.4.

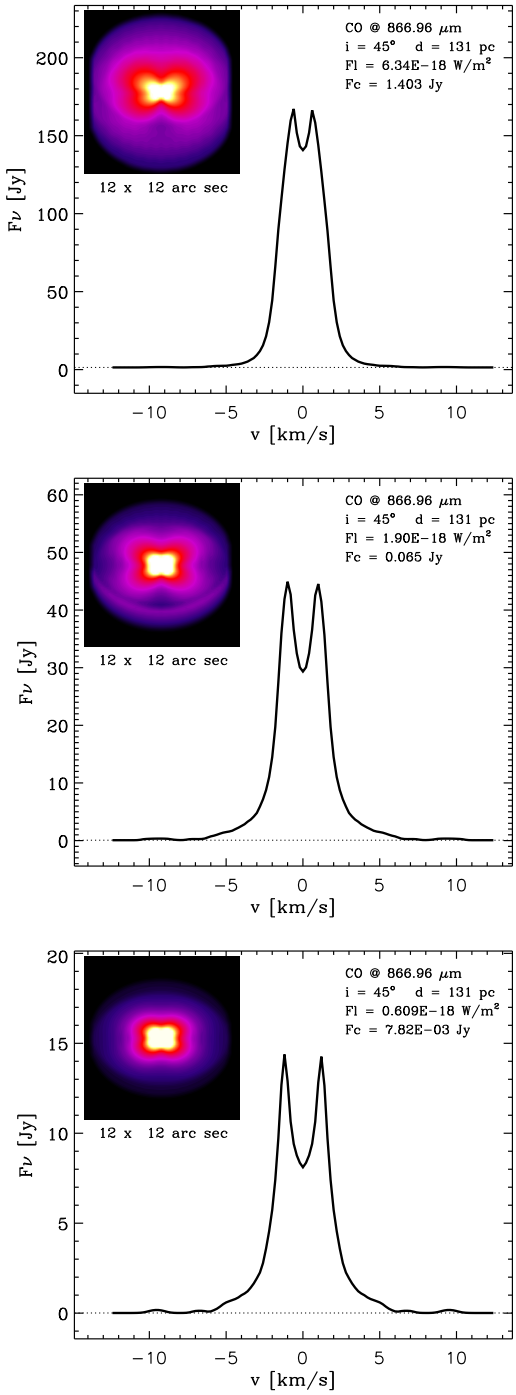

Figure 4.4: Top panel: CO J=3-2 line emission flux from the 2.2×10^{-2} $M_\odot$ model at a distance of 131 pc and an inclination of 45 degrees. The inserted image shows the continuum subtracted integrated logarithmic line intensity as a function of sky position. The angular size of 12" corresponds to 1570 AU at the distance of 131 pc. Middle panel: CO J=3-2 emission from the 10^{-3} $M_\odot$ model. Bottom panel: CO J=3-2 emission from the 10^{-4} $M_\odot$ model.

The J=1-0, J=2-1 and J=3-2 lines all show similar behaviour with disc mass, with the line fluxes initially increasing sharply with mass before levelling off for $M_{\rm disc} > 10^{-4}$ $M_\odot$. This similarity results in largely uniform line ratios, with a spike at 10^{-5} $M_\odot$. The continuum varies almost linearly with disc (and hence dust) mass, although with slightly more emission from the lower mass models than a strict linear relationship would give. This is due to the optically thin low mass discs having more penetrating UV dust heating in the midplane than the higher mass optically thick discs.

The calulated line fluxes all exhibit a jump of four orders of magnitude on moving from the 10^{-5} to the 10^{-4} $M_\odot$ model. This discontinuity is also seen in the line ratios, with all three exhibiting a significantly higher ratio for the 10^{-5} $M_\odot$ model than for the others. The sudden drop in emission below $10^{-4}M_\odot$ corresponds to a fall-off in A_V. There is suddenly almost no region in the disc with $A_V > 0.1$, resulting in a maximum CO abundance of less than 10^{-6} compared with $\sim 10^{-4}$ for the higher mass models. The small remaining region with $A_V > 0.1$ is quite hot, with gas temperatures around 500 K, giving a spike in the line ratios at 10^{-5} $M_\odot$.

Line formation regions

The three CO lines form at an intermediate height in the disc, between the warm upper layer and the cold midplane [see also van Zadelhoff et al., 2001] and are generally optically thick for disc masses down to 10^{-4} $M_\odot$. The submm line formation region is radially very extended, with significant contributions to the total line flux from the entire disc. The results of an experiment varying the outer radius of the disc region sampled in the re-gridding procedure are plotted in Fig. 4.5. The total J=3-2 line flux is seen to vary linearly with $R_{\rm out}$ indicating that the line originates from the full radial extent of the disc. The same behaviour is seen in the J=1-0 and J=2-1 lines. The linear trend is caused by a combination of the radial gas temperature gradient in the CO emitting layers and surface area. The continuum shows a slightly different behaviour, with a greater proportion of the integrated flux from outer radii.

The line profiles for the three transitions are generally very similar for a given disc model, and indeed across the computed mass range. Narrow peak separations (δv = $1-2$ km/s) indicate that the emission is coming from the entire disc inside $\sim$ 700 AU and will thus be dominated by the outer regions that contain more surface area.

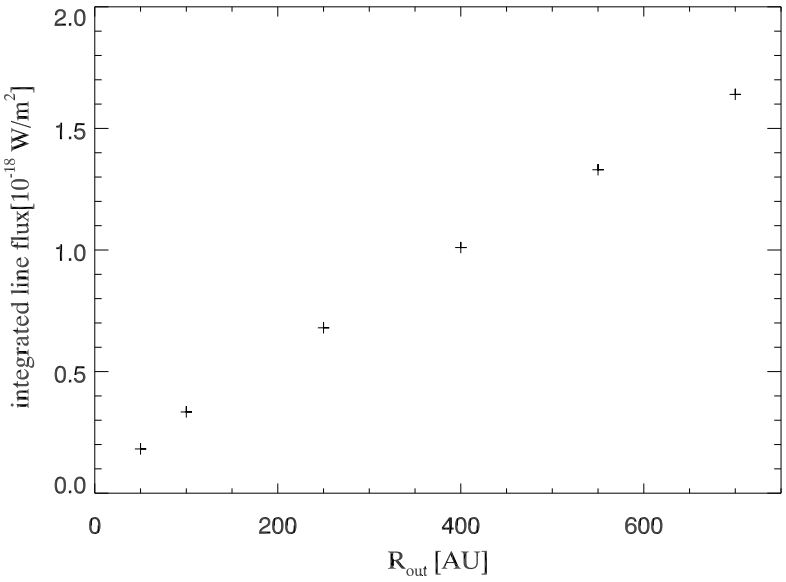

Figure 4.5: Integrated CO J=3-2 line flux for the $10^{-3}M_{\odot}$ model, plotted against the outer radius sampled by re-gridding.

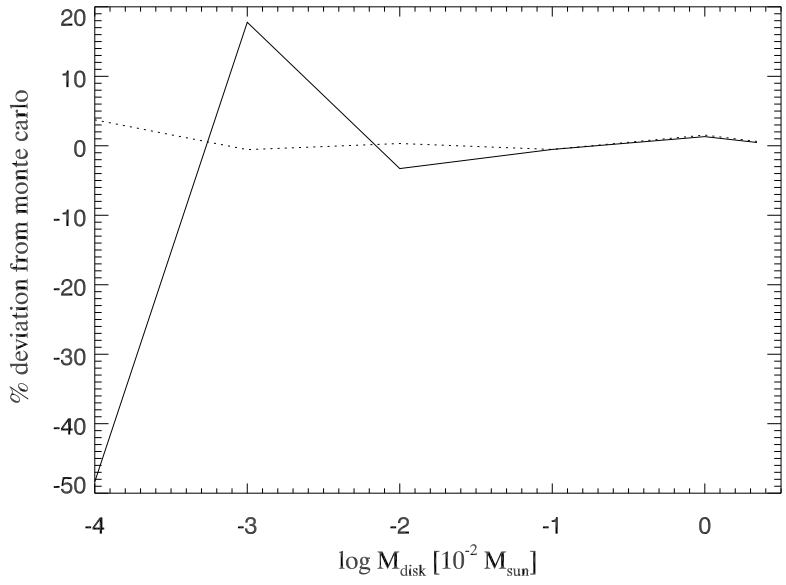

Figure 4.6: Relative difference in percent between Monte Carlo CO line fluxes and CO line fluxes calculated using the escape probabilty assumption (solid line) and between Monte Carlo CO line fluxes and LTE CO line fluxes (dotted line); results are shown as a function of disc mass.

LTE versus escape probability versus Monte Carlo

The continuum results obtained without re-gridding (ES) are in good agreement with those from the Monte Carlo radiative transfer, within 3% in all cases. This indicates that re-gridding does not present an issue when considering sub-mm fluxes. The escape probability line fluxes deviate slightly from the Monte Carlo and LTE fluxes for the low disc masses, up to ∼ 50% lower. This indicates again the limits of the two direction escape probability approach for the optically thin case of very tenuous discs.

The escape probability fluxes are however in good agreement (within 3%) for disc models with masses larger than10^{-4}M$_\odot$. The LTE line fluxes are also in good agreement (within ∼ 1%) for the entire mass range (see Fig. 4.6), indicating that LTE is a valid approximation for these low CO lines. However, $T_{\rm gas} = T_{\rm dust}$ is not a valid approximation for this set of disc models, because the gas temperatures in the outer regions, where the CO lines arise, deviate by up to a factor two from the dust temperatures (see Table 4.4 for mass averaged gas and dust temperatures of CO).

CO line ratios

To understand the values of the CO line ratios for high mass discs in Fig. 4.3, we start with a number of assumptions: 1) The continuum is small $I_{\rm cont} \ll I_\nu$; 2) The CO line forms under optically thick LTE conditions with a universal line profile $\phi(\nu)$ such that $I_\nu = B_\nu(T_{\rm gas})\,\phi(\nu)$ where B_ν is the Planck function; 3) The temperature $T_{\rm gas}$ is constant throughout the line forming region. The line flux can then be expressed as

$$F_{\rm line} = \iint (I_\nu - I_{\rm cont})\, d\Omega\, d\nu \;\approx A\, B_\nu(T_{\rm gas}) \int \phi(\nu)\, d\nu \;\;, \tag{4.1}$$

where A is the disc surface area as seen by the observer.

If we assume a square line profile function in velocity space such that $\phi(\nu) = 1$ if $-\frac{\Delta \rm v}{2} < {\rm v} < +\frac{\Delta \rm v}{2}$ and $\phi(\nu) = 0$ otherwise, we can re-write equation (4.1) in the Rayleigh-Jeans limit as

$$F_{\rm line} = A\, B_\nu(T_{\rm gas})\, \Delta\nu = A\, 2\, k\, T_{\rm gas}\, \Delta {\rm v} \frac{\nu^3}{c^3} \tag{4.2}$$

using $\frac{\Delta \rm v}{c} = \frac{\Delta \nu}{\nu}$. For line ratios, the quantities A, $T_{\rm gas}$ and Δv are identical, and hence

$$\frac{F_{\rm line,1}}{F_{\rm line,2}} = \left(\frac{\nu_1}{\nu_2}\right)^3 \;\;. \tag{4.3}$$

The corresponding values for the three CO line ratios are overplotted with dashed lines on Fig. 4.3, and agree indeed well with the limiting behaviour of the line ratios at high disc masses, $M_{\rm disc} \geq 10^{-3}$. Thus, we conclude that CO line formation in high mass discs occurs under optically thick LTE conditions. At lower masses the line ratios deviate from these values since the assumption of optical thick LTE no longer holds.

Changing the effective temperature of the central star or changing the dust properties affects the CO lines to a lesser extent than the fine structure lines. Changes to the continuum and the lines are generally within 50%. Even though the formation height of CO might change slightly, the excitation conditions are still close to LTE. While the CO mass in the models stays within a few percent of the original model (except in the ISM grain model, where it is 26% smaller) the CO mass averaged temperature changes up to a factor two. The effect on the line fluxes correlates directly with the temperature change, with the higher temperatures giving systematically higher fluxes. At these radio wavelengths, the change in continuum emission amounts to less than 25%, even between the models with different dust properties. The most extreme model is the one with an effective temperature of 10500 K where the mass averaged CO temperature rises to 110 K and hence the line fluxes increase by $\sim 60 - 70\%$.

4.5 Discussion

The goal of this study is a first assessment of the diagnostic power of the fine structure lines of neutral oxygen, ionized carbon and of the CO sub-mm lines in protoplanetary discs. This work prepares the ground for a systematic analysis of a much larger and more complete grid of protoplanetary disc models. Based on the detailed radiative transfer calculations of the previous section, we discuss here the potential of the various lines in the context of deriving physical disc properties such as gas mass, gas temperatures and disc extension.

4.5.1 Far-infrared fine structure lines

From detailed two dimensional modelling of protoplanetary discs, Woitke et al. [2009a] conclude that the [O I] 63 μm line alone provides a useful tool to deduce the gas temperature in the surface layers of protoplanetary discs, especially the hot inner disc surface. However, spatially unresolved observations that measure only integrated [O I] 63 μm line fluxes in sources at typical distances of 140 pc will not be able to detect

the presence of hot gas very close to the star (inside $\sim$ 10 AU). This work shows that the total line flux is dominated by emission coming from the cooler outer regions.

The [O I] 63/145 line ratio increases towards lower masses (10 for $\sim 10^{-2}$ $M_\odot$ to 40 for $M_{disc} < 10^{-4}$ $M_\odot$). In addition this ratio is not sensitive to the disc outer radius for $R_{out} > 100$ AU, which suggests that it could be used as a gas mass tracer. Using only small sub-micron sized grains (similar to the ISM composition) increases the line ratio by a factor two, thus mimicking a disc mass that is lower by more than a factor ten. However, the grain size distributions chosen here present the extreme ends and are easily distinguished from looking at the SED.

The [C II] 158 μm line emission is a very sensitive tracer of the outer disc radius. Due to its low excitation temperature, this line is also strongly affected by confusion with any type of diffuse and molecular cloud material in the line of sight. The problem can be addressed with Herschel/PACS by using the surrounding pixels on the detector (5×5 pixels with the disc being spatially unresolved) for a reliable off-source flux determination.

The [O I] 63/[C II] 158 ratio depends even more on disc mass than the [O I] 63/145 line ratio. It would thereby be a prime diagnostic for relative disc mass estimates. However, while the ratio of the two oxygen lines does not change very much with disc outer radius, the [O I] 63/[C II] 158 ratio does depend strongly on it. Because of this degeneracy with disc size, the diagnostic value of this ratio alone is limited for individual objects. Its use would require the a-priori knowledge of many other disc parameters such as the disc outer radius, grain sizes and composition. Rather we suggest that it could be used in a statistical way on a large sample of discs that share the same classification group, e.g. based on their IR SEDs. Alternatively, a combination of the [O I] 63/145 and [O I] 63/[C II] 158 line ratios could be used to break the degeneracy with disc size [see also Kamp et al., 2010].

4.5.2 CO sub-mm lines and line ratios

The low excitation CO rotational lines are often used to prove the existence of primordial gas in protoplanetary disc and in combination with optically thin line of isotopologues to measure the total gas mass [e.g. Thi et al., 2001, Panić et al., 2008]. Due to the high Einstein A coefficients and high abundances of ^{12}CO in molecular regions, the low rotational CO lines become optically thick at low A_V. Thus, they originate mainly in the optically thin disc surface [van Zadelhoff et al., 2001], where

gas and dust temperature decouple according to our models. However, as in the case of the [C II] line, CO submm lines can be contaminated by low density cold remnant cloud material. The amount of contamination can be estimated either from offset positions for single dish observations or through interferometry.

Isotopologues of CO have much lower abundances of $^{12}CO/^{13}CO = 77$ in the ISM [Wilson and Rood, 1994] and even higher values of 100 in discs [selective photodissociation; see for most recent work Smith et al., 2009, Woods and Willacy, 2009, Visser et al., 2009]. Thus, they can probe deeper into the disc and are — in the absence of freeze-out — excellent tools for measuring the disc mass. Panić et al. [2008] use for example the optically thin ^{13}CO J=2-1 line from the disc around the Herbig star HD 169142 to infer a disc mass of $(0.6 - 3.0) \times 10^{-2}$ $M_\odot$.

Our analysis shows indeed a relatively flat relationship for the ^{12}CO lines with disc gas mass, confirming thus that the low rotational CO lines by themselves are not a good tracer of gas mass (Fig. 4.3). The lines become optically thick even at very low disc masses and hence a reliable inversion of the line fluxes to infer gas mass proves impossible. Similarly there are degeneracies in the computed line ratios J=2-1/1-0, J=3-2/1-0 and J=3-2/2-1 which suggest limitations in the diagnostic power of these line ratios.

The CO lines can be used to measure independently the outer disc radius (Sect. 4.4.2) and thus mitigate the problem of employing the [C II] 158 line for disc diagnostics. Dent et al. [2005] and Panić and Hogerheijde [2009] demonstrate the power of single dish CO observations in deriving disc outer radii and inclinations, thus constraining SED modeling that is rather insensitive to $R_{\rm out}$ and degenerate for inclination and inner radius. Hughes et al. [2008b] note that the outer radius derived from dust continuum observations is always smaller than that derived from CO emission lines. Even though they can explain this within homogeneous gas and dust models ($R_{\rm out}$(gas) = $R_{\rm out}$(dust) and a realistic outer edge, i.e. an exponential density profile), this finding reveals the problems in mixing quantities deduced from dust and gas observations. Since C^+ and CO arise both from the gas in the outer disc, we do not need to rely on dust observations, but can instead use a gas tracer to measure the gas outer disc radius.

The [C II] line probes in general slightly higher layers than the CO lines; hence the model results suggest that we can trace the vertical gas temperature gradient in discs. Table 4.4 shows that for the most massive discs, $\langle T_{C^+} \rangle$ is 50% larger than $\langle T_{CO} \rangle$.

4.5.3 Comparison with observations for MWC480

Since we used the Herbig star MWC480 to motivate our choice of parameters, we briefly discuss the line emission from the models together with observations available from the literature. The goal is not to obtain a best-fitting model, but to provide an impression of the model results within the observational context. Table 4.6 gives an overview of selected observational data for MWC480 (detections and upper limits) from the literature. The CO mass derived from ^{13}CO 3-2 is 1.7×10^{-4} $M_\odot$ and the total gas mass derived from the 1.3 mm continuum flux is $(2.2 \pm 1.0) \times 10^{-2}$ $M_\odot$ [Thi et al., 2001]. The ^{12}CO and ^{13}CO lines suggest an outer disc radius of $\sim$ 750 and $\sim$ 500 AU, respectively [Piétu et al., 2007].

The oxygen fine structure lines are not detected with the ISO satellite [Creech-Eakman et al., 2002]. Assuming the ISO instrumental resolution as FWHM of a potential line (0.3 μm for $\lambda < 90$ μm, 0.6 μm for $\lambda > 90$ μm), the ISO 3σ upper limits for the [O I] lines can be derived from

$$F_{\text{upper limit}} \approx 3\sigma \sqrt{0.5\pi}\ \text{FWHM}\ \text{W/m}^2 \quad . \tag{4.4}$$

This gives values of 4.14×10^{-16} and 1.35×10^{-16} W/m^2 for the 63 and 145 μm line, respectively. The upper limit for the 63 μm line is only a factor 1.6 smaller than the flux predicted from the 10^{-3} $M_\odot$ disc model. The 145 μm upper limit is less sensitive and hence even consistent with our 10^{-2} $M_\odot$ disc model. Changing the outer disc radius to 500 AU does not affect the [O I] lines.

The observed [C II] line is much stronger than in any of our models, suggesting indeed significant contamination from diffuse background material in the large ISO beam (80”).

Our 2.2×10^{-2} $M_\odot$ model overpredicts the CO J=3-2 line flux by approximately one order of magnitude. By reducing the maximum grain size, the total grain surface area increases and dust and gas temperatures couple in the region where this CO line forms; thus yielding $\langle T_g \rangle \sim 40$ K and a factor two lower line fluxes. Another factor two can each be gained by reducing the total disc mass and the disc outer radius to 500 instead of 700 AU.

The observed continuum flux at 1.3 mm is a factor 4 smaller than computed from the 2.2×10^{-2} $M_\odot$ disc model. Reducing again either the total disc mass or the maximum grain size, reduces the modeled continuum fluxes to the right value.

Table 4.6: Observed fluxes for MWC480

Type	λ	Flux	Reference
O I	63 μm	$\leqslant 1.1\,10^{-15}$ W/m^2/μm	(1)
O I	145 μm	$\leqslant 1.8\,10^{-16}$ W/m^2/μm	(1)
C II	158 μm	$5.9 \pm 0.6\,10^{-16}$ W/m^2	(1)
		$5.5 \pm 0.4\,10^{-16}$ W/m^2	(2)
CO	345 GHz	2.88 K km/s	(3)
		$4.23\,10^{-19}$ W/m^2	(*)
cont.	1.3 mm	360 ± 24 mJy	(4)
cont.	2.7 mm	39.9 ± 0.8 mJy	(4)

References: (1) Creech-Eakman et al. [2002], (2) Lorenzetti et al. [2002], (3) Thi et al. [2004], (4) Mannings and Sargent [1997].

(*) $\int T_{\rm mb}\,dv = 10^{-2}\,\lambda_{\rm cm}/(2k)\,(\Omega_a)^{-1}\int F_\nu({\rm W/m^2/Hz})\,d\nu$, with Ω_a being the solid angle of the beam, i.e. $\pi(13.7"/2)^2$ for the JCMT.

To conclude, by tuning the input parameters, the models can get close to the observed continuum as well as line fluxes, thus providing additional confidence that the models capture the essential physics and chemistry of protoplanetary discs. Hence, besides studying physics and chemistry of protoplanetary discs in a more general context, these models can also be used in the detailed analysis of individual objects that possess a larger set of continuum and line observations.

4.6 Conclusions

A limited series of Herbig Ae disc models has been computed in order to study the origin and diagnostic value of the gas line tracers [C II], [O I] and CO. This study does not include the effects of X-ray irradiation, grain settling or mixing. Even though X-rays are generally of minor importance for Herbig stars, grain settling and large scale mixing processes could affect the conclusions. The effect of grain settling will be included in a forthcoming larger model grid (see Chapter 5), but mixing processes need to be addressed with dynamical time-dependant models. The Monte-Carlo radiative transfer code RATRAN is used to compute line profiles and integrated emission from various gas lines.

The main results are:

- The [C II] line originates in the disc surface layer where gas and dust temperatures are decoupled. The total line strength is dominated by emission from the disc outer radius. Thus the 157.7 μm line probes mainly the disc extension and outer disc gas temperature. The line forms in LTE.

- The [O I] lines originates also in the disc surface layer even though somewhat deeper than the [C II] line. The main contribution comes from radii between 30 and 100 AU. The [O I] lines form partially under NLTE conditions. Differences in line emission from escape probability and Monte Carlo techniques are smaller than 10%.

- CO submm lines are optically thick down to very low disc masses of $< 10^{-4}$ $M_\odot$ and form mostly in LTE. $T_{\rm gas} = T_{\rm dust}$ is not a valid approximation for these lines. Differences in line emission from escape probability and Monte Carlo techniques are smaller than 3%, except in the case of very optically thin disc models (10^{-5} and 10^{-6} $M_\odot$).

- The [O I] 63/145 μm and [O I] 63/[C II] 158 μm line ratios trace disc mass in the regime between 10^{-2} and 10^{-6} $M_\odot$. Since the [C II] 158 μm line is very sensitive to the outer disc radius, the [O I] 63/[C II] 158 μm is degenerate in that respect and its use requires additional constraints from ancilliary gas and/or dust observations. The sensitivity of these two line ratios to the dust grain sizes underlines the importance of using SED constraints along with the gas modeling to mitigate the uncertainty of dust properties.

- A combination of the [O I] 63/145 μm and [O I] 63/[C II] 158 μm line ratios can be used to diminish the degeneracy caused by an unknown outer disc radius.

- Neither total CO submm line fluxes nor line ratios can be used to measure the disc mass. However, the low rotational lines studied here provide an excellent tool to measure the disc outer radius and can thus help to mitigate the degeneracy between gas mass and outer radius found for the [O I] 63/[C II] 158 μm line ratio.

Chapter 5

The DENT Model Grid

5.1 Introduction

In this chapter I describe work in which I contributed to the efforts of GASPS, a large international syndicate. GASPS refers to Gas in Protoplanetary Systems, the first extensive, systematic survey of gas in circumstellar discs that covers the transition between initial gas-rich discs through to gas-poor debris discs. It utilises the Photodetector Array Camera and Spectrometer (PACS), one of three instruments aboard the Herschel space observatory. GASPS consists of a two-phase PACS study, surveying the fine structure lines of [C II]158μm and [O I]63μm in 240 objects, followed by observations of [O I]145μm and the far-infrared CO and H_2O rotational lines in the brightest sources. The dust continuum is also measured using 70 and 160μm photometry, to define the SED in the same wavelength range as the line data. The sample includes discs with masses of a few $\times 10^{-2}$ $M_\odot$ down to 10^{-5} $M_\odot$, ages 1-30 Myr, and stellar spectral types B2 through M4.

In order to interpret the survey data, the program has involved extensive disc modelling. This includes the computation of a grid of $\sim$300000 models spanning parameter space, in order to seek trends across the various models and help team members interpret the observational data in the context of a comprehensive set of model predictions. This work takes the approach described in Chapter 4 and expands it to a large multi-parameter analysis. I have acted as the main developer of `xDENT`, a graphical user interface for analysing and plotting the huge quantity of grid data, and for fitting the model data to observations. The first DENT grid results are published in the *MNRAS* letter "Continuum and line modelling of discs around young stars, I. 300

Table 5.1: Parameters of the DENT grid and values assumed. $R_{\rm subli}$ stands for the dust sublimation radius (where $T_{\rm d} = 1500\,{\rm K}$). The choice of inclination angles represents a randomly oriented sample.

stellar parameters		
$M_\star$	stellar mass [$M_\odot$]	0.5, 1.0, 1.5, 2.0, 2.5
age	age [Myr]	1, 3, 10, 100
$f_{\rm UV}$	excess UV, $f_{\rm UV} = L_{\rm UV}/L_\star$	0.001, 0.1
disc parameters		
$M_{\rm d}$	disc dust mass [$M_\odot$]	10^{-7}, 10^{-6}, 10^{-5}, 10^{-4}, 10^{-3}
$\rho_{\rm d}/\rho_{\rm g}$	dust/gas mass ratio	0.001, 0.01, 0.1, 1, 10
$R_{\rm in}$	inner disc radius [$R_{\rm subli}$]	1, 10, 100
$R_{\rm out}$	outer disc radius [AU]	100, 300, 500
ϵ	column density $N_{\rm H}(r) \propto r^{-\epsilon}$	0.5, 1.0, 1.5
H_0	scale height [AU]	*fixed*: 10 $r_0 = 100$ AU
β	disc flaring $H(r) = H_0 \frac{r}{r_0}^\beta$	0.8, 1.0, 1.2
dust parameters		
$a_{\rm min}$	minimum grain size [μm]	0.05, 1
$a_{\rm max}$	maximum grain size [μm]	*fixed*: 1000
s	settling $H(r,a) \propto H(r) a^{-s/2}$	0, 0.5
inclination angle		
i	0° (face-on), 41.4°, 60°, 75.5°, 90° (edge-on)	

000 disc models for Herschel/GASPS" by Woitke, Pinte, Tilling et al. [2010], which includes figures produced using `xDENT`. This is also the case for the two subsequent DENT grid papers by Kamp, Woitke, Pinte, Tilling et al. [2010] and Pinte et al. [2010].

5.2 Grid Computation

The DENT (Disc Evolution with Neat Theory) grid is a tool to investigate the influence of stellar, disc and dust properties on continuum and line observations and to study the extent to which these dependencies can be inverted. The grid is designed to coarsely sample the parameter space associated with young intermediate to low mass stars, with discs ranging from gas-rich through to gas-poor debris discs. The 11 variable input parameters (+ 2 fixed parameters) required to specify the star-disc system are given in Table 5.1. The observable quanities recorded for each of the grid models are listed in Table 5.2.

The model input stellar parameters are the mass and age, with corresponding

Table 5.2: List of output quantities: monochromatic continuum fluxes $F_{\rm cont}$ and integrated, continuum-subtracted line fluxes $F_{\rm line}$.

observable	wavelengths [μm]
$F_{\rm cont}$	57 wavelength points between 0.1 μm and 3500 μm
OI	63.18, 145.53
CII	157.74
^{12}CO	2600.76, 1300.40, 866.96, 650.25, 520.23, 433.56, 371.65, 325.23, 289.12, 260.24, 144.78, 90.16,79.36, 72.84
o-H_2O	538.29, 179.53, 108.07, 180.49, 174.63, 78.74
p-H_2O	269.27, 303.46, 100.98, 138.53, 89.99, 144.52

effective temperatures and luminosities taken from the evolutionary models of Siess et al. [2000]. The photospheric input spectra are taken from Kurucz stellar atmosphere models of solar abundance, with an additional UV component to account for accretion and/or chromospheric activity in young stars. This UV excess is defined as $f_{\rm UV} = L_{\rm UV}/L\star$ where $L_{\rm UV} = \int_{91{\rm nm}}^{250{\rm nm}} L_\lambda d\lambda$ is the UV luminosity with assumed spectral shape $L_\lambda \propto \lambda^{0.2}$. The UV excess component has a significant impact on the disc chemistry and heating. It would thus be desirable to include more $f_{\rm UV}$ values in the grid, analogous to the range of accretion rates found in Mayne and Harries [2010], which cover six orders of magnitude in a model grid examining the dust continuum emission from accreting brown dwarves. However, the additional gas disc parameters in the DENT grid, coupled with the obvious computational constraints, mean that a simple two-value comparison will have to suffice at present.

The disc shape, density structure and dust properties are defined parametrically as outlined in Table 5.1, with dust grain opacities taken from Draine and Lee [1984]. The discs are assumed to be passive, i.e. there is no viscous heating. The grid models do not contain PAHs, which will in general tend to give slightly cooler discs.

The DENT grid was computed using ProDiMo interfaced with the Monte Carlo radiative transfer code Mcfost [Pinte et al., 2006]. In total the grid comprises 323020 disc models and SED calculations. A total number of 1610150 line flux calculations have been carried out for 29 spectral lines under 5 inclinations. See Woitke et al. [2010] for further details concerning the modelling process.

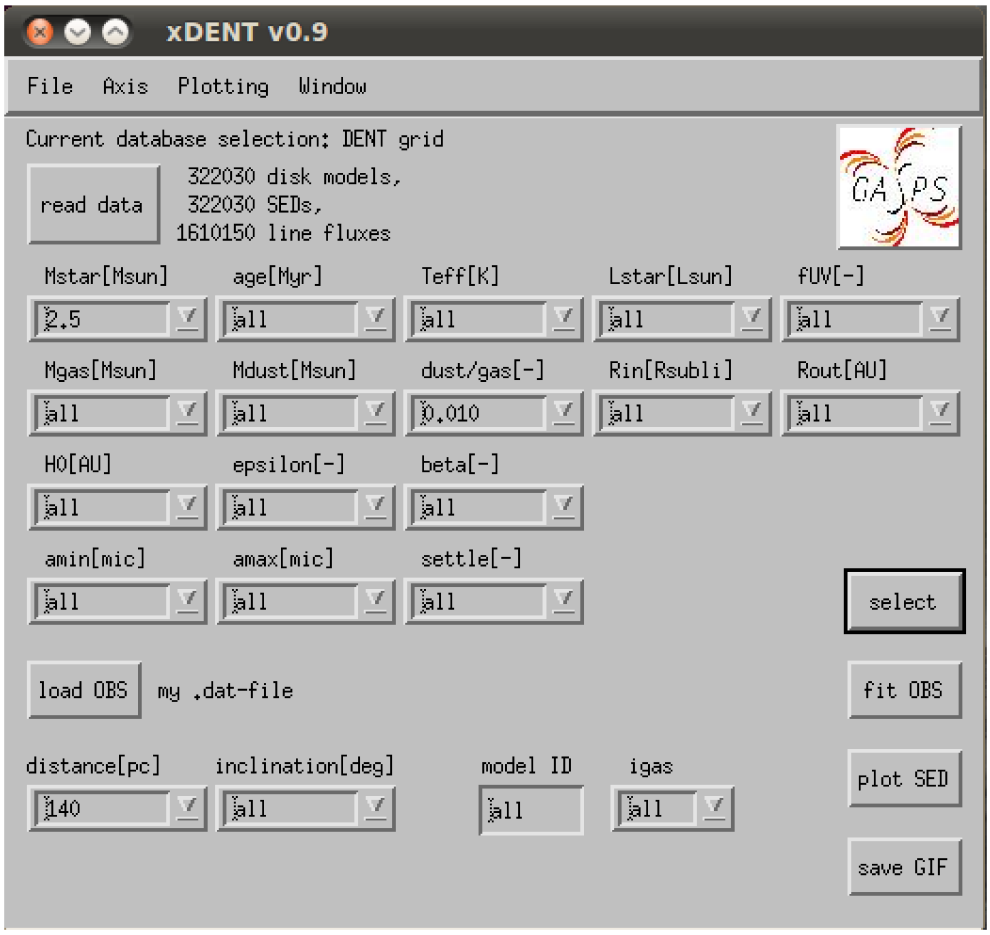

Figure 5.1: `xDENT` main menu.

5.3 xDENT

`xDENT` is a graphical user interface for visualising the DENT grid data. It is written as an `idl` widget, and has been used by the GASPS team to analyse the data and produce figures for a number of publications. `xDENT` allows users to select subsets of grid models, and plot the various input parameter values and observables in a number of formats. Users are also able to fit the grid models to observed line and continuum data. All plots produced using `xDENT` are fully customisable; there is an option to output the `idl` source code for a particular plot, which can be edited to change the plot axes, colours, labels etc. The main features of `xDENT` are outlined in the following sections.

5.3.1 Model selection

The `xDENT` main menu (see Fig. 5.1) lists all model parameters, and allows the user to narrow down the selection of grid models used for plotting and/or fitting. For each parameter the desired models can be selected either by specifying a single value for that parameter from a pull-down menu, or by typing a range of values into the appropriate field. For example, typing "`<=2`" into the $M_{\rm star}$ field will select all models with stellar mass greater than or equal to $2\,{\rm M}_{\odot}$, and typing "`1E-4--1E-2`" into the $M_{\rm disk}$ field selects all models with disc mass between 10^{-4} and $10^{-2}\,{\rm M}_{\odot}$.

As well as filtering the grid models by input parameter value, users can specify up to four observable quantities, with an allowed range of values for each, to narrow down the model selection. Individual models of interest (e.g. from fitting) can be selected by typing the model ID into the appropriate field.

5.3.2 Plotting

Scatter plot

This function plots the data for the selected models on axes specified by the user (see Fig. 5.2). The axes can denote any one of the model input parameters, continuum or line predictions, species masses or mass-averaged species temperatures, or the ratio of any two of these. The plotted points can also be colour-coded according to a third parameter, in up to 8 colour bins. The user can specify the axes ranges, and whether the data is plotted linearly or logarithmically.

If any individual points in a plot are of interest to the user, they can click that point with the cursor. This causes the terminal to print the model ID and model input parameters, as well as the species masses and some key observables. The point is marked in the plot by its model ID so as to avoid confusion (see Fig. 5.3).

Histogram

In addition to plotting individual data points, `xDENT` users can plot histograms using all or a subset of the DENT grid models. The variable selected for the x-axis is split into a number (40 by default) of evenly-spaced (log or linear) bins, and `xDENT` plots the number of models inside each bin. An additional variable can be used to further discretise the results, in which case a specified number of colour-coded histograms are plotted on the same axes (see Fig. 5.4).

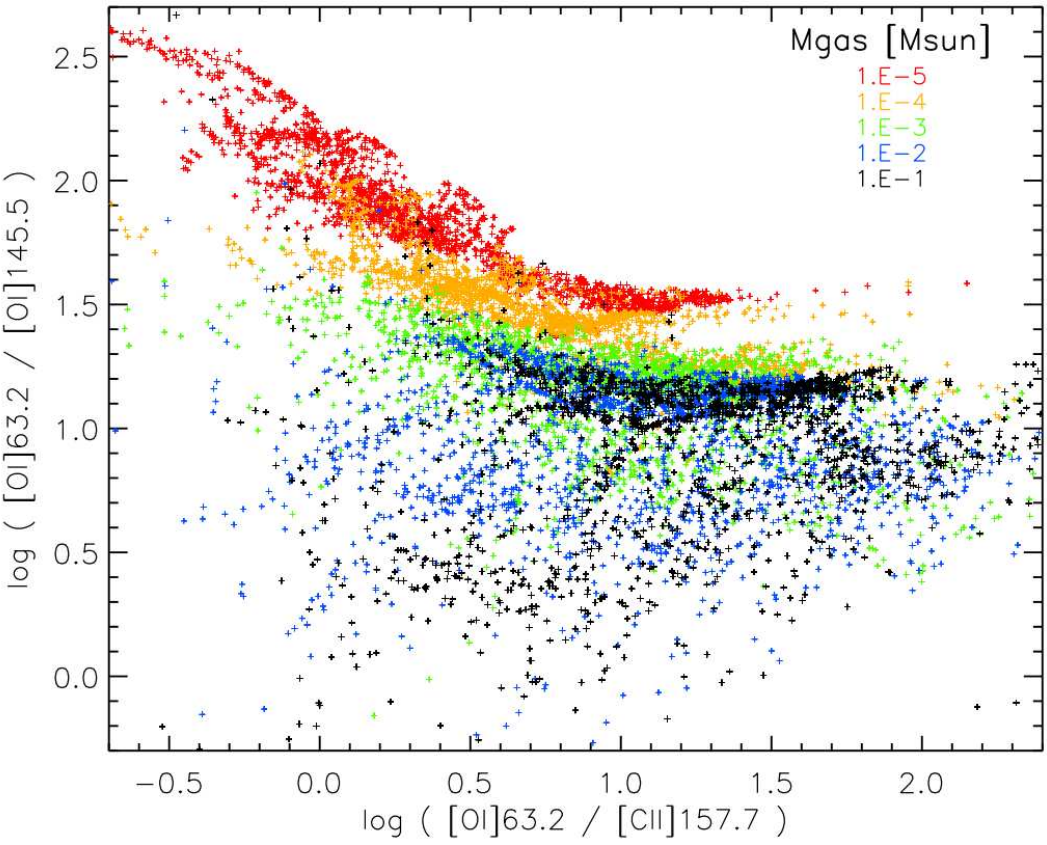

Figure 5.2: Two colour line flux diagram, [OI] 63/145μm versus [OI] 63/[CII] 158μm, of a sub-selection of 10740 DENT models with $\rho_{\rm d}/\rho_{\rm g} = 0.01$, $\epsilon = 0.5$, $s = 0.5$, inclination angle 41°. Colour-coded is the disc gas mass.

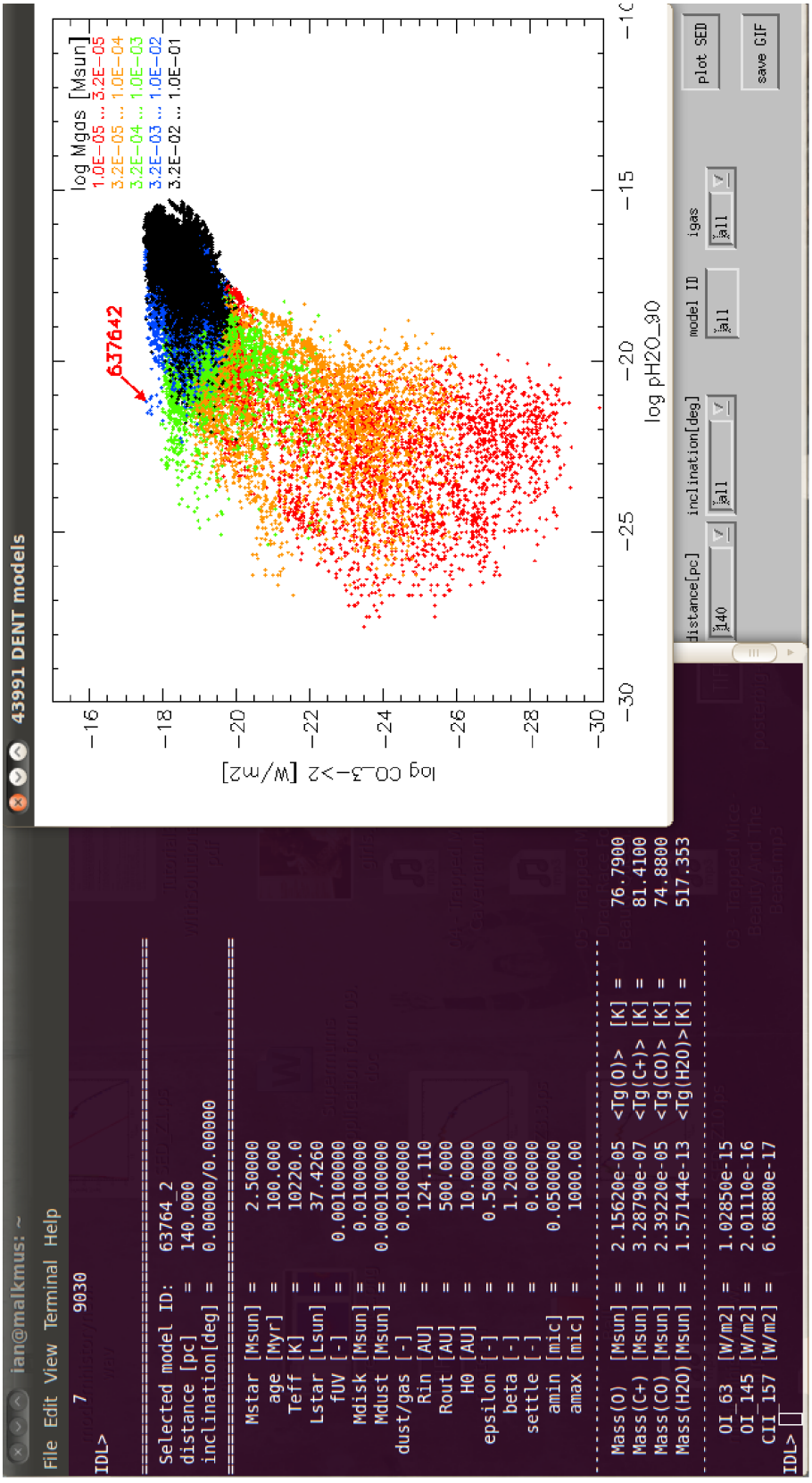

Figure 5.3: Model information function in xDENT.

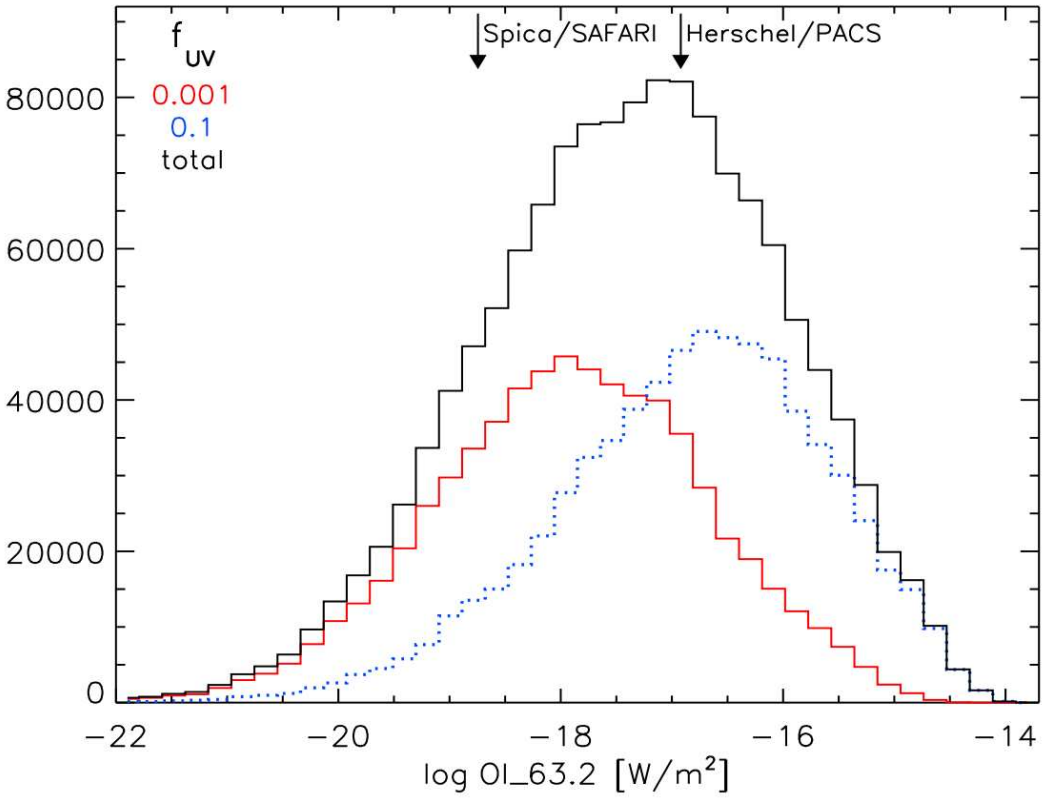

Figure 5.4: Dependence of [OI] 63.2μm line flux on the stellar UV excess $f_{\rm UV}$. The black histogram counts the DENT models that result in certain [OI] 63.2μm fluxes at distance 140pc in 40 log-equidistant bins. The red histogram represents the low $f_{\rm UV} = 0.001$ models, and the blue dotted his- togram the high $f_{\rm UV} = 0.1$ models. The difference between high and low UV excess causes a difference of about 1-1.5 orders of magnitude in line flux. The arrows show the (3σ, 0.5h) detection limits of SPICA/SAFARI and HERSCHEL/PACS.

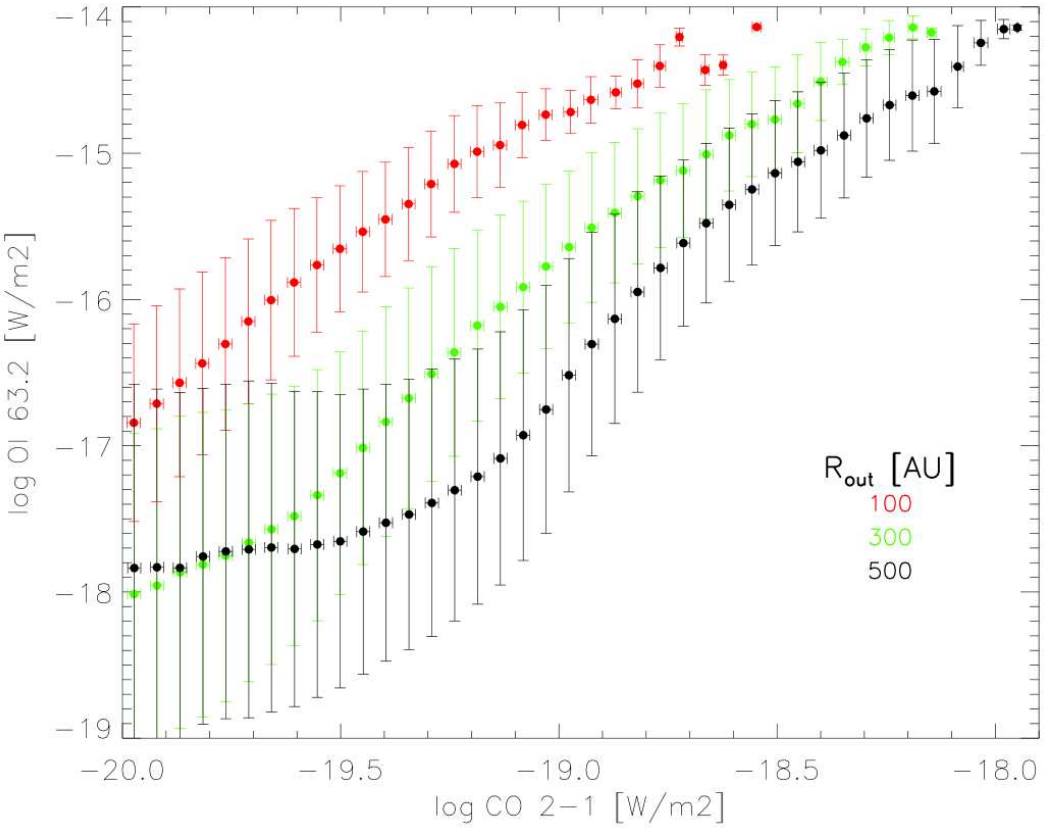

Figure 5.5: [OI] 63μm emission plotted against ^{12}CO J=2-1 line emission for a selection of disc models. The models are binned in the *x*-direction, and the mean values and standard deviations in the *x* and *y*-directions are plotted. The models are further divided by outer disk radius, colour-coded with values of 100, 300 and 500 AU.

Plot means

In certain situations, with a large number of overlapping points, the scatter plots can become rather difficult to interpret. The "plot means" option in `xDENT` is an alternative style of plot which is intended to respresent the data more clearly in such situations. The *x*-axis is split into ~ 40 equidistant bins (again log or linear spacing). Each bin is then analysed, and `xDENT` plots the mean *x* and *y* variable values, with error bars to indicate the *x* and *y* standard deviations in a particular bin. As for the other plotting options, an additional variable can be used to colour-code the plots (see Fig. 5.5).

5.3.3 Model fitting

`xDENT` also has the option of fitting the model outputs to observations. The coarse nature of the DENT model grid means that it is not well-suited to detailed model fitting. Rather, the fitting feature in `xDENT` allows users to identify a range of interest in parameter space, to direct further research with e.g. a more finely-spaced model grid covering that range of values. The detailed fitting of disc models to individual target observations is covered extensively in Chapter 6, but this is outwith the aims of the DENT grid.

`xDENT` users can specify any combination of observed line and/or continuum fluxes and upper limits, and the program calculates for each model the following logarithmic measure of deviations between model predictions and observations

$$\begin{aligned} \chi^2 &= \frac{1}{N}\sum_{i=1}^{N}\Delta_i^2 \qquad \text{with} \\ \Delta_i &= \begin{cases} \dfrac{\log(F^i_{\rm mod}/F^i_{\rm obs})}{\log(1+\sigma^i_{\rm obs}/F^i_{\rm obs})} & , F^i_{\rm obs} \geq 3\sigma^i_{\rm obs} \\ \dfrac{F^i_{\rm mod}}{\sigma^i_{\rm obs}} & , F^i_{\rm obs} < 3\sigma^i_{\rm obs} \end{cases} \end{aligned} \tag{5.1}$$

where $F^i_{\rm obs}$ and $\sigma^i_{\rm obs}$ are the observed flux and its error respectively, and $F^i_{\rm mod}$ is the flux predicted by the model. The sum in equation 5.1 is carried out over the total number of observed fluxes provided by the user. The grid models are fitted to the observations by finding the model with the minimum χ^2 value.

The use of this modified χ^2 quantity to select the best-fitting models was motivated by the huge range in values for each observable quantity predicted by the model grid. Typically an observed data point will have models predicting values several orders of magnitude in each direction, and this logarithmic χ^2 discriminates evenly between values which are too high and too low. The standard χ^2 definition was found to favour models which predicted values less than that which was observed. When fitting to observed upper limits it is no longer possible to use this method, and χ^2 is defined simply as the ratio of the predicted flux and the observed error [Woitke et al., 2011]. Due to difficulties arising from switching between these two definitions, the observed upper limits are not used for my later model fitting efforts (see chapter 6), and I instead use only the logarithmic χ^2 definition from 5.1.

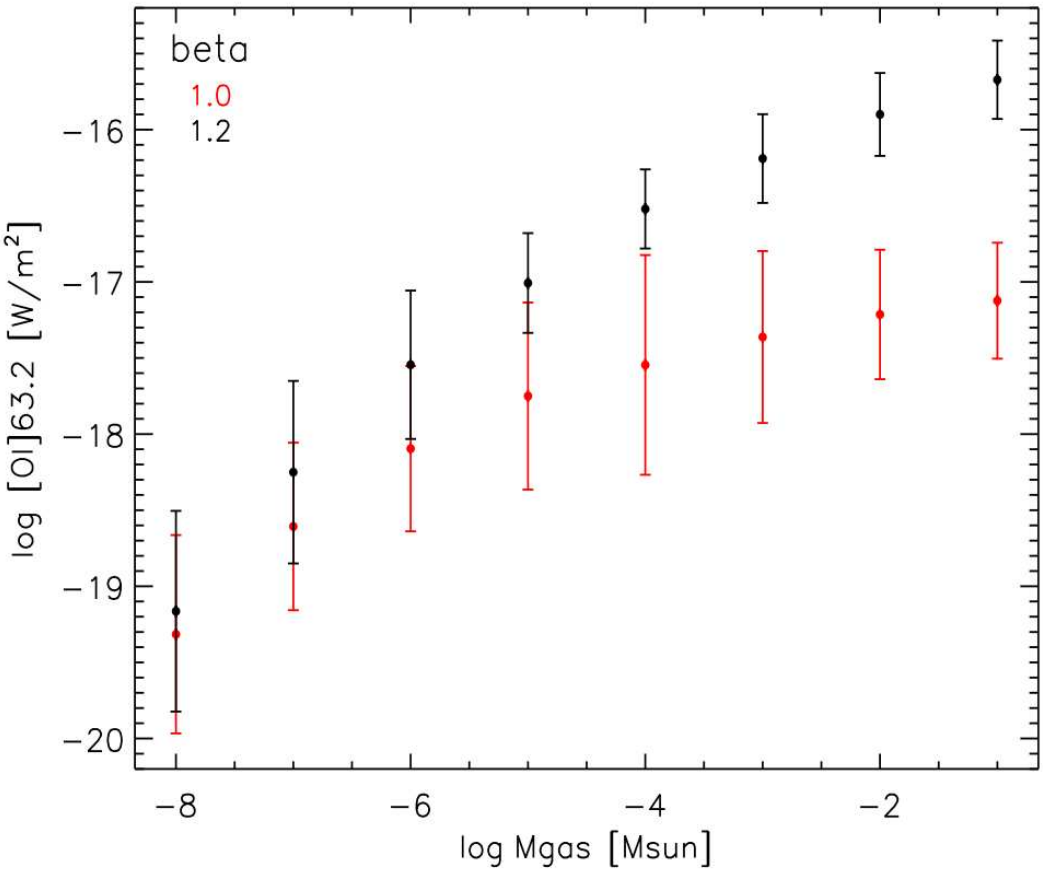

Figure 5.6: Dependence of [OI] 63.2μm line flux at distance $d = 140$ pc on the flaring parameter β, as function of total disc gas mass $M_{\rm gas}$. A sub-selection of 3456 T Tauri models is plotted ($M_\star \leq 1\,{\rm M}_\odot$, $age \leq 1$ Myr, $f_{\rm UV} = 0.1$, $R_{\rm in} = R_{\rm subli}$, $s = 0$, inclination angle $\leq 60°$).

5.4 Results

The DENT model grid data have been used in a number of studies to seek parameter dependencies, with an ultimate aim to be able to invert these dependencies and infer the disc properties from observations. All of these studies have used `xDENT` as an analytical tool, and to produce figures for publication. I summarise here some of the key findings from the DENT model grid.

Woitke et al. [2010] show that the calculated emission line fluxes are strongly dependent on the assumed stellar UV excess and disc flaring. Fig. 5.4 splits the entire sample of DENT grid models into two groups: those with large UV excess emission, $f_{\rm UV} = 0.1$, and those with $f_{\rm UV} = 0.001$, and measures the [OI] 63.2μm line emission

from each. It is seen that the difference in UV excess leads to a difference of 1-1.5 orders of magnitude in line flux. This can be attributed to the increased UV emission heating the warm disc surfaces, leading to a brightening of the emission lines. The dependence on UV excess is less pronounced for Herbig Ae/Be stars, which have a photospheric soft UV component.

This line is also shown to be sensitive to the disc flaring in Fig. 5.6, which plots the calculated [OI] 63.2μm line flux for a subset of T Tauri discs with $f_{\rm UV} = 0.1$, as a function of disc mass. At low disc masses the discs are optically thin, and the disc flaring has only little influence on the line emission. However, in the more massive, optically thick discs, the line fluxes from the flared and non-flared discs are seen to diverge. The line fluxes from the discs with strong flaring ($\beta = 1.2$) continue to increase with increasing mass, whereas the non-flared discs ($\beta = 1$), in which the disc surface is shadowed by the inner disc regions, begin to saturate with increasing disc mass due to increased shadowing. The flared discs have warm surface layers which are illuminated by stellar light, giving stronger [OI] 63.2μm emission. Woitke et al. [2010] propose that for massive T Tauri discs, high [OI] 63.2μm fluxes are a safe indicator of flaring of the gas disc.

Kamp et al. [2011] also use `xDENT` to study the [OI] 63.2μm line emission from discs, and find it to be on the whole a reasonable tracer of gas mass. However, for massive non-flaring, settled disc models without UV excess, this line is found to suffer from self-absorption in the cool upper disc layers. In addition, the [CII] 158 μm fine structure line is strongly dependent on the stellar UV flux, and the presence of a UV excess, due to this line forming in the photoionised gas in the thin disc surface layer. Kamp et al. [2011] propose that the sensitivity of the lines to the UV excess and disc flaring can be by-passed to an extent by taking the ratios of lines which are equally affected by these parameters. This is the case in Fig. 5.2, which shows a two-colour line flux diagram in which the [OI] 63 & 145 μm lines and the [CII] 158 μm line are able to distinguish between different disc masses, for a large subset of the DENT grid models. However, for many objects the [OI] 145 μm and [CII] 158 μm lines will not be available, since they are often more than a factor of 10 fainter than the [OI] 63.2μm line, and so Kamp et al. [2011] also look at the low rotational CO lines. These are found to trace the disc outer radius, as I found in Chapter 4, albeit for a much more limited sample of models. In particular the CO J=2-1/[OI] 63.2μm line ratio is found to correlate with the disc outer radius, and this correlation with $R_{\rm out}$ can be clearly seen

in Fig. 5.5.

Pinte et al. [2010] compare the DENT grid data to the first set of GASPS observations, comprising Herschel/PACS line data obtained for a small sample of objects with discs. These results confirm the prediction from the DENT grid, that the line fluxes are strongly affected by the UV excess in T Tauri stars, and the stellar UV for Herbig stars. This study also highlights the considerable parameter degeneracies present in the DENT grid, and notes the difficulties and potential pitfalls when attempting to interpret line observations and invert them into physical parameters. A better understanding of the various degeneracies might be obtained by deriving the Spearman's rank correlation coefficient for each pair of free parameters, as was carried-out recently by Mayne et al. [2012]. In any case, it is necessary to combine far-IR line observations with the low rotational sub-mm transitions of CO, and continuum data, in order to break these degeneracies. I follow this approach in Chapter 6, in which I carry out detailed model fitting to a large sample of data for a single object, in order to attempt to derive the disc properties.

Chapter 6

Gas Modelling in the Disc of HD 163296

6.1 Introduction

In this chapter I continue my attempts to better-understand the physical conditions inside Herbig discs, using a different approach. While the previous two chapters have employed a statistical approach - using large samples of disc models to seek overall trends across the various observable quantities - in the following I instead focus on one particular object, attempting detailed model fits to the available observations of the Herbig Ae star HD 163296. These observations include new Herschel/PACS far-infrared data obtained as part of the GASPS program, as well as a large number of additional line and continuum data. The work described in this chapter is published in the *Astronomy & Astrophysics* paper "Gas Modelling in the Disc of HD 163296" by Tilling et al. [2011].

The Herschel/PACS data reduction described in Section 6.2 was carried out by Gwendolyn Meeus. The stellar parameter determination described in Sections 6.3.1–6.3.4 was carried out by Benjamin Montesinos, Aki Roberge and William Vacca. This was an important part of this study however, since accurate stellar parameters and knowledge of the stellar UV emission are crucial in modelling the gas chemistry and heating. The MCFOST model used to check the disc PAH emission in Section 6.5.2 was computed by Christophe Pinte.

One important disc property for planet formation models is the amount of gas present as it evolves. The dust characteristics are generally better-understood than

Table 6.1: Observed line data with HERSCHEL/PACS. Detections are listed as $F_L \pm \sigma$) whereas non-detections quote $< 3\sigma$. There is an additional absolute flux calibration error of 30%. In the case of the [CII] 158 μm line, strong contamination from the surrounding background prevented us from estimating a meaningful upper limit.

Species	λ [μm]	ν [GHz]	Line Flux [10^{-18} W m^{-2}]	Continuum (RMS) [Jy]
OI	63.18	4745.05	193.1 ± 5.8	16.46 ± 0.07
OI	145.52	2060.15	< 8.5	22.12 ± 0.03
CII	157.74	1900.55	–	23.90 ± 0.05
p-H_2O	89.99	3331.40	< 9.4	19.14 ± 0.04
o-H_2O	179.52	1669.97	< 14.5	22.28 ± 0.08
o-H_2O	180.42	1661.64	< 16.2	21.58 ± 0.09
o-H_2O	78.74	3810.01	< 15.0	21.00 ± 0.10
OH	79.11	3792.19	< 17.0	20.70 ± 0.10
OH	79.18	3788.84	< 17.0	20.60 ± 0.10
CO J=36-35	72.85	4115.20	< 11.6	17.30 ± 0.03
CO J=33-32	79.36	3777.63	< 22.8	18.12 ± 0.07
CO J=29-28	90.16	3325.12	< 11.1	19.10 ± 0.05
CO J=18-17	144.78	2070.68	< 13.1	22.05 ± 0.04

the gas, and the ISM gas/dust mass ratio of 100 is often adopted to give an estimate of the gas mass. However, gas masses derived from millimetre and sub-mm CO emission observations are typically lower than from dust observations with this assumption, sometimes by a factor ~ 100 [Thi et al., 2001]. This is variously attributed to gas depletion due to photoevaporation or planet formation, and CO freeze-out on grains [Zuckerman et al., 1995, Kamp and Bertoldi, 2000]. These low level rotational CO transitions are also strongly dependent on the disc size, and often optically thick under certain disc conditions, limiting their ability to probe the deeper disc layers [Panić and Hogerheijde, 2009, Hughes et al., 2008b]. In order to better constrain the disc gas mass it is necessary to observe additional gas species, such as those observable in the far-infrared. The FIR range is a crucial observing window which can help to resolve some of these ambiguities. The fine structure lines of atomic oxygen and ionised carbon probe the gas in the warm disc surface layers, and as products of CO photodissociation provide a good test for this proposed explanation of CO under-abundance. In addition, the high level rotational transitions of CO arise from warm gas in the inner disc, probing different disc regions to the low level mm CO lines.

In addition to the discrepancy between gas mass estimates from millimetre

continuum and CO observations, there is uncertainty regarding the derived disc outer radii from CO and continuum observations. The outer radius suggested by model fits to dust emission is often found to be smaller than that of the gas disc. In the case of the Herbig Ae star AB Aurigae, Piétu et al. [2005] suggested that a change in dust grain properties, leading to reduced opacity in the outer disc, could explain this discrepancy. For HD 163296, Isella et al. [2007] attributed the apparent difference in disc radii to a sharp drop in surface density, opacity or dust-to-gas ratio beyond 200 AU, while Hughes et al. [2008b] proposed that the apparently conflicting dust and gas observations could be reconciled using a different treatment of the disc surface density at the outer edge, motivated by similarity solutions for the time evolution of accreting discs. This study attributed smaller derived disc radii from dust observations to detector sensitivity thresholds, arguing in favour of larger dust discs, albeit with an exponentially-tapered density at the outer edge. A steepening of the density profile in the outer disc has also been observed in the case of DM Tau, LkCa 15 and MWC 480 by Piétu et al. [2007].

HD 163296 is an isolated Herbig Ae star with spectral type A1Ve, mass $\sim 2.5\,M_\odot$ and stellar luminosity $\sim 38\,L_\odot$ (this work), situated at a distance of $118.6^{+12.7}_{-10.0}$pc [van Leeuwen, 2007]. Scattered light and millimetre continuum observations indicate the presence of an inclined circumstellar disc extending out to a radius of 540AU [Mannings and Sargent, 1997, Grady et al., 2000, Wisniewski et al., 2008]. In addition, there is evidence of an asymmetric outflow perpendicular to the disc, with a chain of six Herbig-Haro knots tracing its mass-loss history [Devine et al., 2000]. The derived disc dust mass is in the range $(5-17)\times10^{-4}M_\odot$ [Natta et al., 2004, Tannirkulam et al., 2008a, Mannings and Sargent, 1997, Isella et al., 2007].

Recent near-infrared studies of the inner disc of HD 163296 indicate an inner dust rim feature enclosing a bright emission region extending inwards towards the star. This emission inwards of the dust rim has been attributed to an optically thin inner disc, although there is uncertainty regarding the size and composition of such a disc. Derived radii for the dust rim lie in the range (0.2 – 0.55) AU [Renard et al., 2010, Eisner et al., 2009, Tannirkulam et al., 2008b, Benisty et al., 2010, Monnier et al., 2006]. An increase in opacity at the inner rim due to sublimation of grains could cause the rim to puff up, and it has been suggested that this leads to time-variable self-shadowing of the outer disc [Sitko et al., 2008, Wisniewski et al., 2008]. Mid-infrared imaging of warm dust in the disc surface layers seems to indicate little flaring [Doucet

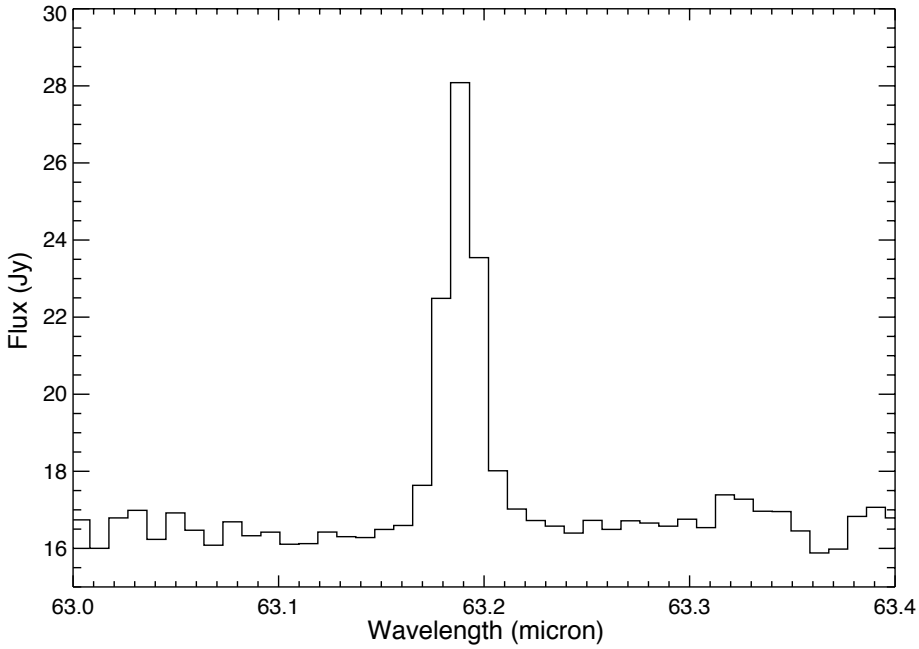

Figure 6.1: Observed [OI]63μm emission line with Herschel/PACS.

et al., 2006], and scattered light brightness profiles are consistent with a non-flared outer disc [Wisniewski et al., 2008]. Fits to the ISO-SWS spectra of HAeBe discs led Meeus et al. [2001] to classify HD 163296 as one of their group II objects, in which an optically thick inner disc shadows the outer disc from stellar radiation, resulting in a non-flared geometry.

In this study I aim to fit a wide variety of observed emission lines and the dust spectral energy distribution (SED) simultaneously with a disc with this observed geometry.

6.2 Herschel/PACS Observations

We have obtained observations of HD 163296 in the far-infrared using Herschel/PACS, consisting of spectroscopic line observations and photometry. These include a detection of the [OI] 63 μm fine structure line, and upper limits for a number of other atomic, ionic and molecular far-IR lines. We observed HD 163296 with the PACS spectrometer in line spectroscopy mode (obsid 1342192161, 1252 sec, 3 repetitions) and range scan mode (obsid 1342192160, 5141 sec, 3 repetitions), while chopping and nodding.

Table 6.2: Photometric fluxes observed with Herschel/PACS. These observations (AORS 1342228401 and 1342228401) are done with the standard miniscan.

λ [μm]	70	160
Flux [Jy]	18.5±3.3	20.2±4.0

The spectra were reduced using HIPE version 7.0, with the standard pipeline scripts for a chopped line scan of a point source. The reduction steps include division by the spectral response function and MedianOffsetCorrection, as the new flat fielding task is not yet robust for short range scans such as the present observations (PACS instrument team, private communication). For this study, we only make use of the data contained in the central spaxel, to which we apply a wavelength-dependent correction factor for the loss of flux due to diffraction losses. With these additional steps, the absolute flux calibration accuracy is 30% (see PACS Spectroscopy Performance and Calibration Document, http://herschel.esac.esa.int/AOTsReleaseStatus.shtml).

The line fluxes and upper limits are given with continuum data in Table 6.1. The PACS photometry data are given in Table 6.2. Comparison of the azimuthally averaged radial profiles with the observed point spread function (PSF), using Vesta, show that the disc is unresolved at both 70μm and 160μm. The spatial extent of the observed [OI] 63 μm emission is illustrated in Fig. 6.2, where it can be seen that the emission is dominated by the central 9.4×9.4 arcsecond spaxel. This corresponds to a maximum radial extent of 560 AU for the emission.

The pipeline reduction of the [CII] 158 μm range shows this line in absorption, which is unexpected. Therefore, we also looked at the unchopped spectra in the different chop positions. It is clear that the region around HD 163296 is full of [CII] 158 μm emission, and that this causes the emission feature at the position of the star to cancel out (and even become an absorption feature). This is likely due to cloud material along the line-of-sight, since HD 163296 is located close to the Galactic plane, and is consistent with the presence of CO emission at radial velocities offset from this object, but unresolvable with PACS [Thi et al., 2001]. We also inspected all the other lines for their unchopped appearance, but did not find contamination through the offset positions in those cases.

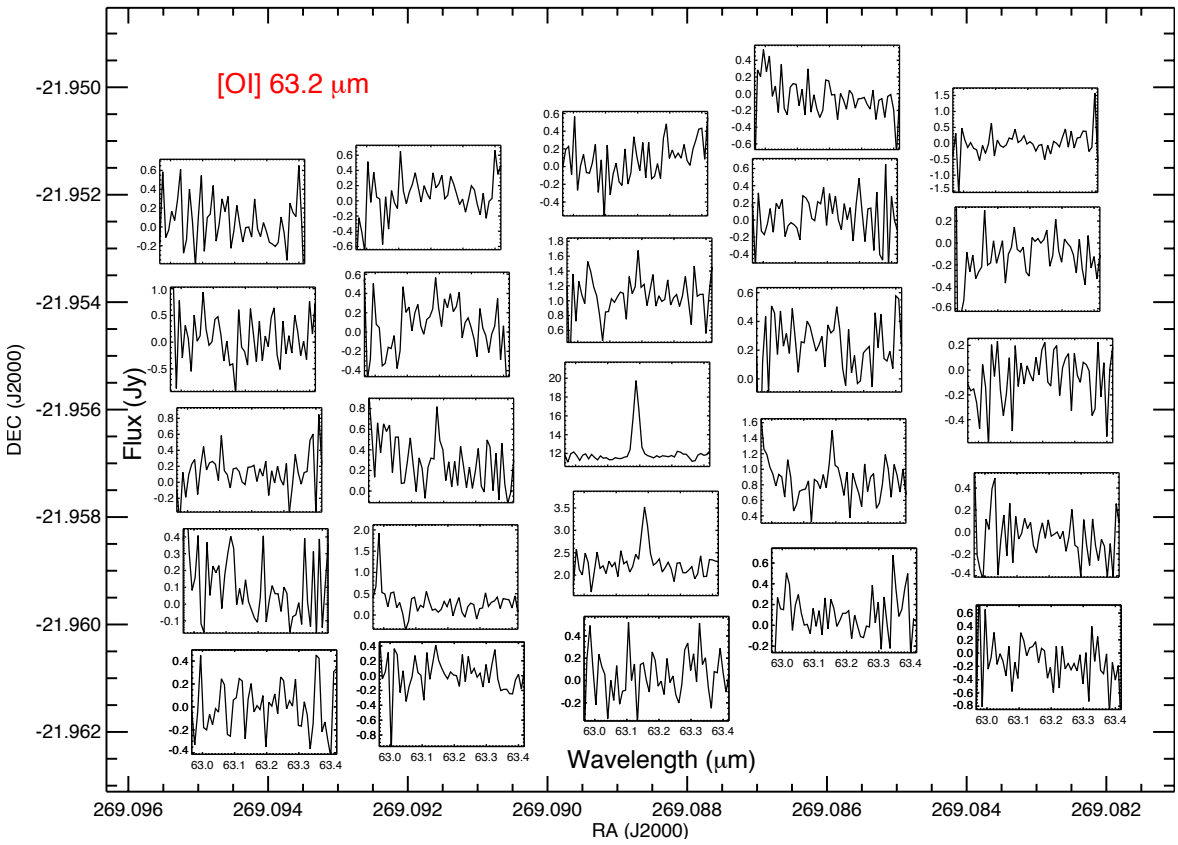

Figure 6.2: [OI]63μm spectra observed by Herschel/PACS towards HD 163296. Each spectrum corresponds to a 9.4×9.4 arcsec pixel centered at the given coordinates. Emission is dominated by the central pixel, corresponding to a maximum outer radius of ∼ 560AU, assuming a distance of 118.6 parsecs to this object.

Table 6.3: Parameters for HD 163296.

Temperature	9250 ± 150 K
Gravity ($\log g_*$)	4.07 ± 0.09
Metallicity ([Fe/H])	$+0.20 \pm 0.10$
Mass	$2.47 \pm 0.10\ M_\odot$
Luminosity	$37.7 \pm 7.0\ L_\odot$
Age	4.2 ± 0.4 Myr

6.3 Properties of HD 163296

The study of the disc of HD 163296 is directly linked to the knowledge of the absolute parameters of the star itself and the behaviour of the spectral energy distribution (SED) in the ultraviolet (UV), optical and near infrared (near-IR), which is mostly dominated by stellar radiation; in particular, the energy emitted at wavelengths shorter than 2500 Å is a fundamental piece of information used to model the disc, due to its impact on the photo-chemistry and gas heating [Woitke et al., 2010]. This section describes the stellar properties and studies the spectral energy distribution at the range mentioned above.

6.3.1 Stellar parameters

The determination of the stellar parameters of HD 163296 was done in an extensive work devoted to the study of a sample of Herbig Ae/Be stars [Montesinos et al., 2009]. Details of the methodology followed and the observations used can be found in that paper. We outline in this section the relevant steps of the process.

An iterative distance-independent algorithm based on the analysis of the SED and optical high-resolution spectra (for the estimation of the effective temperature and metallicity), and mid-resolution spectra of the Balmer lines Hβ, Hγ and Hδ (for the estimation of the gravity), was applied.

The knowledge of the effective temperature, gravity and metal abundance allows us to place the star in a $\log g_* - \log T_{\rm eff}$ diagram and superimpose the appropriate set of evolutionary tracks and isochrones for that specific metallicity [Yi et al., 2001]. This gives directly – or after a simple interpolation between the tracks and isochrones enclosing the position of the star – the stellar mass and the age. Since there is a one-to-one correspondence between a pair ($T_{\rm eff}$, g_*) on a given track and a pair ($T_{\rm eff}$, $L_*/L_\odot$), the stellar luminosity can also be estimated.

Table 6.4: Photometry for HD 163296.

Band	λ (μm)	Magnitude and error	Flux and error (Jy)
U	0.360	6.95 ± 0.03	3.00 ± 0.08
B	0.440	6.92 ± 0.04	7.27 ± 0.27
V	0.550	6.86 ± 0.03	6.56 ± 0.18
R	0.640	6.73 ± 0.05	6.26 ± 0.29
I	0.790	6.67 ± 0.10	5.48 ± 0.51
J	1.215	6.17 ± 0.05	5.55 ± 0.26
H	1.654	5.49 ± 0.05	6.69 ± 0.31
K	2.179	4.71 ± 0.05	8.56 ± 0.39

Table 6.3 gives the stellar parameters of HD 163296 after a slight refinement of the results presented in Montesinos et al. [2009], incorporating an analysis of the foreground extinction.

6.3.2 The SED: UV, optical and near-IR observations

Simultaneous optical UBVRI and near-infrared JHK photometry obtained as part of the EXPORT collaboration [Eiroa et al., 2001, Oudmaijer et al., 2001], were used to build the optical and near-IR photospheric spectral energy distribution of HD 163296. Table 6.4 shows the wavelengths, magnitudes and corresponding fluxes with their uncertainties. The calibration from magnitudes to fluxes has been done using the zero points given by Bessell [1979] for the optical and Cox [1999] for the near-IR magnitudes.

Ultraviolet IUE spectra of HD 163296 were extracted from the INES archive[1]. From the collection of 68 SW and LW (for "short" and "long wavelength") spectra in low resolution, obtained through the large aperture of the spectrograph, all those that looked clean (few or no bad pixels) and with the correct exposure classification codes were selected. The spectra (SW+LW) cover the range 1250–3000 Å.

A high-resolution, far-UV spectrum of HD 163296 was constructed by combining data taken with HST STIS and FUSE. The STIS spectra, covering 1150 Å to 3000 Å, were obtained from the HST STIS Echelle Spectral Catalog of Stars (StarCat[2]). The FUSE spectrum of HD 163296 is extremely noisy below 970 Å; therefore, we used only the portion between that wavelength and 1150 Å in our high-resolution composite

[1] http://sdc.cab.inta-csic.es/ines/
[2] http://casa.colorado.edu/~ayres/StarCAT/

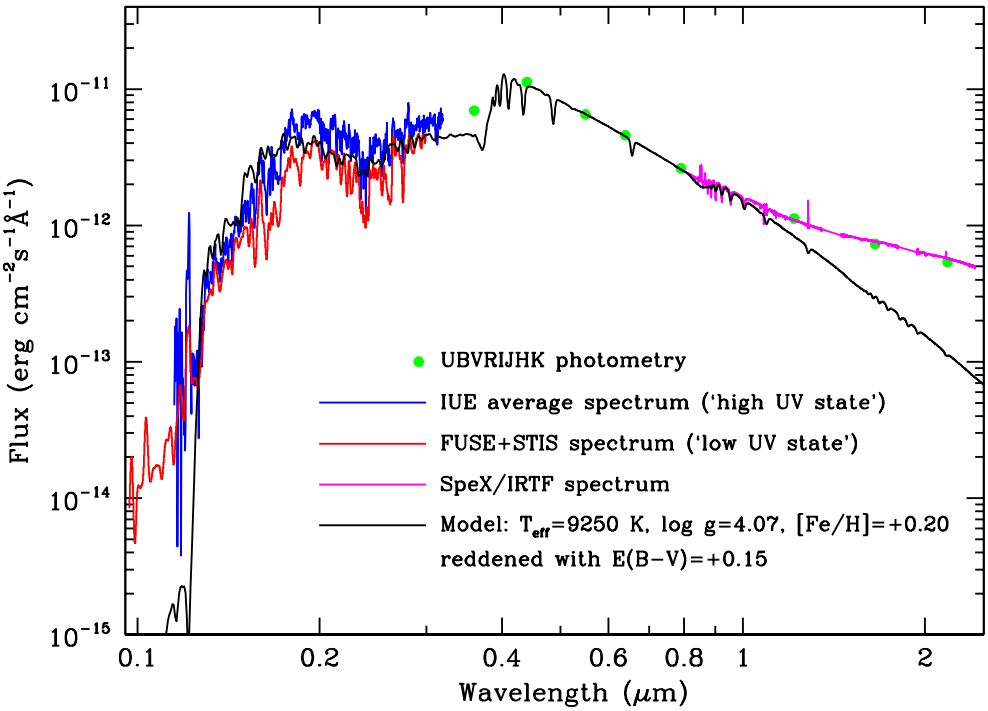

Figure 6.3: Spectral energy distribution for HD 163296. The green dots represent the fluxes corresponding to the UBVRIJHK photometry. The size of the dots is of the order or larger than the uncertainties. The IUE average spectrum and the FUSE+STIS spectrum are plotted in blue and red, respectively; the latter has been slightly smoothed to reduce the noise. The SpeX/IRTF spectrum is plotted in magenta. The black solid line is a photospheric model computed for the specific stellar parameters given in Table 6.3, reddened with E(B–V)=+0.15 and normalized at the flux in V. See text for details.

UV spectrum for HD 163296. FUSE spectra contain strong terrestrial airglow emission lines, due to the large size of the observing aperture. We removed these lines from the HD 163296 spectrum before stitching it to the STIS spectrum.

A comparison of the IUE and FUSE+STIS spectra shows that they differ in the level of their continuum. The IUE spectra with the largest flux levels are a factor ~ 1.6 higher than the FUSE+STIS spectrum, therefore, regarding the modelling, the ultraviolet contribution of the star will be represented by two different UV input spectra, namely a "low UV" state, corresponding to the FUSE+STIS spectrum, and a "high UV" state, corresponding to the average of the highest IUE spectra[3] (see section 6.4.1).

In addition, a near-infrared spectrum of HD 163296 was obtained at the NASA

[3]The average IUE spectrum was build with the following individual spectra: SWP 28805, SWP 28811, SWP 28813 and LWR 02065.

Infrared Telescope Facility (IRTF) on Mauna Kea on 2010 July 8 with SpeX [Rayner et al., 2003]. Ten individual exposures of the target, each lasting 32 s, were taken using the short-wavelength cross-dispersed (SXD) mode of SpeX. This mode yields spectra spanning the wavelength range 0.8–2.4 μm divided into six spectral orders. The slit width was set to 0.″3, which yields a nominal resolving power of 2000 for the SXD spectra. Observations of HD 156717, an A0 V star, used as a "telluric standard" to correct for absorption due to the Earth's atmosphere and to flux calibrate the target spectra, were obtained immediately preceding the observations of HD 163296. The airmass difference between the observations of the object and the standard was 0.06. The seeing was estimated to be $\sim$ 0.″3 – 0.″5 at 2.2 μm during the observations and conditions were clear. The statistical S/N varies across the spectral range but is of the order of several hundred over the entire SXD spectrum. The SpeX data were reduced with Spextool [Cushing et al., 2004] and the telluric correction was performed using the procedures and software described by Vacca et al. [2003].

Figure 6.3 shows the SED of HD 163296. The solid black line is a photospheric model computed for $T_{\rm eff}$ = 9250 K, $\log g_*$ = 4.07 and [Fe/H]=+0.20 from the GAIA grid of models created with the PHOENIX code [Brott and Hauschildt, 2005]. The model has been reddened with E(B–V)=+0.15 ($R_{\rm V}$ = 3.1); this will be discussed in section 6.3.4.

6.3.3 Spectral type from the ultraviolet and near-infrared spectra

Despite the fact that the precise determination of the stellar parameters has been done through a careful analysis of a variety of observations, as we have mentioned in section 6.3.1, an attempt to determine the spectral type of HD 163296 in a more qualitative way has been done using the ultraviolet and near-infrared spectra.

A comparison of the ultraviolet data with IUE spectra of stars classified as "spectral-type standards" was done . The spectra were taken from the "IUE Ultraviolet Spectral Atlas of Standard Stars"[4] [Wu et al., 1983, 1992]. It is interesting to note that below 2000 Å, for a given spectral type, the ultraviolet spectra of the "spectral-type standards" themselves are very different, in particular for A0 V and A1 V. If we consider only the region above 2000 Å, the comparison suggests that HD 163296 is closer to A3 V (and possibly slightly later), however, if a mild extinction is present, the UV spectra would be also close to that of A1 V stars. A larger extinction would

[4]http://www-int.stsci.edu/~jinger/iweb/proj/project.html

push the spectral type determination towards earlier spectral types.

A similar exercise of spectral typing was done by a comparison of the SpeX spectrum in the YJ bands (0.85 – 1.35 μm) with Kurucz synthetic models (see Montesinos et al. [2009] for references regarding the synthesis codes and models used). The spectrum is complex, the range of $T_{\rm eff}$'s explored with the Kurucz models (8750–9250 K, corresponding to A3V and A1V) does not produce significant Paschen line variations. The Paschen line wings of HD 163296 are narrower than in any of the models, which would suggest temperatures of 9250 K or higher. The metallic lines are faint, their typical intensity being lower than 5% that of the continuum. Some lines are deeper than in any photospheric spectrum, which suggests the presence of some circumstellar absorption. Some lines are much fainter, which suggests an spectral type A1V or earlier, or dust emission veiling. Good agreement is rarely found. Although we fail to find a unique combination of $T_{\rm eff}$ and $\log g$ that provides an adequate fit to both the UV and NIR spectra of HD 163296, all data are consistent with an A1-A3 star, seen through mild foreground extinction.

6.3.4 The extinction

The determination of the extinction is an intricate problem. The classical method of comparing the observed colours with those of standard stars of similar properties does not lead to any conclusive result, given the slight variability of the star and the photometric (and spectral type) uncertainties. For normal stars, the UV part of the SED can be used to estimate this parameter, but in the case of HD 163296 the ultraviolet spectrum is variable and has contributions both from the photosphere and the accretion shock that are difficult to quantify. The extinction seems to be mostly circumstellar, therefore the exact value of the constant $R_{\rm V}$ is not known. The observations available do not allow us to disentangle completely this problem.

The strategy followed to assign a value of E(B–V) to this star has four steps: 1) introduce extinctions from E(B–V)=0.0 to 0.2 to the photospheric model, 2) normalize the reddened model photosphere to the flux at V, 3) de-redden the normalized model and estimate the integrated stellar flux, F_*; note that F_* is the flux that would be observed in the complete absence of extinction. Obviously, different extinctions imply different values of F_*. A value of $R_{\rm V}=3.1$ has been used.

The fourth step is based on the following argument: since the stellar luminosity $L_*/L_\odot$ is known through the distance-independent method outlined in section 6.3.1,

an estimation of the distance, d, can be obtained simply from the expression $L_* = 4\pi d^2 F_*$, where it is assumed that the whole star is visible, i.e. and no part of the stellar flux is completely blocked by the disc of other circumstellar material (see a complete discussion of this issue in Montesinos et al. [2009]). The value E(B–V)=+0.15 allows us to recover a distance of 128 pc, which matches the Hipparcos distance to within the uncertainties, therefore it has been adopted as the optimum extinction for consistency with the whole set of parameters. We would like to point out that that value is a simple parameterization of a very complex problem and that a deeper study, outside the scope of this chapter, would be needed to study all its peculiarities.

In Fig. 6.3 the photospheric model reddened with E(B–V)=+0.15 has been plotted. It goes through the two ultraviolet spectra but falls below both of them at wavelengths shorter than $\sim$ 1260 Å, and it also underestimates the flux at U. Note that the model is purely *photospheric*, therefore the excess fluxes inferred from the observed data when compared with the model might be due to emission from the accretion shock, i.e. with a non-photospheric origin. The observed SED seems to depart from the photospheric SED at around $\sim$ 1 μm, where the contribution from the disc starts to become noticeable.

6.3.5 Observational constraints

In addition to the new Herschel data I have further constrained my disc models using SMA interferometric observations of the J=3-2 transition in ^{12}CO and PBI interferometry of the ^{12}CO 2-1 and ^{13}CO 1-0 transitions [Isella et al., 2007], an upper limit for the S(1) transition in H_2 obtained by VLT/VISIR [Martin-Zaïdi et al., 2010], the ISO-SWS spectrum in the infrared, and a wealth of photometric data, including SCUBA photometry in the sub-mm [Sandell et al., 2011]. See Fig. 6.4 for a full list of the photometry sources.

There is a wealth of observational data available for HD 163296 which constrains to varying extents my choice of model parameters. As well as fitting to the data mentioned in the previous paragraph, I have taken care not to contradict current understanding of the disc geometry. There is at present some uncertainty regarding the radial extent of the disc. Scattered light imaging indicates an outer edge for the dusty disc of $\sim$ 540 AU, consistent with that derived for the gas disc from millimetre CO emission by Isella et al. [2007]. However, the resolved mm continuum emission seems to indicate a smaller outer disc radius $\sim$ 200 AU [Isella et al., 2007]. Hughes

Table 6.5: Fixed disc model parameters.

Quantity	Symbol	Value
stellar mass	$M_\star$	$2.47\,M_\odot$
effective temperature	$T_{\rm eff}$	9250 K
stellar luminosity	$L_\star$	$37.7\,L_\odot$
inner disc radius	$R_{\rm in}$	0.45 AU
dust material mass density	$\rho_{\rm gr}$	$3.36\,{\rm g\,cm^{-3}}$
strength of incident ISM UV	$\chi^{\rm ISM}$	1
cosmic ray H_2 ionisation rate	$\zeta_{\rm CR}$	$1.7\times10^{-17}\ {\rm s^{-1}}$
turbulent Doppler width	$v_{\rm turb}$	$0.15\,{\rm km\,s^{-1}}$
α viscosity parameter	α	0
disc inclination	i	50°
distance	d	118.6 pc

et al. [2008b] propose that the millimetre continuum and CO 3-2 emission can be fit simultaneously by a disc with an exponentially-tapered outer edge. For the purposes of my modelling, I adopt the surface density profile derived by Hughes et al. [2008b] for this object, and attempt to fit simultaneously the remaining observational data (SED, line fluxes, CO line profiles) by varying the remaining disc parameters. As an additional test, I compute a model with a power-law density profile, varying in addition the column density power index to fit the same data (SED, line fluxes, CO line profiles). For the purposes of this power-law model the disc outer edge is fixed at the scattered light radius of 540 AU. These adopted disc outer radii are consistent with our far-infrared photometry measurements, in which the disc is unresolved, corresponding to the emission at these wavelengths being dominated by the inner $\sim$200–300 AU of the disc.

The disc is also resolved at the inner edge, and while there is some uncertainty regarding the precise structure in this region [Renard et al., 2010, Benisty et al., 2010, Eisner et al., 2009, Tannirkulam et al., 2008b], I adopt the median value of 0.45AU for the inner disc radius. The disc is assumed to have constant flaring with radius, i.e. the assumed inner rim structure does not cause shadowing. The reference scale heights referred to in my results (see Table 6.6) are defined at the inner rim, i.e. $R = 0.45$ AU. The disc inclination is fairly well-constrained by imaging at various wavelengths [Benisty et al., 2010, Wassell et al., 2006, Isella et al., 2007, Tannirkulam et al., 2008a, Grady et al., 2000], and is fixed at 50° throughout the modelling in this paper. See Table 6.5 for a full list of the parameters which are fixed during the model-

fitting process.

While I have not used the spatial CO emission maps as a constraint for my modelling efforts, I do use the extracted line profiles for the three CO lines [Isella et al., 2007] as a constraint for the radial origin of the emission. The interferometry allows one to isolate the emission from the disc, eliminating contamination from cloud material. The bulk of the modelling uses a surface density profile derived from fitting to the spatial CO 3-2 emission [Hughes et al., 2008b].

6.4 Modelling

The disc modelling was carried out using the radiation thermo-chemical disc code ProDiMo [Woitke et al., 2009a, Kamp et al., 2010]. The code solves in turn the radiative transfer problem, chemical network, and gas heating and cooling balance. Finally, the level populations are calculated, followed by line transfer calculations to give the predicted line emission.

The frequency-dependent 2D radiative transfer solver calculates the dust temperature structure and internal continuous radiation field for a given disc and stellar spectrum. For the purposes of this chapter it was used to determine an SED-fitting dust model for HD 163296, by varying the total dust mass, grain size parameters and the spatial distribution of dust in the disc, including dust settling as a function of grain size (see Section 6.5.1).

Once the dust temperature structure $T_{\rm dust}(r,z)$ and internal radiation field $J_\nu(r,z)$ have been computed, ProDiMo solves the chemical network assuming kinetic equilibrium (such that the net concentration of each species does not change over time), and the gas energy balance. This gives the chemical composition of the disc, the gas temperature $T_{\rm gas}(r,z)$ and the gas emission lines, and depends on the gas-to-dust ratio and PAH abundance. The chemical network includes 973 reactions between 76 gas phase and solid ice species composed of 10 elements [Woodall et al., 2007, Schöier et al., 2005b]. There is a detailed treatment of UV-photoreactions [see Kamp et al., 2010], as well as H_2 formation on grain surfaces, vibrationally excited $H_2^\star$ chemistry, and ice formation (adsorption, thermal desorption, photo-desorption, and cosmic-ray desorption) for a limited number of ice species [see Woitke et al., 2009a, for details].

The level populations of the various atoms, molecules and ions are calculated using an escape probability method, and used to solve the line transfer for selected spectral

lines, in this case those of CO [Flower, 2001, Jankowski and Szalewicz, 2005, Wernli et al., 2006, Yang et al., 2010], H_2O [Barber et al., 2006, Dubernet and Grosjean, 2002, Faure et al., 2007, Green et al., 1993, Tennyson et al., 2001],OI [Abrahamsson et al., 2007, Bell et al., 1998, Chambaud et al., 1980, Jaquet et al., 1992, Launay and Roueff, 1977] and CII [Flower and Launay, 1977, Launay and Roueff, 1977, Wilson and Bell, 2002]. See Woitke et al. [2011] for a description of the line transfer calculations, as well as recent improvements to the chemistry and gas heating/cooling balance in PRODIMO.

6.4.1 Input spectrum

The stellar input spectrum used for the modelling is a composite of the available observed UV data with a model photosphere spectrum in the wavelength range for which detailed spectral data are not available. I have accounted for the observed ultraviolet variability of this object (see Section. 6.3) by running two sets of disc models with different UV input spectra, namely, one representing the "low UV" state and the other a "high UV" state, as described in Section 6.3.2. These were provided by the FUSE+STIS and the IUE average spectra, respectively. At the upper wavelength boundary I switch in each case to the GAIA PHOENIX model photosphere computed with $T_{\rm eff}$ = 9250 K, $\log g_*$ = 4.07 and [Fe/H]=+0.20. The observations were de-reddened using the Fitzpatrick parameterization (Fitzpatrick, 1999) with E(B–V)=+0.15 and $R_{\rm V} = 3.1$.

The UV spectrum is of central importance to the gas modelling, both in the chemical network and in the gas heating/cooling balance. This requires UV input for wavelengths of 912 Å and above (the wavelength at which atomic hydrogen is ionised). The FUSE spectrum in this case only extends down to 970 Å, and the IUE spectrum down to 1150 Å. In order to give a full spectrum for modelling purposes, the "high UV" input is extended down to 970 Å by scaling the STIS+FUSE (low UV) spectrum accordingly. In both cases a power-law fit to the data is employed for the remaining shortfall. The total photon particle fluxes are 60% greater for the high UV input spectrum than for the low UV state.

6.4.2 Fitting procedure

I have utilised a Monte-Carlo evolutionary method, varying the 11 parameters listed in Table 6.6. Deviations between model predictions and observations were measured using the same logarithmic χ^2 parameter as defined in equation 5.1. This was applied separately to the observed photometry points, all λ-points in the observed ISO-SWS spectrum, and the available gas line observations (see Section 6.3.5). In the case of the line observations the models were fitted to the observed fluxes, and the line widths in the case of the CO sub-mm observations, for which profiles were available. The upper limits were not used as a fitting constraint, but were checked against the predicted best-fit model fluxes for any contradictions.

The application of eqn. 5.1 to the three sets of observations results in $\chi^2_{\rm phot}$, $\chi^2_{\rm ISO}$ and $\chi^2_{\rm line}$ respectively, and the total quality of the model fit is then calculated as

$$\chi^2 = w^{\rm phot}\chi^2_{\rm phot} + w^{\rm ISO}\chi^2_{\rm ISO} + w^{\rm line}\chi^2_{\rm line} \tag{6.1}$$

with weights $w^{\rm phot} = 0.15$, $w^{\rm ISO} = 0.3$ and $w^{\rm line} = 0.55$.

The χ^2 value was then minimised by applying a (1,11)–evolutionary strategy with automated step-size control [Rechenberg, 2000]. The strategy uses 1 parent producing 11 children with slighly modified parameters, the best of which will become the parent of the next generation. The step-size δ is treated as an additional parameter which is passed-on to the children.

It should be noted that the best-fit parameters depend in general on the weighting scheme employed for the three groups of observations; in practice it was found that weighting slightly in favour of the line emission and ISO-SWS observations at the expense of the photometry gave the best fit overall. I also note the possibility that the converged parameter values correspond to a local χ^2 minimum, and not a single global minimum, and do not claim a unique fit to the observations. Indeed, it is clear from my modelling efforts that there exist many degeneracies between the various parameters. However, each of the models discussed in the following sections are the result of several hundred generations of χ^2-minimisation.

6.4.3 Dust properties

The rich solid-state spectrum of HD 163296 was observed by van den Ancker et al. [2000], using the ISO-SWS and ISO-LWS spectrometers. The study found the dust in

this object to consist of amorphous silicates, iron oxide, water ice and a small fraction of crystalline silicates, with the presence of large millimetre-sized grains indicated by the continuum temperature.

I assume homogeneous and spherical dust grains (Mie theory), with a power-law size-distribution defined by a minimum radius $a_{\rm min}$, maximum radius $a_{\rm max}$, and power-law index p. The grain composition is assumed to be constant throughout the disc, and I adopt the dust species mixture determined by Bouwman et al. [2000] for this object, averaging their fractional species abundances over the disc (see Table 6.7). All grains have the same species composition regardless of their size, and the grain composition is not treated consistently with the physics and chemistry of grains. For instance, the assumed grain water ice fraction is constant throughout the disc, independent of the water ice abundances calculated in the solution of the chemical network. For the dust material mass density, I take the average value for this mix of $3.36\,{\rm g\,cm^{-3}}$. Optical constants for the various dust species were taken from measurements made by the studies listed in Table 6.7.

Bouwman et al. [2000] carried out a detailed study of this object, fitting to spectral data over a large wavelength range. I note however that the dust opacity law represents a potentially large source of uncertainty when deriving the disc parameters. For instance, the two olivine species $FeMgSiO_4$ and Mg_2SiO_4, whilst having broadly similar spectra in the wavelength range observable by ISO-SWS, have a factor > 30 difference in absorption opacity at ~ 1 micron. This will inevitably affect the derived disc parameters, although the difference in opacities at millimetre wavelengths is negligible. The models referred to in this study have extinction opacities in the range $(10.4 - 12.8)\ {\rm cm^2 g^{-1}}$(dust) at 1mm.

6.4.4 Gas/dust ratio

The models considered have constant dust properties with radius. However, in general the models do allow for differential dust grain scale heights as a function of grain size, to represent the major effects of dust settling. This leads to a local gas/dust ratio which varies with height in the disc, yet at any given radius the ratio of the vertical gas and dust total column densities is constant, and equal to the global gas/dust ratio. The degree of dust settling is determined by a simple parameterisation (see Section 6.5.1), and models in which no dust settling is present are referred to as “fully mixed”.

Table 6.6: Model parameters for four well-fitting disc models. The first three columns refer to models with exponentially-tapered density profiles, while model 4 is a simple power law. Models 1, 3 and 4 are for a "low UV" input spectrum while model 2 is for a "high UV" flux. Finally, models 1, 2, and 4 allow dust grains to settle towards the midplane while model 3 is fully mixed. Model 3 represents my overall "preferred" model, which is later discussed in detail, and is marked by an asterisk.

		(1)	(2)	(3)*	(4)
Quantity	Symbol	"low UV"	"high UV"	Fully mixed	Power-law
disc mass	$M_{\rm disc}$	$2.2\times10^{-2}\,M_\odot$	$2.0\times10^{-2}\,M_\odot$	$7.1\times10^{-2}\,M_\odot$	$1.1\times10^{-2}\,M_\odot$
column density power index	ϵ	n/a	n/a	n/a	0.085
reference scale height	H_0	0.019 AU	0.019 AU	0.019 AU	0.027 AU
flaring power	β	1.068	1.066	1.066	1.019
gas-to-dust mass ratio	ρ/ρ_d	21.8	20.5	101.1	9.1
minimum dust particle radius	$a_{\rm min}$	$5.95\times10^{-3}\,\mu$m	$1.25\times10^{-3}\,\mu$m	$9.63\times10^{-3}\,\mu$m	$1.24\times10^{-2}\,\mu$m
maximum dust particle radius	$a_{\rm max}$	$1134\,\mu$m	$1405\,\mu$m	$2041\,\mu$m	$1015\,\mu$m
dust size dist. power index	p	3.61	3.57	3.68	3.75
dust settling parameter	s	0.57	0.39	0 (fixed)	0.56
minimum dust settling radius	$a_{\rm set}$	$1.09\,\mu$m	$0.44\,\mu$m	n/a	0.81
PAH abundance relative to ISM	$f_{\rm PAH}$	4.3×10^{-2}	3.5×10^{-2}	6.8×10^{-3}	2.2×10^{-2}
fit to observed photometry	$\chi_{\rm PHOT}$	1.723	2.061	1.323	1.279
fit to ISO-SWS spectrum	$\chi_{\rm ISO}$	1.326	1.378	1.780	0.827
fit to observed line data	$\chi_{\rm LINE}$	0.661	0.741	0.742	0.607

6.5 Results

Table 6.6 gives the derived parameter values for four runs of the evolutionary scheme outlined in the previous section. The first three columns refer to models with a fixed exponentially-tapered density profile. The fourth column refers to a model with power-law density profile, $\Sigma \propto R^{-\epsilon}$, in which the outer radius is fixed at 540 AU but the power index, ϵ, is allowed to vary.

The surface density profile in the models with an exponential outer edge (columns 1-3) takes the form

$$\Sigma(R) \propto R^{-\gamma}\ \exp\left[-\left(\frac{R}{R_0}\right)^{2-\gamma}\right], \tag{6.2}$$

where γ is analagous to the power law index, and R_0 is the scale length over which the disc surface density tapers exponentially. I adopt the previously derived values of $\gamma = 0.9$ and $R_0 = 125$ AU [Hughes et al., 2008b]. For the purposes of my modelling, the disc chemistry etc. was computed out to 850 AU, at which point the column density is negligible.

The first, "low UV" column uses the FUSE+STIS UV spectrum as input for the modelling, and the second "high UV" column uses the average IUE spectrum, as described in Section 6.4.1. Both runs produce settled discs, with variable scale heights for dust grains of different sizes. The third column in Table 6.6 gives the results

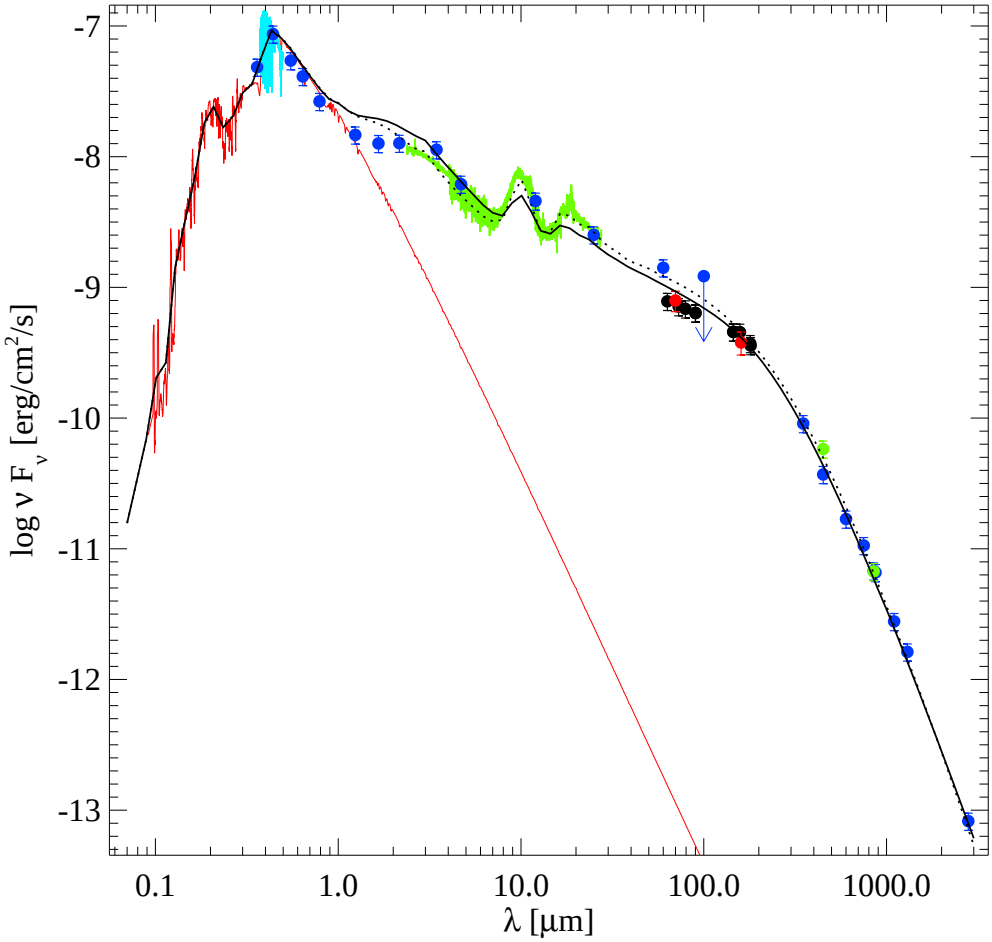

Figure 6.4: Spectral energy distribution for the best-fit fully mixed disc model ("preferred" model), obtained from a simultaneous fit to the observed SED, ISO-SWS spectrum and line emission from HD 163296 (solid black line). Black dotted line indicates the SED for the model with power-law density profile, which is unable to fit the mm continuum image for HD 163296. Blue circles indicate (with increasing wavelength) simultaneous UBVRIJHK photometry [Eiroa et al., 2001, Oudmaijer et al., 2001], LM photometry [de Winter et al., 2001], IRAS photometry (12-100 mic), sub-mm photometry [Mannings, 1994], and millimetre photometry [Isella et al., 2007]. Also marked are PACS photometric observations (red circles), PACS continua derived from the spectroscopic observations (black circles), SCUBA photometry (green circles) [Sandell et al., 2011], scaled VLT/UVES spectrum (blue line, Martin-Zaidi, in preparation) and the ISO-SWS spectrum (green line). The red line shows the stellar+UV input spectrum. Downwards arrow denotes upper limit. All fluxes were corrected for interstellar reddening using the Fitzpatrick parameterisation [Fitzpatrick, 1999] with $R_V = 3.1$ and E(B–V)= 0.15.

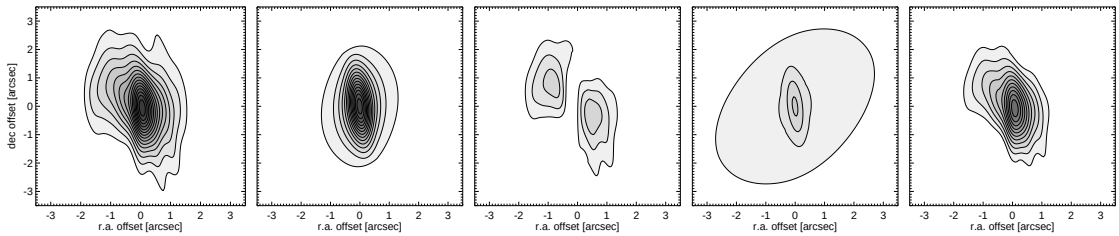

Figure 6.5: 1.3mm continuum emission maps for HD 163296. From left: observed map; emission map for preferred model (column 3 in Table 6.6); residuals for preferred model; emission map for power-law model (column 4 in Table 6.6); residuals for power-law model. Residuals computed by subtracting the model intensity from the observed intensity. Contours spaced at 12 mJy intervals, corresponding to [3,6,9,12,15,18,21,24,27,30,33,36,39,42,45]$\times\sigma$.

for a run with well-mixed dust grains, i.e. no settling is introduced. This run uses the FUSE+STIS (low UV) spectrum, as does the run with power-law surface density referred to in column 4.

None of the models described in Table 6.6 represent a perfect fit to all the available data for HD 163296, but in all cases the models are able to fit almost all the observations. Considering the large number of data used for the modelling, and the range of parameters covered by the well-fitting models, is is clear that there is some degree of parameter degeneracy present.

6.5.1 Continuum emission and spectral energy distribution

The SED for the best-fit fully mixed disc model (column 3 in Table 6.6) is shown in Fig. 6.4. With the constraints outlined in previous sections, my aim was to fit the observed SED with a simple dust model, i.e. a continuous disc with constant flaring, and dust species composition constant throughout the disc. All of the models described in Table 6.6 require the presence of mm-sized grains in order to fit the observed SED. It was not possible to fit both the 10 micron silicate feature and the millimetre tail with a well-mixed disc. This can be seen in Table 6.6, where the fully mixed model gives a worse fit to the ISO-SWS spectrum than for the models in which dust settling is present. Fig. 6.4 shows that the best-fit fully mixed model gives a smaller than observed silicate emission feature. Sitko et al. [2008] observe a spectral variability of $\sim$ 10% in the wavelength range covered by the ISO-SWS data, and while I am unable to fit the observations to within this range with even a settled model (simultaneously

Table 6.7: Dust grain composition.

Dust Species	Mass Fraction	Optical constant ref.
Amorphous $FeMgSiO_4$	0.745	Dorschner et al. [1995]
Amorphous Carbon	0.15	Jager et al. [1998]
Crystalline Mg_2SiO_4	0.035	Servoin and Piriou [1973]
Water Ice	0.035	Warren and Brandt [2008]
Iron Oxide	0.02	Henning et al. [1995]
Iron	0.015	Posch et al. [2003]

with the overall SED and line data), the fit is considerably better than is possible with a well-mixed disc. This result is similar to that found for IM Lupi by Pinte et al. [2008], in which a settled disc was needed to fit the 10 μm silicate feature and SED millimetre tail simultaneously.

On the other hand, the constraint of fitting to the ISO-SWS spectrum leads to models which produce too much emission in the near-infrared (J,H and K bands), giving an overall worse fit to the observed photometry. This effect is less pronounced in the best-fit fully mixed model (column 3 c.f. columns 1&2 in Table 6.6). The flux overprediction in the settled models is likely mainly due to the smaller average grain size in the strongly illuminated disc surface layer. The condition of radiative equilibrium between grains means that this gives a higher average grain temperature at the disc surface, and the re-emitted light peaks at shorter wavelength than for the fully mixed models (in the near-IR as opposed to the mid-IR). This flux overprediction is still present to a smaller extent in the fully mixed model (see Fig. 6.4). This could be a consequence of my fixing the disc inner radius for modelling purposes, and a better fit in the near-IR would be possible if I had allowed the inner radius to vary. It is also probable that the structure of the inner rim is more complex than allowed by this parameterised model, with evidence for puffing-up of material, which would certainly affect the emission at these wavelengths. There is also significant variability observed for this object in this wavelength region [de Winter et al., 2001, Sitko et al., 2008].

Dust settling enhances the silicate emission feature for an optically thick disc since it removes the large grains from the surface layers, and places them at smaller heights in the disc where they cannot be observed at mid-infrared wavelengths. The flat blackbody opacity of these larger grains is overwhelmed by the characteristic spectrally-varying opacity of smaller micron-size grains which remain at lower optical depth, dominating the observed emission.

In cases such as this where a simple parameterised disc structure is assumed, ProDiMo implements a simple recipe to account for the major effects of vertical dust settling. It is assumed that the dust grains are distributed vertically with a scale height which decreases for large dust particles:

$$H'(a,r) = H(r) \cdot \max\{1, a/a_s\}^{-s/2} \tag{6.3}$$

where $H(r)$ is the gas scale height, and s and a_s are two free parameters (see Woitke et al. [2010] for details).

Introducing two additional parameters to the modelling inevitably improves the fit to the observed data, and indeed the combined fit to the photometry, ISO-SWS spectrum and line emission does improve overall as dust settling is introduced. The fact remains, however, that it is possible to obtain a good fit to almost all the available data with a well-mixed disc, with a gas/dust ratio almost equal to the canonical value of 100, and so I adopt this model, described in column 3 of Table 6.6, as my "preferred" model. However, the inability of a well-mixed disc such as this to fit the observed emission in the mid-infrared means that there remains compelling evidence for a disc exhibiting dust-settling, able to fit the line emission with a depleted gas/dust ratio (see column 1 in Table 6.6). The effect of dust settling on the line emission is further explored in Section 6.5.2.

The model with power-law density profile (column 4 in Table 6.6) gives the best overall fit to the SED, ISO-SWS spectrum and line emission (see Fig. 6.4), with quite different disc parameters to the three models with exponential outer edges (columns 1-3). The disc requires a very flat density profile, $\epsilon \sim 0.085$, in order to fit these observations (not including spatial data). The predicted millimetre continuum emission from this model is plotted with the observed maps in Fig. 6.5. It is clear that the flat density profile leads to an emission deficit in the inner disc in comparison to observations, and so this cannot be considered to be a good model for the disc of HD 163296. A better power-law model could be found by using the maps as a further constraint for the modelling, but that is beyond the scope of this work. The fully mixed "preferred" model gives a better match to the observed millimetre emission, as should be expected since its density profile is derived from fitting to this data [Hughes et al., 2008b]. The factors driving the power-law model to such a flat density profile will be discussed in Section 6.5.2.

The power-law density profile model is, however, able to fit the non-spatially-

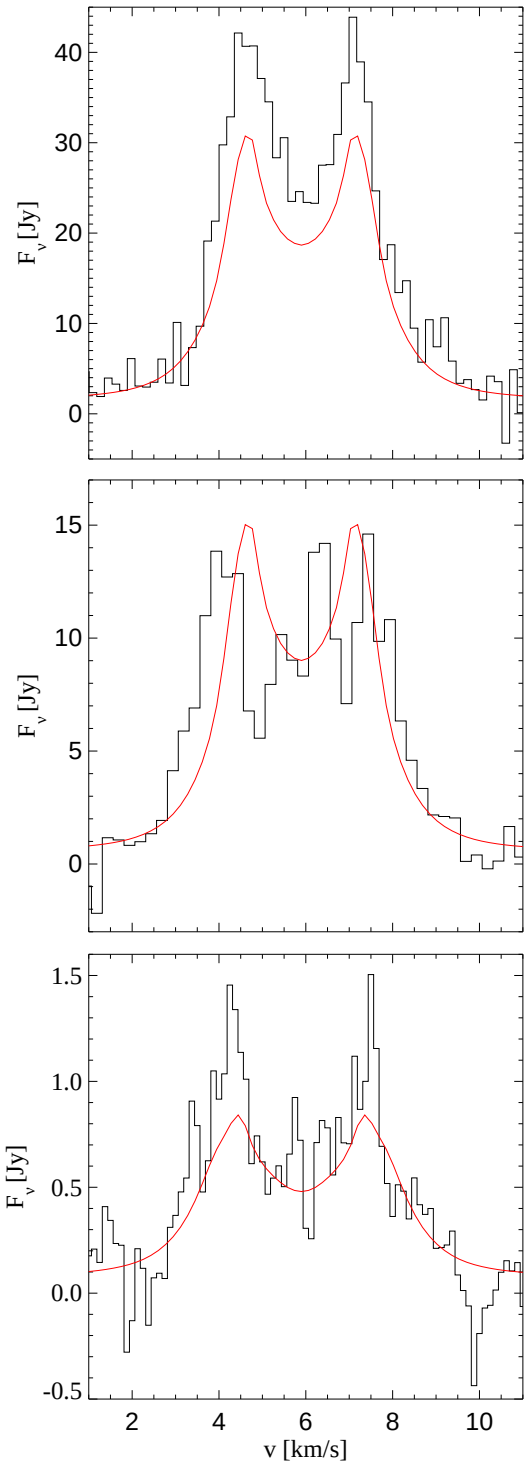

Figure 6.6: Plotted in black are the line profiles observed by Isella et al. [2007] for the ^{12}CO J=3-2 (upper panel), ^{12}CO J=2-1 (middle panel) and ^{13}CO J=1-0 (lower panel) transitions, with the corresponding profiles from the preferred disc model in red. This refers to a single simultaneous fit to the observed continuum and line data (column 3 in Table 6.6). Observed profiles are obtained by integrating over the whole disc.

resolved data with a smaller flaring index (~ 1.02) than the exponentially-tapered discs (~ 1.07), more in keeping with the observational evidence for a disc that is not strongly flaring [Meeus et al., 2001, Doucet et al., 2006, Wisniewski et al., 2008]. Meeus et al. [2001] classify HD 163296 as a group II object, in which the inner disc shadows the outer disc, as opposed to group I objects which have a flared geometry. Meijer et al. [2008] find HD 163296 to lie on the transition between flared and non-flared geometry, i.e. a flaring index close to 1. It is clear that my "preferred" model is unable to account for every observed property of the disc of HD 163296, and it is probable that a more complex model - with non-constant flaring and variable dust properties with radius - would be required to simultaneously fit the full set of observational data available for this object.

The models described in Table 6.6 have disc dust masses in the range $(7-12)\times 10^{-4}M_{\odot}$, which is within the range of masses $(5-17)\times 10^{-4}M_{\odot}$ found in the literature for HD 163296. This small spread in dust mass from my fitting efforts is unsurprising given the fixed disc size and constant grain composition.

6.5.2 Gas properties

The predicted line fluxes for the various models are given in Table 6.8. I have ignored the [CII] 158 μm result during the model-fitting process, due to systematic uncertainties arising from strong emission at the offset positions.

The observed line profiles for the ^{12}CO J=3-2, ^{12}CO J=2-1 and ^{13}CO J=1-0 transitions [Isella et al., 2007] are plotted with the preferred model profiles in Fig. 6.6. The observed profiles are double-peaked, consistent with a disc in Keplerian rotation. The CO 3-2 line is observed to be brighter than predicted by the model. This behaviour is repeated across the three exponentially-tapered models, but is less pronounced in the power-law model, whose flat surface density profile gives a larger CO 3-2 flux. Discs with flatter density profiles allow stellar radiation to penetrate deeper into the inner disc, resulting in a slight increase in temperature throughout the disc, including its outer regions. This leads to brighter CO 3-2 lines since this transition is optically thick in all of my models, and is largely dependent on the disc outer radius (which is fixed) and the outer disc temperature at intermediate height (see Fig. 6.8). The CO 2-1 line also follows this behaviour, with the line flux ratio in the models staying roughly constant at a value of CO 3-2/1-0 ~ 3, as expected for lines formed under optically thick LTE conditions [Kamp et al., 2010]. This is slightly lower than the observed ratio of

Table 6.8: Integrated line fluxes for the transitions observed by PACS, and additional CO and H_2 lines, as predicted by the models listed in Table 6.6. Observed fluxes for comparison. Fluxes in [10^{-18} W/m^2]. Errors are a quadratic sum of the calibration error (20% for the interferometric CO observations and 30% for the PACS observations) and the RMS continuum noise.

Species	λ [μm]	ν [GHz]	"low UV" model	"high UV" model	Fully mixed model	Power-law	Observed Flux
OI	63.18	4745.05	200.6	222.0	191.4	170.3	193.1 (58.2)
OI	145.52	2060.15	6.29	7.33	5.39	4.59	< 8.5
CII	157.74	1900.55	8.32	8.40	11.2	9.98	–
p-H_2O $3_{22} \rightarrow 2_{11}$	89.99	3331.40	1.22	1.68	1.20	0.353	< 9.4
o-H_2O $2_{12} \rightarrow 1_{01}$	179.52	1669.97	4.40	4.19	2.43	3.94	< 14.5
o-H_2O $2_{21} \rightarrow 2_{12}$	180.49	1661.64	0.847	0.993	0.618	0.243	< 16.2
o-H_2O $4_{32} \rightarrow 3_{12}$	78.74	3810.01	2.33	2.94	2.20	0.840	< 15.0
o-H_2 S(1)	17.03	17603.78	1.15	1.59	1.15	0.572	< 28
OH	79.11	3792.19	4.59	6.31	5.40	2.71	< 17.0
OH	79.18	3788.84	4.78	6.54	5.59	2.82	< 17.0
CO J=36-35	72.85	4115.20	0.335	0.489	0.423	0.132	< 11.6
CO J=33-32	79.36	3777.63	0.497	0.704	0.578	0.197	< 22.8
CO J=29-28	90.16	3325.12	0.763	1.03	0.732	0.311	< 11.1
CO J=18-17	144.78	2070.68	1.91	2.31	1.49	0.851	< 13.1
CO J=3-2	866.96	345.80	1.26	1.27	1.22	1.49	1.65 (0.39)
CO J=2-1	1300.40	230.54	0.401	0.401	0.397	0.464	0.379 (0.118)
^{13}CO J=1-0	2720.41	110.20	0.0122	0.0115	0.0120	0.0127	0.0124 (0.007)

CO 3-2/2-1 = 4.3. Recent observations of this object give a peak intensity of 25 Jy for the 3-2 line [Hughes et al., 2011][5], compared with 43 Jy in the Isella et al. [2007] data and the 30 Jy predicted by my preferred model. The predicted flux is within the calibration error margin for both observations, but fitting to the lower value would in general tend to lead to power-law models with steeper density profiles, in contrast to the flat power-law profile I obtain from fitting to the brighter observation. Another factor driving the power-law models to flat density profiles is the overprediction in near-IR continuum emission by my models. The inner radius is fixed in accordance with high resolution imaging, and so the power-law models tend to reduce their near-IR emission by removing material from the inner disc, giving a better fit to the photometry.

PAHs are one of the main sources of gas heating in the disc, as UV photons cause them to emit excited electrons via the photoelectric effect, which thermalise in the gas. For the purposes of the modelling I consider a typical size of PAH molecule (circumcoronene, $N_{\rm C} = 54$ carbon atoms and $N_{\rm H} = 18$ hydrogen atoms) and include PAH^-, PAH, PAH^+, PAH^{2+} and PAH^{3+} as additional species in the chemical network (see Woitke et al. [2010] for further details). The fractional PAH abundance, $f_{\rm PAH}$, is defined relative to the standard ISM particle abundance with respect to hydrogen nuclei, $X^{\rm ISM}_{\rm PAH} = 3 \times 10^{-7}$ [Tielens, 2008], so that the PAH abundance, ϵ(PAH) = $f_{\rm PAH}\, X^{\rm ISM}_{\rm PAH}\, \frac{50}{N_{\rm C}}$. Small $f_{\rm PAH}$ values (0.007-0.04 relative to ISM abundances) are required in my models in order to fit the observed line data. This is consistent with the findings of Geers et al. [2006], who require PAH abundances $f_{\rm PAH} < 0.1$ in order to fit the observed PAH emission from Herbig discs. PAH emission was not observed in HD 163296 by Acke et al. [2010], and we have used the Monte Carlo radiative transfer code MCFOST [Pinte et al., 2006] to check that our results are consistent with this non-detection. A disc model with parameters and PAH abundance identical to the preferred model gives an infrared spectrum in which no PAH emission is seen. This is due in part to the low flaring in the disc, $\beta = 1.066$, and the large fraction of small dust grains in the disc, with significant opacity in the optical-UV range over which PAH molecules absorb. This results in the PAHs being "hidden" from direct stellar illumination, absorbing a fraction $\sim 10^{-4}$ of the energy absorbed by the disc. In the preferred model 0.3% of the total carbon mass is tied up in PAH molecules.

The total hydrogen number density and gas temperature within the disc are plotted

[5]This CO 3-2 data also seems to indicate the presence of turbulence of order 0.3 km/s in the disc of HD 163296 [Hughes et al., 2011]. I have not yet explored the effect of this possible stronger turbulence on my results.

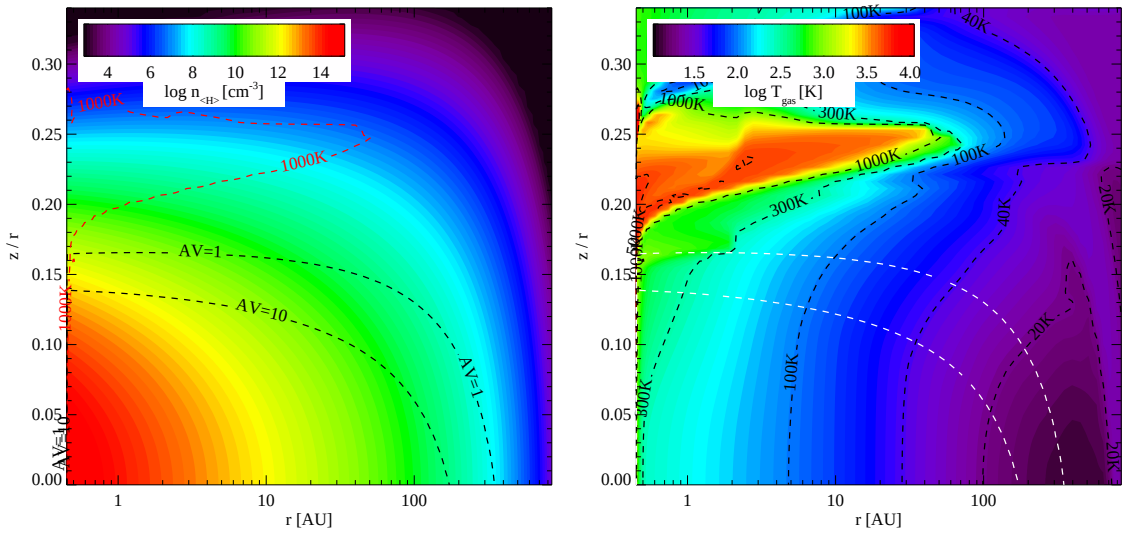

Figure 6.7: The total hydrogen number density (left panel) and gas temperature (right panel) are plotted for a vertical cross-section through the preferred disc model (column 3 in Table 6.6). Dashed lines indicate contours of gas temperature and visual extinction A_V, as marked.

in Fig. 6.7, and the spatial origin of the various emission lines is visualised in Fig. 6.8. These plots all refer to the "preferred" disc model, i.e. one in which no dust settling is present. The CO J=3-2 and [OI] 63 μm lines are optically thick throughout the disc, and cannot be used alone to trace the gas mass. Even the ^{13}CO line is optically thick throughout much of the disc, only becoming optically thin outside of $\sim$ 400 AU. Also, there is evidence that this line (and most others) can be affected by the degree of dust settling in the disc (see Section 6.5.2). The [CII] 157.74μm line is optically thin, but traces only the warm ionised gas in the disc surface. Clearly care must be taken when attempting to use individual emission lines as a tracer of gas mass. Note the contrast in disc radii at which line and continuum become optically thin in the case of CO 3-2, reflecting the conflicting derived radii for the gas and dust discs in HD 163296. The line optical depths in Fig. 6.8 were computed using an escape probability formalism, and do not take into account the effects of Keplerian shear in the disc.

As well as optical depth effects, disc gas mass estimates from CO emission alone can be affected by the extent of CO freeze-out on grain surfaces. ProDiMo calculates the grain adsorption and desorption as part of the solution of the chemical network, and the spatial abundances of gas-phase and ice CO in my best-fit model are plotted in Fig. 6.9. The total mass of gas-phase CO in the disc is 1.51 $\times$ 10^{-5}M$_\odot$, and the CO ice

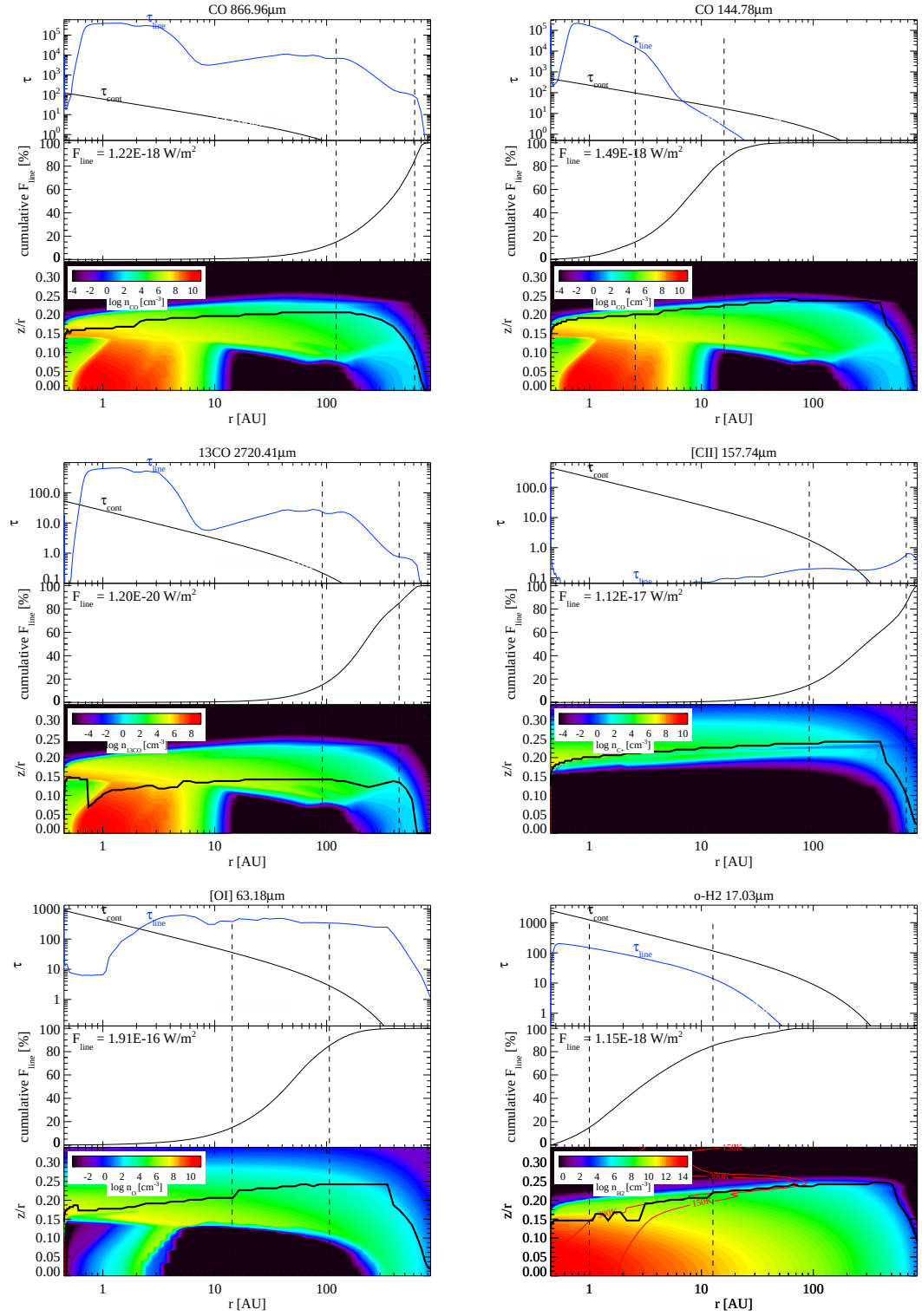

Figure 6.8: Spatial origin of the various gas emission lines in the preferred model (column 3 in Table 6.6). From top-left clockwise: CO J=3-2, CO J=18-17, [CII] 157.74μm, o-H_2 S(1) (with red T_g contours), [OI] 63.18μm, ^{13}CO J=1-0. In each panel, the upper plot shows the line optical depth as a function of radius (blue line) and the continuum optical depth at the corresponding wavelength (black line). The middle plot shows the cumulative contribution to the total line flux with increasing radius. The lower plot shows the gas species number density, and the black line marks the cells that contribute the most to the line flux in their vertical column. The two vertical dashed lines indicate 15% and 85% of the radially cumulative face-on line flux respectively, i.e. 70% of the line flux originates from within the two dashed lines.

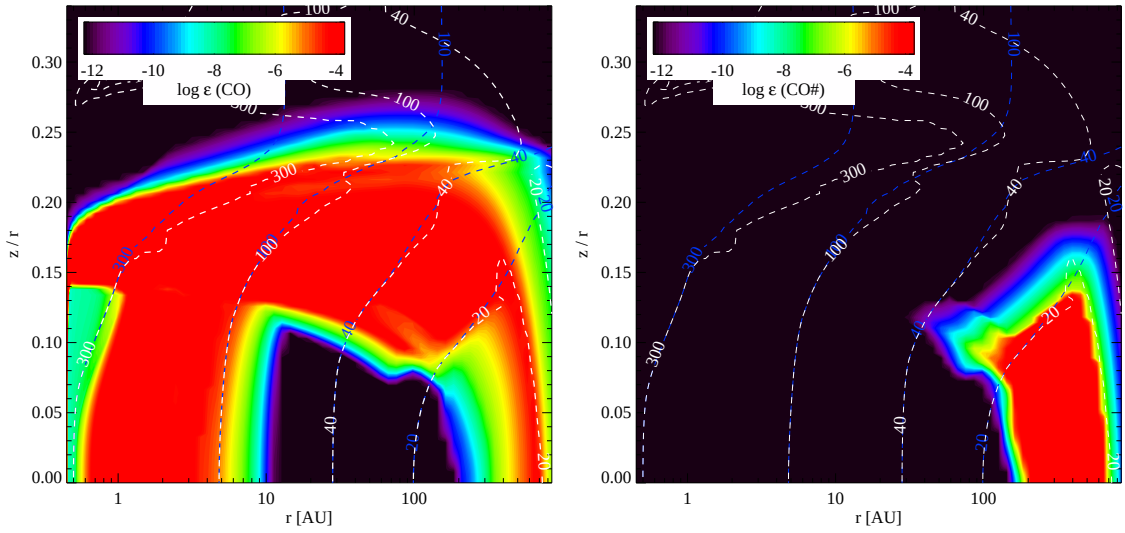

Figure 6.9: CO abundances in the preferred model (column 3 in Table 6.6). Left panel: gas-phase CO abundances. White and blue dashed lines plot the gas and dust temperature contours respectively. Right panel: CO ice abundance.

mass is $4.32 \times 10^{-5} M_{\odot}$. One would expect a smaller fraction of CO to be frozen out on grain surfaces in discs with flatter density profiles, due to weaker dust shielding in the inner disc leading to warmer temperatures throughout the disc, and less CO freeze-out.

The derived chemical abundances and gas properties in my preferred model have been checked by re-computing the chemistry using a time-dependant solver, and comparing the results to those obtained with the assumption of kinetic equilibrium. I assume molecular cloud initial abundances, and after running the solver for 4 Myr there is no major departure from the equilibrium chemistry. The biggest change in line flux is a reduction of 20% in the 180.4 μm water line, while the [OI] 63 μm line decreases by 4% and the CO lines by $< 1\%$. The assumption of a constant $^{13}CO/^{12}CO$ ratio is also valid since dust shielding dominates over CO self-shielding in the models, with negligible change to the results when CO self-shielding is swtiched off, suggesting that no fractionation effect would be present in this disc.

All of the disc models considered are passive discs, i.e. the viscous "α" heating parameter is set to zero. This is not strictly consistent with the presence of accreting gas in this object, since this implies some form of viscosity to transport angular momentum through the disc. However, viscous heating is likely to be unimportant in the case of Herbig Ae discs such as this, which are thought to be dominated by radiative heating by the central star [D'Alessio et al., 1998].

Table 6.9: Effects of UV variability. Comparison between the preferred model, and an identical model illuminated by an input spectrum typical of a "high UV" state for this object. Shown are total species masses, average overall CO temperature, average CO temperature for the warm gas regions in the inner disc, and line fluxes. $L_{\rm UV}$ refers to the energy emitted in the wavelength range 912-2500 Å.

	Best-fit model	Test model (high UV)
$L_{\rm UV}/L_\star$	0.097	0.155
$M_{\rm H}$	$2.67\times10^{-5}\mathrm{M}_\odot$	$2.82\times10^{-5}\mathrm{M}_\odot$
$M_{\rm C^+}$	$8.67\times10^{-8}\mathrm{M}_\odot$	$9.42\times10^{-8}\mathrm{M}_\odot$
$M_{\rm CO}$	$1.54\times10^{-5}\mathrm{M}_\odot$	$1.66\times10^{-5}\mathrm{M}_\odot$
$\langle T_{\rm CO}\rangle$	55.3 K	55.0 K
$\langle T_{\rm CO}\rangle\,(z/R>0.2,\ R<20\,\mathrm{AU})$	262.8 K	332.6 K
$F_{\rm [OI]\,63\,\mu m}$	$1.91\times10^{-16}\mathrm{W\,m^{-2}}$	$2.49\times10^{-16}\mathrm{W\,m^{-2}}$
$F_{\rm [CII]\,58\,\mu m}$	$1.12\times10^{-17}\mathrm{W\,m^{-2}}$	$1.41\times10^{-17}\mathrm{W\,m^{-2}}$
$F_{\rm CO\ 3-2}$	$1.22\times10^{-18}\mathrm{W\,m^{-2}}$	$1.31\times10^{-18}\mathrm{W\,m^{-2}}$
$F_{\rm CO\ 36-35}$	$4.23\times10^{-19}\mathrm{W\,m^{-2}}$	$6.22\times10^{-19}\mathrm{W\,m^{-2}}$

Effect of UV variability

I have investigated the effects of UV variability on the gas in the disc in two ways. Firstly, by computing a test model with parameters identical to my "preferred" model, but with the high UV state spectrum used as input. This isolates the effect of increasing the UV intensity on the line emission, since all other model parameters remain the same. The results of this test are summarised in Table 6.9. The second approach consists of a separate evolutionary run of models using the high UV state as input, and has been covered in Section 6.5. This method allows me to assess how the disc model parameters change in order to fit the same line data with an increased UV intensity (see Table 6.6). By examining firstly the physical effect of the UV on the gas in the disc, and secondly the effect of the UV on the model parameter fit, it is possible to estimate the degree of uncertainty introduced by UV variability in this object.

An increased UV strength affects the gas chemistry by promoting photochemical reactions, and the photodissociation of H_2 and CO. It also leads to increased desorption of ice species from grain surfaces in regions where the UV is able to penetrate. It also strongly affects the gas heating, via the photoelectric effect in dust grains and PAHs.

The "high UV" input spectrum represents a 60% increase in UV intensity over the low UV input. Table 6.9 summarises the effects of this increase on the gas in the preferred model. There is a slight overall increase in the disc gas temperature, and

an increase in the atomic hydrogen and C^+ masses, due to photoelectric effects and PAH heating, and increased photodissociation of gas molecules. The total gas-phase CO mass actually increases slightly, since the increased rate of photodissociation is balanced by an increase in the rate of ice desorption. The J=36-35 line in particular sees the biggest increase in flux, $\sim 50\%$. By considering only the gas in the warm layers of the inner disc, where the high J CO lines form, it can be seen that this increase in line flux is caused by a substantial increase in the gas temperature in this region. The [OI] 63 μm flux increases by $\sim 30\%$, roughly equal to the calibration uncertainty margin, and the low J CO lines increase by $\sim 5\%$. All non-detected lines stay within the observed upper limits. In summary, it would not be possible to distinguish between the high and low UV states from these disc observations, since all fluxes are within the observational error margins. The general influence of the UV intensity on the disc gas is discussed by Woitke et al. [2010], in the context of a large grid of models.

The derived parameters for the evolutionary run using the "high UV" spectrum as input are listed in Table 6.6. They are largely similar to those derived from the low UV run (columns 2 c.f. 1), as would be expected from the small fractional change in UV intensity. The slight decrease in gas mass and flaring will tend to counteract any increase in line emission. The PAH fractional abundance decreases slightly as might be expected. The main change lies in the grain size distribution, with a reduction in the minimum grain size. This makes it harder for the UV to penetrate the disc, balancing the increase in UV intensity. This also produces even more continuum emission in the near-IR, worsening the SED fit still further in comparison to the "low UV" model.

Effects of dust settling

The effect of dust settling on various line fluxes can be seen in Fig. 6.10. This shows the increase in line flux across the various transitions as smaller and smaller grains are allowed to settle towards the midplane. The models are otherwise identical to the preferred (fully mixed) model, but with a settling parameter of 0.5. The models run from strongly settled discs through to entirely well-mixed, i.e. identical to the preferred model. For the purposes of this exercise I have computed some extra line fluxes in addition to those observed in HD 163296, namely the ^{12}CO 6-5 and 1-0 transitions, the ^{13}CO 3-2 transition, and the o-H_2O 538.3μm transition.

Kamp et al. [2011] computed a large grid of disc models using ProDiMo, in tandem with Mcfost [Pinte et al., 2006] (see Chapter 4). This study noted a trend of increasing

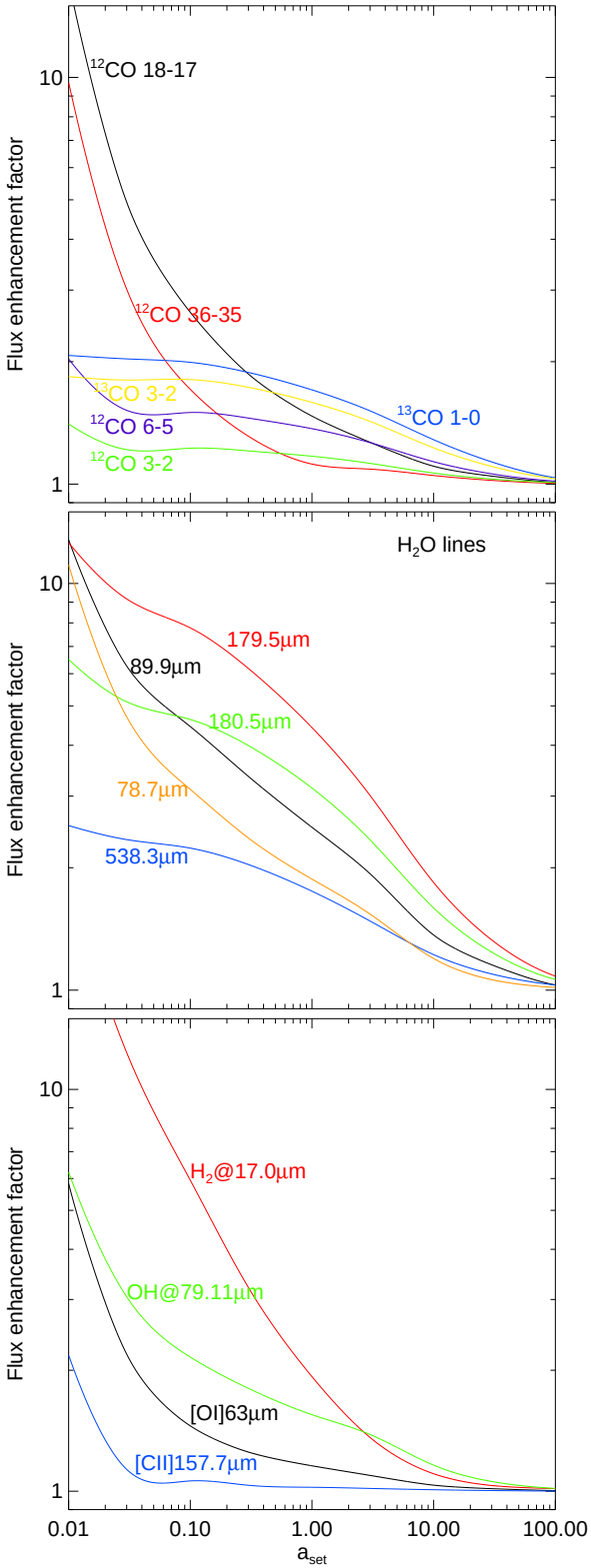

Figure 6.10: The fractional enhancement in line flux is plotted against the minimum grain size affected by dust settling, relative to the preferred (fully mixed) model ($a_s = a_{max}$). All models have a settling parameter of 0.5. Top panel: CO lines; Middle panel: water lines; Lower panel: [OI]63μm, [CII]158μm, OH 79.11 μm and H_2 S(1) lines.

disc dust temperature with settling, due to a combination of reduced emissivity at long wavelengths in the disc surface, and increased illumination of the dust as the stellar radiation is able to penetrate further into the disc. My models of HD 163296 follow this same behaviour, albeit with an accompanying increase in gas temperature. The effect of dust settling on the gas and dust temperature contours in my models is demonstrated in Fig. 6.11, where the chemical abundances of various chemical species are plotted. The chemical structure is seen to "follow" the settled dust grains towards the midplane, since the UV penetrates further into the disc, causing the characteristic layering of the various gas species to move closer to the midplane. This is despite the gas scale heights being identical in both models. In the settled models the warm gas in the disc resides at lower heights where the gas density is higher, leading to a general brightening of the emission lines. This seems to be a firm result for this object, with serious implications for the derivation of a precise disc gas mass from the emission lines.

The brightening of the line fluxes seems to be a general result for all the transitions considered. The exact behaviour of the various line fluxes with variable dust settling, and the extent to which they are affected, depends on the height and radial position in the disc from which they originate. This is well-illustrated by the CO lines in Fig. 6.10. As the largest grains begin to settle, the ^{13}CO 1-0 line is the first to show an increase in flux. This is due to an increase in thermal desorption of CO ice from grain surfaces in the outer disc midplane, which this line traces (see Fig. 6.8). This behaviour is echoed in the other ^{13}CO line, the J=3-2 transition. In contrast, the ^{12}CO 3-2 line, which is also formed in the outer disc, shows a smaller increase in flux. This is because this line is optically thick, and formed higher in the disc where it remains unaffected by the thermal desorption of ice in the midplane. The ^{12}CO 2-1 and 1-0 lines follow this same behaviour (not plotted). As smaller grains begin to settle, the ^{13}CO lines increase less rapidly than for the lines formed in the warm gas higher in the disc. This is most pronounced in the high J CO lines, which form in the inner disc where the temperature and density gradients are more extreme, and the lines more sensitive to the downwards shift in chemical structure. The ^{12}CO 6-5 line forms at intermediate distance in the disc, and this is reflected in the level of flux enhancement (Fig. 6.10; top panel).

The behaviour of the water lines (middle panel in Fig. 6.10) is less straightforward. The o-H_2O 179.5μm line shows a stronger increase in flux than both the 180.5μm line, which is at higher excitation, and the 538.3μm line, which is at lower excitation. The p-H_2O 89.99μm and o-H_2O 78.7μm lines are at higher excitation, forming in the inner

disc, and these also show a large increase in flux as the dust grains settle. It is likely that the relative behaviour of the various water lines is a complex function of the changing temperature structure and H_2O chemical abundance structure in the disc, affecting the excitation of the various levels.

The largest increase in line flux occurs in the H_2 S(1) transition (Fig. 6.10; lower panel). The emission region for this line is seen to follow the 300K gas temperature contour (see Fig. 6.8), which intersects a greater molecular hydrogen mass in the settled models. This leads to a dramatic enhancement in flux in the strongly settled models, a factor of $\sim$ 30 increase on the fully mixed model. The [OI] 63 μm line also starts to increase as the smallest grains are allowed to settle, coinciding with an increase in atomic gas, but the enhancement is less extreme since this line is formed further out in the disc (see Fig. 6.8). The OH 79.11 μm line is formed at intermediate distance between H_2 S(1) and [OI] 63 μm, and its behaviour with increasing dust settling reflects this. The [CII] 158 μm line is less strongly affected by settling. This line is formed in a thin layer at the disc surface, with emission dominated by the outer disc, and so it is less sensitive to changes in the internal disc temperature structure.

The settling of dust grains might be expected to drive line formation conditions closer to LTE, with the various species residing lower in the disc, in regions of higher density, with more frequent collisions between particles. However, there is no evidence for this in my models. The majority of lines show only minor departures from LTE, in both settled and well-mixed models. The largest departure from the line fluxes assuming LTE level populations occurs in the water lines, but the LTE line fluxes increase at roughly the same rate as those computed using escape probability, so the ratio $F_{\rm NLTE}/F_{\rm LTE}$ remains roughly constant. The critical density for the water lines, $n_{\rm crit} \sim 10^8 - 10^{10}{\rm cm}^{-3}$. These densities are reached only in the inner disc in my models, with each of the lines arising in regions with $n < n_{\rm crit}$, even in the settled models. The water line which is closest to LTE in the models is the 538.3μm line, which has the lowest level of excitation and the smallest critical density. In general, the critical densities decrease rapidly at large optical depths, driving most of the transitions towards LTE.

These results are in contrast to the findings of Jonkheid et al. [2007], who find a trend of decreasing gas temperature and line emission as the dust grains are allowed to settle towards the midplane. However, a direct comparison is not appropriate, since their models assumed a simultaneous reduction in the dust/gas

ratio and PAH abundances with dust settling. The reduction in gas temperature can largely be attributed then to the drop in photoelectric heating from dust grains and PAH molecules. Jonkheid et al. [2007] also note that the dust temperatures in their models are high enough to prevent CO freeze-out, whereas considerable freeze-out is present here. Meijerink et al. [2009] also predict an increase in line emission with dust settling, from models in which the effect of settling is simulated by simply increasing the global gas/dust ratio, as opposed to considering the vertical distribution of grains in the disc.

My models indicate that the ^{13}CO 1-0 line flux can change by a factor ~ 2 in strongly settled models. This is in a high mass disc for which the line is optically thick throughout most of the disc, and so this settling flux enhancement might be expected to be even stronger in a lower mass disc. In any case, variable grain freeze-out would seem to limit the ability of this line to trace the total disc gas mass. In general, the effect of dust settling on the vertical thermal structure of the gas in discs is seen to introduce new degeneracies when attempting to fit the disc parameters to the observed line emission. While my preferred model fits the observed data with a well-mixed disc with the canonical gas/dust ratio, I cannot rule out the possibility of a gas-depleted disc in which dust settling gives an enhancement in the various line fluxes. Indeed, such a disc with gas/dust $\sim$ 20 allows a better fit to the line data and the observed 10 micron silicate emission (column 1 in Table 6.6).

6.5.3 Effect of X-rays

It is currently unclear how important a role X-rays play in determining the gas chemistry and temperature structure in discs. Aresu et al. [2011] studied the effects of stellar X-ray emission on models of T Tauri discs computed with ProDiMo. This study found that while Coulomb heating by X-rays introduced an extended hot gas surface layer to the discs, the [OI] and [CII] fine structure lines were only affected for X-ray luminosities $L_X > 10^{30}$ erg s^{-1}. One would expect this to hold for the warmer gas in Herbig discs, and Günther and Schmitt [2009] derive an X-ray luminosity of $L_X = 10^{29.6}$ erg s^{-1} for HD 163296, lower than but close to the threshold value noted by Aresu et al. [2011] for T Tauri discs. HD 163296 represents an interesting test case for the influence of X-rays in Herbig discs.

I have computed a disc model with parameters identical to my preferred model, but with an additional X-ray component in the input spectrum. The X-ray luminosity was

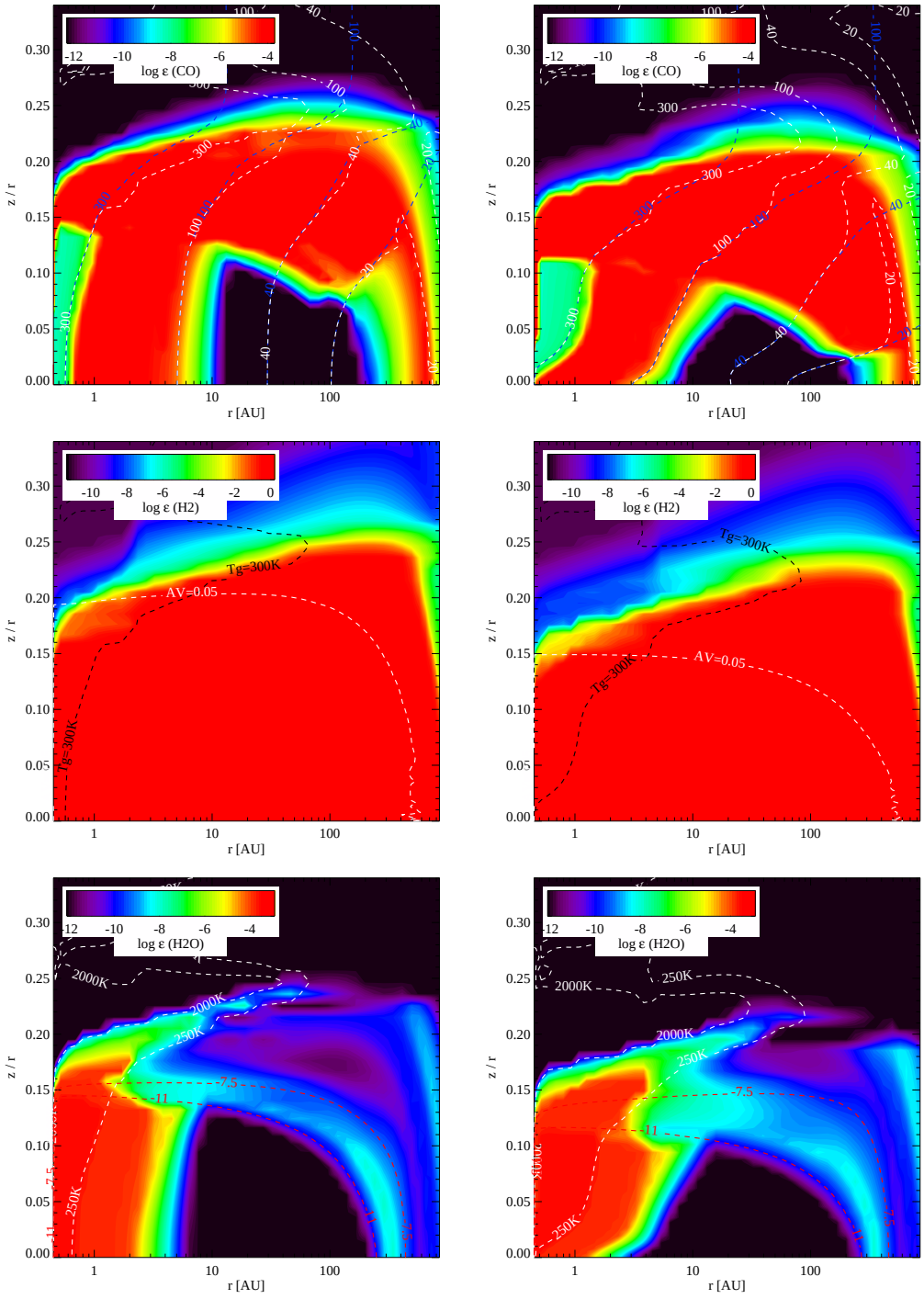

Figure 6.11: Effect of dust settling on the disc chemical abundances. Left column indicates abundances in a fully mixed model, and right column represents a strongly-settled model with otherwise identical parameters. Top row: CO abundance with dust (blue dashed lines) and gas (white dashed line) temperature contours. Middle row: H_2 abundance with 300K gas temperature contour (black dashed line) and visual extinction contour (white dashed line). Bottom row: H_2O abundance. White dashed lines indicate $T_{\rm gas}$ contours enclosing "hot water" region, red dashed lines indicate contours of UV field strength per hydrogen nucleus, $\log(\chi/n_{\rm H})$ as defined in Draine and Bertoldi [1996], enclosing the cool water belt.

set equal to the value of $L_X = 10^{29.6}$ erg s^{-1} observed by Günther and Schmitt [2009] for HD 163296. The effect of this on the gas temperature is illustrated by Fig. 6.12 (c.f. Fig. 6.7). The X-ray heating processes produce an extended hot surface gas layer, as noted by Aresu et al. [2011], with gas temperatures >5000K extending out to the outer disc.

There is little discernible effect on the disc chemistry, with none of the chemical species masses or predicted line fluxes changing by more than a few percent.In all cases the effect of the additional X-rays is less than produced by switching to the "high UV" input spectrum . I would therefore expect the UV to dominate the gas chemistry in a Herbig disc of the sort considered here.

6.6 Summary and Conclusions

This chapter presents new observations of the far-IR lines of the Herbig Ae star HD 163296, obtained using Herschel/PACS as part of the GASPS open time key program. These consist of a detection of the [OI] 63.18 μm line, as well as upper limits for eight additional lines. I have supplemented these observations with additional line and continuum data.

I have computed radiation thermo-chemical disc models using the disc code ProDiMo, and employed an evolutionary χ^2-minimisation strategy to find the best simultaneous model fit to the continuum and line data. The stellar parameters and UV input spectrum for the modelling were determined through detailed analysis in the UV, optical and near-infrared.

I obtain reasonable fits to the observed photometry, ISO-SWS spectrum, far-IR line fluxes and millimetre CO profiles for a variety of discs, and note that parameter degeneracies preclude the precise derivation of the disc properties. In particular, the effects of dust settling on the vertical thermal structure of the gas in discs strongly influence the line emission, placing further limits on the derivation of a disc gas mass from the line data. I am able to fit the photometry and line data with a well-mixed disc with gas/dust ~ 100, but an equally good fit is possible with a disc with gas/dust ~ 22, in which dust settling is present. The main advantage of the settled model is that the fit to the observed ISO-SWS spectrum is greatly improved, and it seems probable that some degree of dust settling and gas-depletion is present in the disc. These discs have a radial surface density profile as derived by Hughes et al. [2008b], with an exponentially-

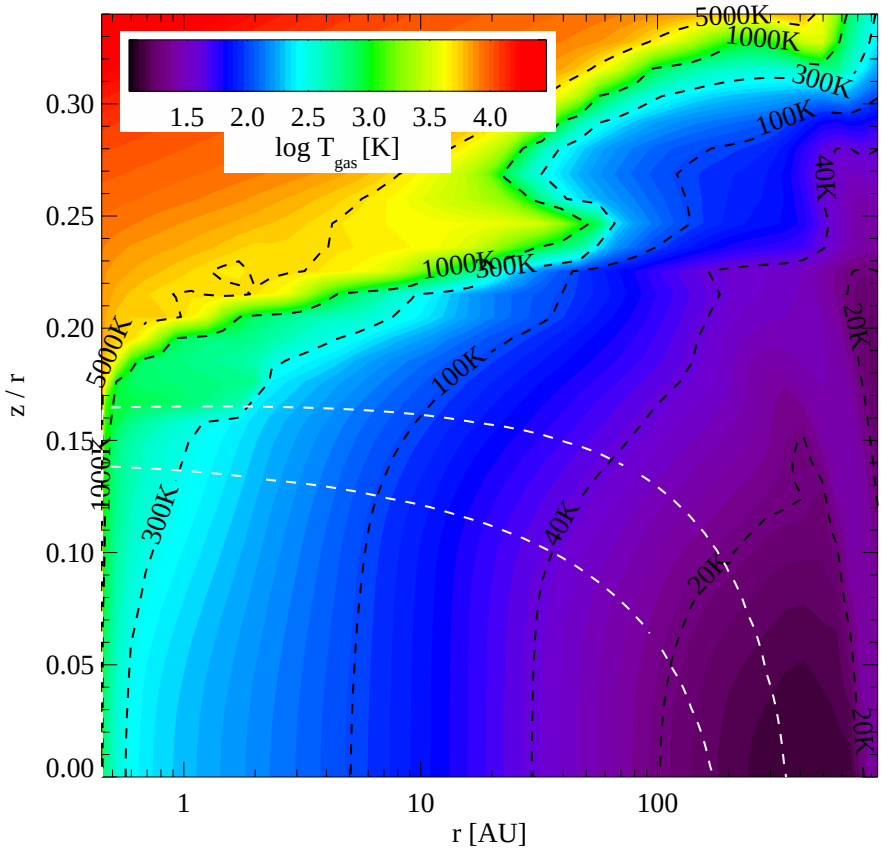

Figure 6.12: Gas temperature structure for the preferred model (column 3 in Table 6.6), irradiated by an additional X-ray spectral component with $L_X = 10^{29.6}\,\mathrm{erg\,s^{-1}}$, as observed by Günther and Schmitt [2009] in HD 163296. This is in comparison to the right hand panel of Fig. 6.7, in which no X-ray spectral component is present.

tapered outer edge.

A model fit to the same data with power-law radial density profile gives a gas/dust ratio of ~ 9. This power-law model gives the best fit to the observed SED data, although it does very badly when it comes to fitting the radial intensity distribution of the resolved millimetre continuum. This is due to the flat density power index required to fit the SED and the observed CO 3-2 emission, and presents a challenge for future modelling efforts.

The emitted line fluxes are in general sensitive to the degree of dust settling in the disc. This is a firm result in my models, and has serious implications for attempts to derive the disc gas mass and other properties from line observations. This settling flux enhancement arises from changes to the vertical temperature and chemical structure, as settled dust grains allow stellar UV to penetrate deeper into the disc. The effect is

strongest in lines which are formed in the warm gas in the inner disc (e.g. a factor ~ 30 increase in the H_2 S(1) line), but the low excitation molecular lines are also affected, e.g. a factor ~ 2 increase in the ^{13}CO 1-0 line.

I explore the effects of the observed UV variability in this object on the gas chemistry in my models, and conclude that this effect is not large enough to affect the observable line fluxes beyond the current range of instrumental uncertainty.

I also examine the effect of X-rays on the gas chemistry of the models, and find that while X-rays present a significant source of gas-heating in the disc surface layers, the observed X-ray luminosity of $L_X = 10^{29.6}$ erg s^{-1} does not significantly alter the gas chemistry or line emission. Any effects are smaller than those expected as a result of the observed UV variability in this object.

It is difficult to reach any firm conclusions regarding the evolutionary state of the disc of HD 163296. There is some evidence to suggest that the disc is gas-depleted. This is in contrast to the result found for the Herbig Ae star HD 169142 by Meeus et al. [2010], where despite indications that the disc is transitional, it was found to be gas-rich. I note that there are uncertainties associated with my gas/dust values arising from uncertainties in the disc dust composition, and the associated opacity law. This is reflected by the factor of ~ 3 spread in the range of derived dust masses found in the literature for this object [Natta et al., 2004, Tannirkulam et al., 2008a, Mannings and Sargent, 1997, Isella et al., 2007]. All of my derived dust masses are within the range $(5 - 17) \times 10^{-4} M_\odot$ from the literature. I also note the restrictions placed on my conclusions by the assumption of constant dust grain properties throughout the disc, and it has been suggested that the dust properties in discs should in general be variable with radius [Birnstiel et al., 2010, Guilloteau et al., 2011].

It would appear that the modelling of HD 163296 is a far from straightforward task, and it is difficult to fit it into the standard evolutionary picture developed over the past decade, where an initially gas-rich, strongly flaring disc gradually accretes its gas, leading to a gas-depleted non-flaring disc in which accretion has stopped. I am unable to find a single disc model which fits perfectly the entire wealth of observational data for this object. As well as the gas/dust ratio, there is uncertainty regarding the disc flaring, which itself is strongly tied in to the disc gas heating and line emission, as well as being indicative of the disc's evolutionary state. Evidence of in-falling material and the presence of a bipolar outflow in HD 163296 seem to indicate that the star is actively accreting material, typical of a young object with a gas-rich disc. However, it has been

suggested that the observed disc geometry and flaring could indicate a star at a later stage of its evolution. This would be consistent with the evidence for grain growth from my modelling, with all the models requiring large grains to fit the observations. There is also possible further evidence for particle growth from high resolution optical spectra of this object. This is consistent with possible evidence for dust settling and gas-depletion from this study, but is hard to reconcile with evidence for substantial ongoing activity in the inner disc. It is clear that this object is at a fascinating stage in its evolution.

Chapter 7

Atomic Hydrogen Modelling in ProDiMo

In this chapter I discuss developing work in which I explore the effects of modifying ProDiMo to include the bound-bound and bound-free transitions of atomic hydrogen. These modifications are outlined in Section 3.6.

7.1 Introduction

Hydrogen emission has been observed from a number of objects believed to have a circumstellar disc. Classical Be stars are B type stars which exhibit Balmer line emission, in which the hydrogen atom decays to the principal quantum number $n = 2$ level from a higher excitation level. It was suggested by Struve [1931] that the observed range of Hα line profiles could be explained by hydrogen recombination in a flattened disc. In addition, Be stars often exhibit a strong infra-red excess, typical of objects with a circumstellar disc, and the net (continuum) linear polarisation observed in Be stars can be explained by electron scattering from non-spherical circumstellar gas [Coyne and Kruszewski, 1969].

Sigut and Jones [2007] compared the observed Hα emission from the classical Be star γ-Cassiopeiae with that predicted by a circumstellar disc model. This utilised a pure gas disc with solar composition, with heating and cooling provided by a selection of atomic and ionic species, through both bound-bound and continuum transitions. The total Hα cooling rate was found to be consistent with observations. The disc thermal structure was compared with that in a pure hydrogen disc [Millar and Marlborough,

1998], and the results were found to depend largely on the assumed disc density. At low density, the solar composition discs were cooler on average than pure hydrogen discs, which was attributed to additional collisionally-excited line cooling from the heavy elements. At higher densities however, this was offset by the additional bound-free continuum absorption from these elements, leading to similar disc-averaged temperatures in both the solar composition and pure hydrogen cases.

B[e] objects are a subset of Be stars which exhibit forbidden emission lines (e.g. those of Fe, O, N), in addition to Balmer emission and a strong infra-red excess. There is often confusion regarding the precise evolutionary state of such objects [Israelian et al., 1996].

In the following I use the B[e] star HD 45677 as a case study to explore the effects of introducing the bound-bound and bound-free hydrogen transitions to ProDiMo. First though, I return to my previous model of the Herbig Ae object HD 163296.

7.2 HD 163296 Model

In order to assess the impact of the new hydrogen transitions on a familiar model, I have used a model of the disc around the Herbig Ae star HD 163296 as a basis for my tests. This object was the subject of my model-fitting efforts in Chapter 6, and I use the parameters from the "preferred" well-fitting model in that study, listed in column 3 of Table 6.6.

Figure 7.1 illustrates the effect on the gas temperature of introducing the hydrogen transitions to the model. There is a net heating effect, concentrated largely in the inner disc in the already hot gas, leading to gas temperatures $\sim 20000\,\mathrm{K}$. This can largely be attributed to photoionisation heating, and the heating effect is vastly reduced when the extreme ultra-violet (EUV; $\lambda < 91.2\,\mathrm{nm}$) intensity is set to zero. In this case it is no longer possible for the stellar UV to ionise hydrogen in the ground state, instead requiring some degree of prior excitation. The gas temperature without EUV irradiation is largely unchanged from the model without the detailed hydrogen treatment, with just a small heating effect in the disc surface, where there is some degree of hydrogen excitation.

Figure 7.2 illustrates the large ionisation cross-section presented by the hydrogen in the EUV wavelength region (to the right of the $n = 1$ absorption edge in this plot), and removing this EUV radiation reduces the degree of ionisation accordingly (see

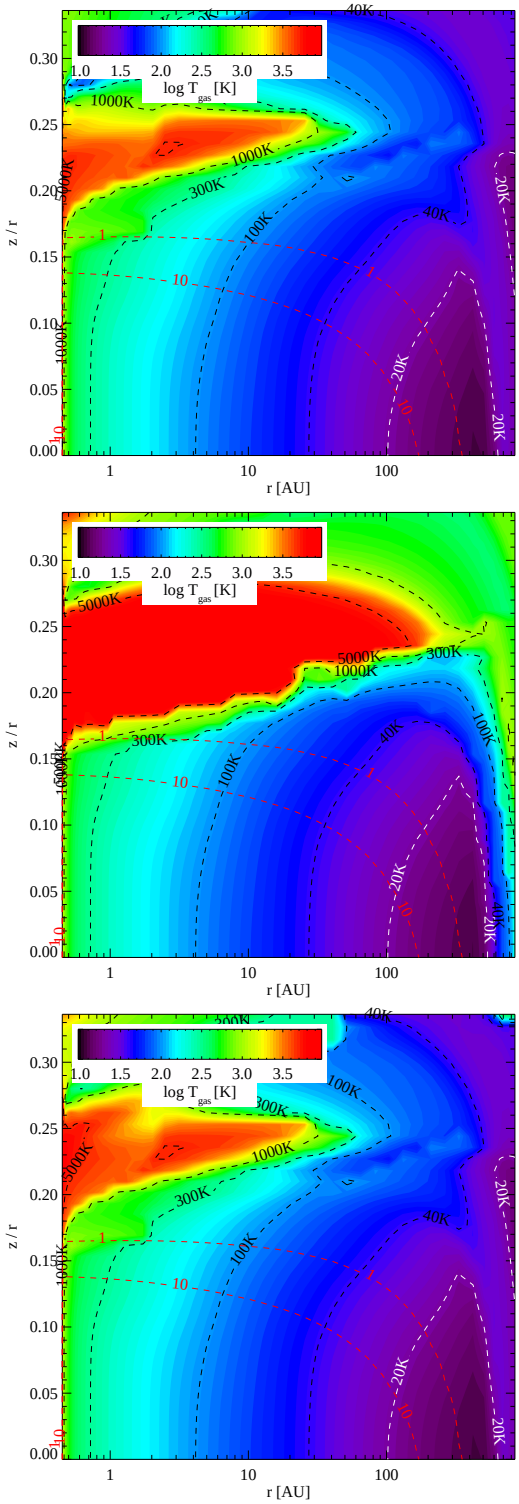

Figure 7.1: Gas temperature structure in the disc of HD 163296. Top panel: gas temperature in the absence of HI bound-bound and bound free transitions. Middle panel: including HI transitions. Bottom panel: including HI transitions, but with the EUV spectral intensity set equal to zero, i.e. $J_\lambda = 0$ for λ <91.2 nm.

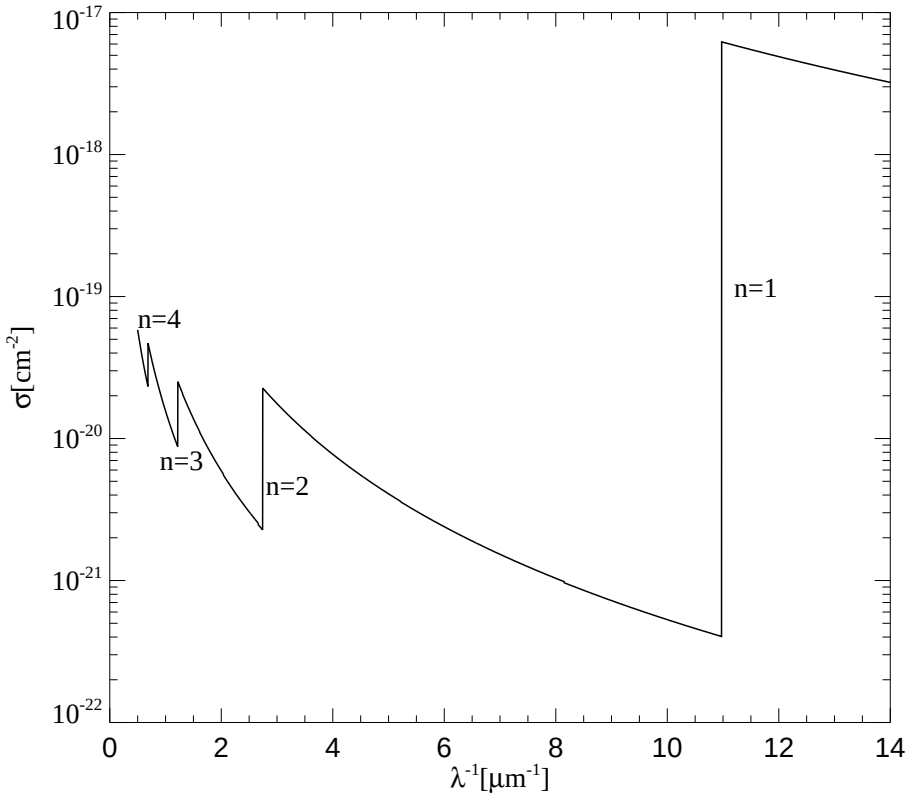

Figure 7.2: Photoionisation cross-sections for neutral hydrogen, assuming LTE level populations at 15000K. Cross-sections σ are per hydrogen atom. Absorption edges are labelled with the corresponding principal quantum number, n.

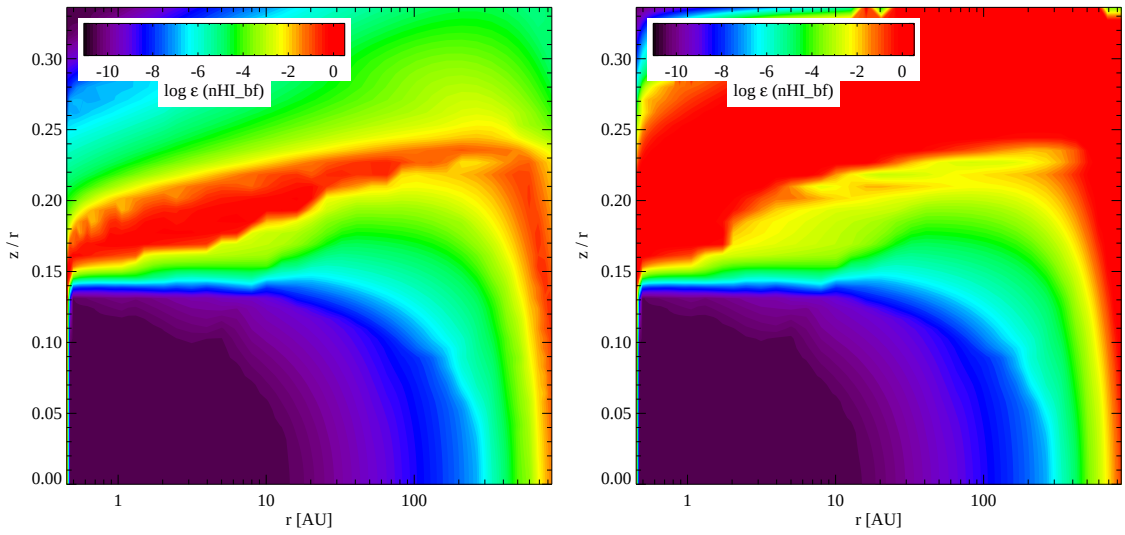

Figure 7.3: HI abundances in the HD 163296 disc model. Left panel: input spectrum including non-zero EUV intensity. Right panel: EUV intensity set to zero.

Table 7.1: HI and HII masses and mass-averaged HI temperature in the HD 163296 disc model, with both zero and non-zero EUV intensity.

	$M_{\rm HI}$	$M_{\rm HII}$	$\langle T_{\rm HI}\rangle$
$J_{\rm EUV}=0$	$2.3\times10^{-5}{\rm M}_\odot$	$1.8\times10^{-7}{\rm M}_\odot$	64 K
$J_{\rm EUV}\neq0$	$7.8\times10^{-6}{\rm M}_\odot$	$1.7\times10^{-5}{\rm M}_\odot$	1037 K

Figure 7.3 and Table 7.2). In the absence of EUV the hydrogen is almost entirely neutral, with < 1% of the disc hydrogen mass consisting of ionised gas. The mass-averaged hydrogen temperature is also strongly weighted in favour of the cold gas in the outer disc. With EUV irradiation, the ionisation mass fraction increases to ~ 70%, and the remaining HI resides in the hot gas in the upper disc layers, giving a hydrogen temperature ~ 1000 K.

7.3 HD 45677 Model

In addition to the existing HD 163296 disc model, I have used the B[e] star HD 45677 to further assess the impact of my modifications. The ISO-SWS spectrum for this object contains a number of Brackett and Pfund emission lines, allowing us to compare the model with observational data. Also, the increased stellar luminosity and temperature in comparison to HD 163296 provide a contrasting disc environment in which to study the hydrogen transitions.

The model parameters are listed in Table 7.2. They were derived from a fit to the observed SED performed by Wing-Fai Thi. The disc is assumed to have a gas/dust ratio of 100. The disc structure is solved fully self-consistently over several "global" iterations, as was the case in Chapter 4 (but not Chapters 5 & 6).

The gas density and temperature structure are shown in Figure 7.4. The observed SED is fit by a relatively low mass disc, with lower densities than the HD 163296 model (c.f. Figure 6.7). This, coupled with strong irradiation by the central star, leads to gas temperatures ~ 5000 K throughout the entire disc. This result also largely holds in the absence of the detailed hydrogen treatment, although with slightly lower temperature in the upper surface layers.

The self-consistent structure determination leads to a disc which is puffed-up to an enormous height, with the scale height $H \sim R$ outwards of ~ 20 AU. The model contains hardly any H_2, and instead exhibits a smooth linear transition from HI abundances ~ 1 at small z through to HII abundances ~ 1 in the upper disc (see Figure 7.5). The nature

Table 7.2: Parameters of the HD 45677 model.

Quantity	Symbol	Value
stellar mass	$M_\star$	$10.4\,M_\odot$
effective temperature	$T_{\rm eff}$	21850 K
stellar luminosity	$L_\star$	$7310\,L_\odot$
disc mass	$M_{\rm disc}$	1.0×10^{-3}
inner disc radius	$R_{\rm in}$	4.4 AU [(1)]
outer disc radius	$R_{\rm out}$	200 AU
radial column density power index	ϵ	1.0
dust-to-gas mass ratio	ρ_d/ρ	0.01
minimum dust particle radius	$a_{\rm min}$	$1.5\,\mu$m
maximum dust particle radius	$a_{\rm max}$	$1000\,\mu$m
dust size distribution power index	$a_{\rm pow}$	3.5
dust material mass density	$\rho_{\rm gr}$	$3.5\,{\rm g\,cm^{-3}}$
strength of incident ISM UV	$\chi^{\rm ISM}$	1
cosmic ray ionization rate of H_2	$\zeta_{\rm CR}$	1.7×10^{-17} s^{-1}
abundance of PAHs relative to ISM	$f_{\rm PAH}$	0.1
α viscosity parameter	α	0.0

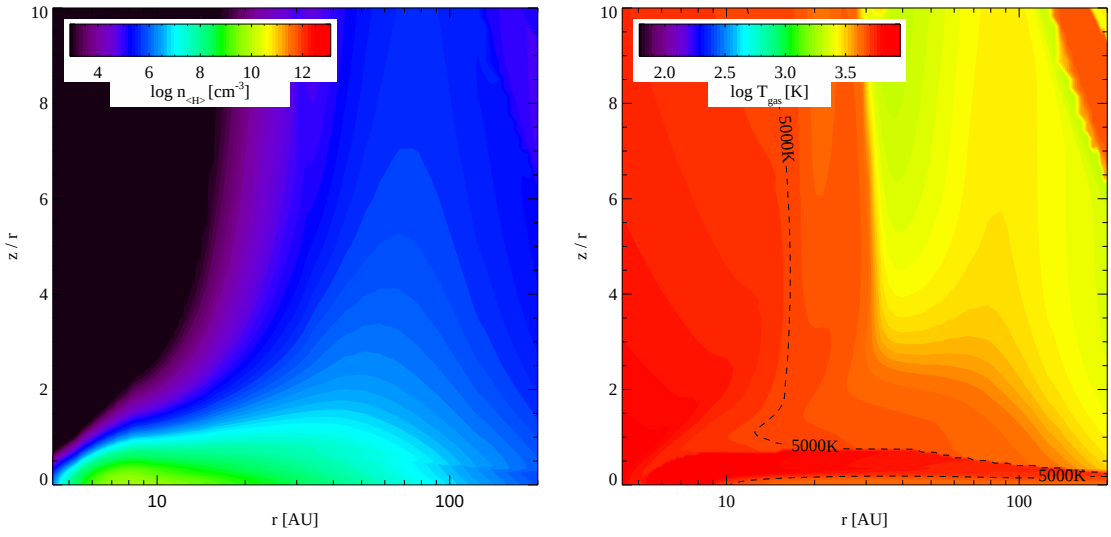

Figure 7.4: Total hydrogen nuclei density (left panel) and gas temperature (right panel) in a model of the disc surrounding HD 45677.

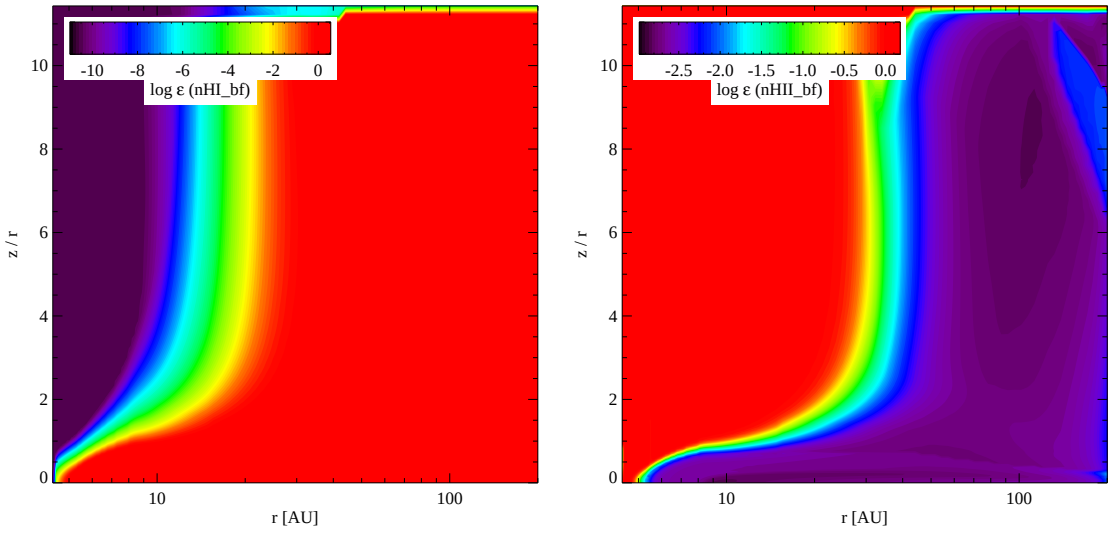

Figure 7.5: HI (left panel) and HII (right panel) abundances in the HD 45677 disc model.

of the hydrogen cooling across this transition can be seen in Figure 7.6, which plots several bound-bound and bound-free cooling rates as a fraction of the total radiative hydrogen cooling rate for a vertical slice through the disc. The cooling is dominated by the Lyman-continuum recombination cooling, and to a lesser extent by Lyman-α cooling. The Lyman-α cooling rate increases in the tenuous disc surface layers, to the detriment of the continuum cooling, but drops off steeply in the high density disc midplane. Generally the bound-free continuum cooling dominates in the high density regions, at low z, while the bound-bound cooling takes over at the disc surface. This is due to the increasing optical depth in the hydrogen lines with increasing gas density. The Hα line (n=3-2) is less strongly affected by optical depth effects since it doesn't involve the ground state. The Hα cooling therefore drops off less rapidly than Lyman-α and Lyman-β at small z, and there is a peak in emission at around $z = 5$-10 AU corresponding to a warm region with higher excitation of the n=3 level.

7.3.1 Comparison with observations

Figure 7.7 plots the observed ISO-SWS spectrum of HD 45677. The Brackett series 5-4 and 6-4 lines, and the Pfund series 6-5, 7-5 and 8-5 lines are clearly visible. The higher level Pfund series lines, and the Humphreys series (n=6), which also occur in this wavelength range, are not observed. The observed lines are all several orders of

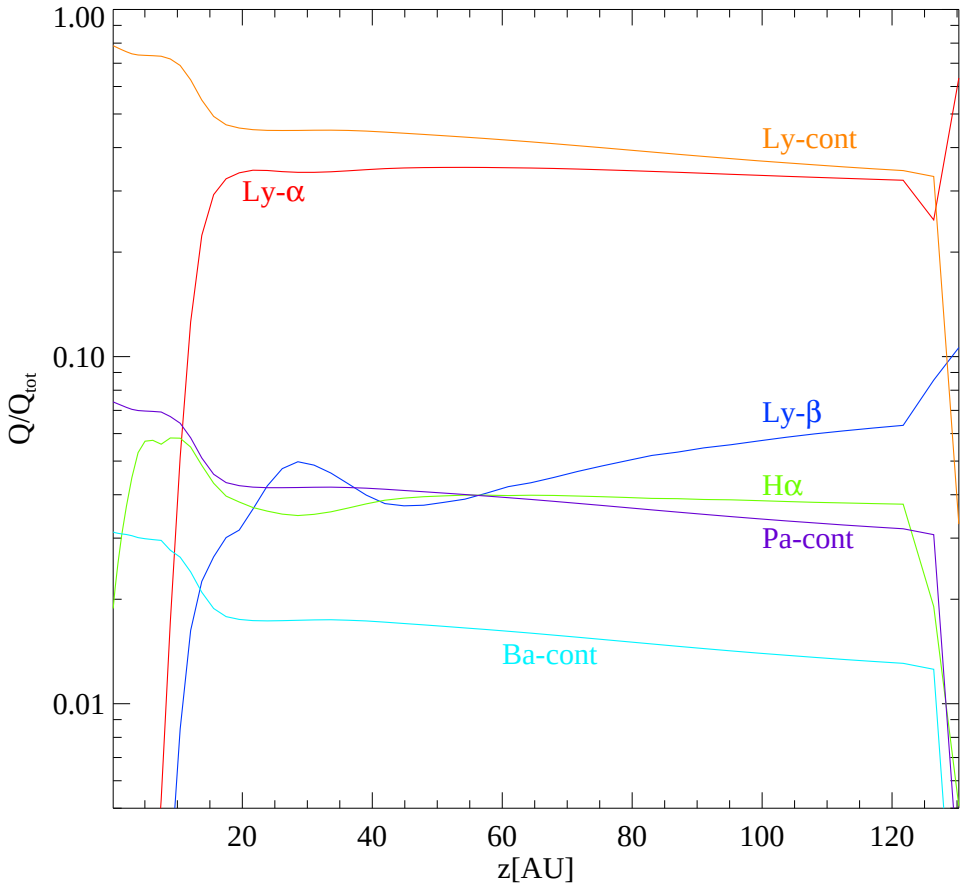

Figure 7.6: Neutral hydrogen cooling rates, as a fraction of the total radiative hydrogen cooling rate, for a vertical disc cross-section at a radius of 10 AU.

Table 7.3: Predicted hydrogen line fluxes from three disc models. The first has gas/dust = 100 and EUV intensity set to zero. The second is the same but with non-zero EUV. The third has non-zero EUV and gas/dust = 1000. The observed fluxes from the ISO-SWS spectrum are also given. All fluxes in W/m^2.

Line	u	l	λ [mic]	g/d=100,EUV=0	g/d=100,EUV≠0	g/d=1000,EUV≠0	Obs. flux
Br-α	5	4	4.05	1.3×10^{-14}	1.7×10^{-12}	2.9×10^{-12}	8.7×10^{-7}
Br-β	6	4	2.62	1.0×10^{-14}	3.0×10^{-12}	7.1×10^{-12}	1.0×10^{-6}
Pf-α	6	5	7.46	2.0×10^{-15}	5.2×10^{-13}	9.6×10^{-13}	5.2×10^{-7}
Pf-β	7	5	4.65	2.0×10^{-15}	1.5×10^{-12}	3.2×10^{-12}	6.7×10^{-7}
Pf-γ	8	5	3.74	1.5×10^{-15}	1.5×10^{-12}	4.0×10^{-12}	2.0×10^{-7}

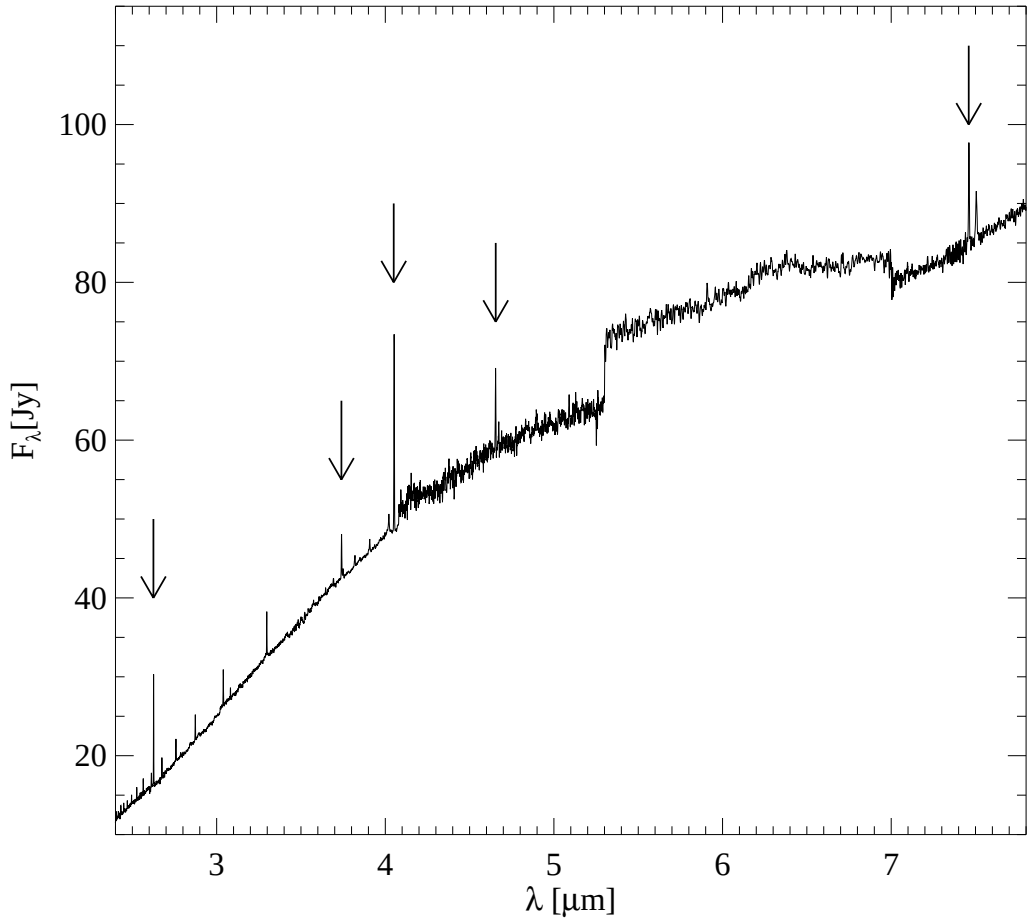

Figure 7.7: Partial ISO-SWS spectrum for HD 45677. Marked with arrows are the hydrogen emission lines: the Brackett series lines n=5-4 at 4.05 μm and n=6-4 at 2.62 μm and the Pfund series lines n=6-5 (7.46 μm), n=7-5 (4.65 μm) and n=8-5 (3.74 μm).

magnitude brighter than predicted by the models, and so it is clear that this preliminary modelling approach is unable to constrain the disc properties at present.

Introducing stellar EUV to the models leads to an increase in line flux by $\sim$2-3 orders of magnitude, with the higher excitation lines showing the largest increase. This can be attributed to the higher excitation lines being more sensitive to the increase in gas temperature caused by adding the EUV spectral component. Increasing the gas/dust ratio of the EUV-irradiated models then leads to a further brightening of the lines by a factor ~ 2, with the enhancement factor again increasing slightly with line excitation. This behaviour is consistent with the lines being optically thick, with a factor of 10 increase in gas mass leading to a factor ~ 2 increase in flux. It also suggests that the line optical depth decreases with increasing line excitation.

HD 45677 is a poorly understood object, with uncertainty regarding both its evolutionary state and its physical structure. Analysis of optical forbidden emission lines led Swings [1973] to suggest that HD 45677 is in fact a young post-main-sequence object surrounded by a dust shell. Grady et al. [1993] claimed that the IUE spectrum and IR excess of this object could be explained by a massive HAeBe star with an actively accreting protoplanetary disc, whereas the photometric observations of de Winter and van den Ancker [1997] led them to claim that HD 45677 is a main sequence star. This is in agreement with the findings of Israelian et al. [1996] from observations of the Balmer lines and the lines of He I and Si II. These two studies also agreed that the observations are best-explained by the presence of a circumstellar disc seen edge-on, whereas the presence of single-peaked Fe II and Cr II emission lines led Muratorio et al. [2006] to claim that the disc is in fact viewed almost face-on. There is also a large degree of spectral variability [de Winter and van den Ancker, 1997], and evidence for a wind [Israelian et al., 1996].

It is clearly a great challenge to attempt to fit the observed infra-red hydrogen lines, especially if this were combined with other observational data seemingly arising from a disc. It seems unlikely that this will be possible using the current model of a single continuous disc, with constant dust and gas properties with radius. One approach might be to include a separate gas disc inwards of the dust inner radius, in order to fit the broad observed emission lines (FWHM ~ 300 km/s) while still being in agreement with the observed dust SED. This would also be consistent with the picture of a disc which is actively accreting gas, with potential for a pure gas disc inwards of the dust sublimation radius.

7.4 Summary and Conclusions

I have used the Herbig Ae object HD 163296 and the B[e] object HD 45677 as case studies with which to assess the effects of introducing the bound-bound and bound-free transitions of atomic hydrogen to ProDiMo. The results are found to be strongly dependent on the EUV intensity, with a net heating effect which is strongly reduced in the absence of the spectral EUV component. This presents a challenge for future modelling efforts, since it is unclear to what extent the stellar EUV should be expected to irradiate the disc gas. Absorption by intermediate circumstellar material would strongly attenuate the EUV intensity, and so care must be taken when attempting to model the disc hydrogen emission.

Self-consistent models of HD 45677 lead to vertically extended discs with hot gas (~ 5000 K) throughout, with very little H_2 present. The hydrogen cooling is dominated by the Lyman-α line and Lyman-continuum, with the line emission dominant in the tenuous surface layers, and the continuum taking over at higher densities, where the lines are optically thick.

The Brackett and Pfund series line fluxes predicted by the models are several orders of magnitude lower than observed in the ISO-SWS spectrum of HD 45677. The behaviour of the lines with increasing disc gas mass indicates that they are optically thick, with the lower excitation lines showing the greatest degree of saturation with increasing gas mass. It seems unlikely that a continuous disc model such as this will be able to fit simultaneously the observed SED and infra-red hydrogen lines, and I suggest that further tests involving multiple zones (e.g. an inner gas disc) would be an illuminating way to proceed following these preliminary modelling efforts.

Chapter 8

Conclusions

Protoplanetary discs are key to our understanding of planet formation. It is of great interest to the astronomical community to be able to use observational data to infer the disc properties. In particular, knowing the amount of gas present in discs at different stages in their evolution allows us to constrain and distinguish between different models of planet formation. Also, the thermal and chemical structure in the disc dictate the conditions in the planets which eventually arise from its gas and dust.

There are a wealth of observational data which allow us to study discs, from young gas-rich discs to debris discs, in which the gas has been used up by planet formation, gradually photoevaporated away by the intense stellar radiation, or accreted on to the central star. The Herschel Space Observatory has allowed us to study the disc gas with greater sensitivity than ever. The far-infrared emission lines which Herschel traces provide a powerful analytical tool, allowing us to break degeneracies between existing dust continuum and millimetre CO observations. This relies however on detailed modelling of the disc thermal and chemical structure, in order to predict the observed line emission, and compare this with Herschel and other data.

I have used the radiation thermo-chemical disc code ProDiMo to explore the extent to which observations are able to constrain the disc properties. This has involved a number of different approaches, from seeking general statistical trends across a large sample of disc models, to focussing on the specific physical processes at work in individual objects. This body of work is consistent, however, in its aim to assess the power of observations, coupled with modelling, in piecing together the disc jigsaw puzzle.

The first stage in this process is to compute a limited series of Herbig Ae disc

models with increasing mass, in order to study the origin and diagnostic value of the gas line tracers [C II], [O I] and CO. The Monte-Carlo radiative transfer code RATRAN is used to compute line profiles and integrated emission from various gas lines. This line emission is compared with that computed using an escape probability formalism, and with the assumption of LTE level populations. The [C II] 157.7 μm line is found to originate in the disc surface layer, where gas and dust temperatures are decoupled. The total line strength is dominated by emission from the disc outer radius, and so the 157.7 μm line probes mainly the disc extension and outer disc gas temperature. The line forms in LTE. The [O I] lines are also found to originate in the disc surface layer, albeit somewhat deeper than the [C II] line. The main contribution to the [O I] emission comes from radii between 30 and 100 AU. The [O I] lines form partially under non-LTE conditions. Differences in line emission from escape probability and Monte Carlo techniques are smaller than 10%.

The CO sub-mm lines in the models are found to be optically thick down to very low disc masses of $< 10^{-4}$ $M_{\odot}$. These lines are formed mostly in LTE. The assumption of thermal gas-dust coupling such that $T_{\rm gas} = T_{\rm dust}$, is not a valid approximation for these lines. Differences in line emission from escape probability and Monte Carlo techniques are smaller than 3%, except in the case of very optically thin disc models (10^{-5} and 10^{-6} $M_{\odot}$).

The [O I] 63/145 μm and [O I] 63/[C II] 158 μm line ratios trace disc mass in the regime between 10^{-2} and 10^{-6} $M_{\odot}$. Since the [C II] 158 μm line is very sensitive to the outer disc radius, the [O I] 63/[C II] 158 μm is degenerate in that respect and its use requires additional constraints from ancilliary gas and/or dust observations. The sensitivity of these two line ratios to the dust grain sizes underlines the importance of using SED constraints along with the gas modelling to mitigate the uncertainty of dust properties. A combination of the [O I] 63/145 μm and [O I] 63/[C II] 158 μm line ratios can be used to reduce the degeneracy caused by an unknown outer disc radius.

The CO lines are not found to be a good gas tracer; neither the total CO sub-mm line fluxes nor line ratios can be used to measure the disc mass. However, these low rotational CO lines provide an excellent tool to measure the disc outer radius, and can thus help to break the degeneracy between gas mass and outer radius found for the [O I] 63/[C II] 158 μm line ratio.

Following on from this small-scale study, varying the gas mass incrementally along a series of models, this approach has been expanded to a huge multi-dimensional

analysis. A grid of ~300000 models has been computed, spanning parameter space, in order to seek trends across the various models, and compare the model predictions with the findings of a large survey of the gas in circumstellar discs. I have acted as the main developer of `xDENT`, a graphical user interface for analysing and plotting the huge quantity of grid data, and for fitting the model data to observations.

In addition to its use as an analytical and interpretive tool, `xDENT` has been used to produce figures for a number of publications concerning the model grid data. The principle aim of these studies is to seek parameter dependencies, so as to invert these dependencies and infer the disc properties from observations. The calculated line emission is found to be strongly dependent on the assumed stellar UV excess and disc flaring, as well as other less general dependencies. The grid results highlight considerable parameter degeneracies, meaning that care must be taken when attempting to interpret line observations and invert them into physical parameters. It is necessary to combine the far-IR line observations with with other line and continuum data, in order to break these degeneracies, and it is this strategy which I follow during the next phase of my work.

Having reached the practical limit of the statistical approach followed thus far, with computational and model constraints preventing the grid analysis from being extended much further, I instead move on to focus on modelling the disc of a single object. By carrying out detailed model fitting to a large number of observational data from an individual target, my aim has been to derive the disc properties, with a hope that such a detailed approach will yield some further understanding of the physical processes driving the observable trends that we see. For these purposes I have used the Herbig Ae star HD 163296, a well-studied object with a large number of available line and continuum observations. These include new observations of the far-IR lines, obtained using Herschel/PACS as part of the GASPS open time key program.

I have computed radiation thermo-chemical disc models using ProDiMo, and employed an evolutionary χ^2-minimisation strategy to find the best simultaneous model fit to the observed continuum and line data. The stellar parameters and UV input spectrum for the modelling have been determined through detailed analysis in the UV, optical and near-infrared.

I obtain reasonable fits to the observed photometry, ISO-SWS spectrum, far-IR line fluxes and millimetre CO profiles for a variety of discs, and note that parameter degeneracies preclude the precise derivation of the disc properties. In particular, the

effects of dust settling on the vertical thermal structure of the gas in discs strongly influence the line emission, placing further limits on the derivation of a disc gas mass from the line data. I am able to fit the photometry and line data with a well-mixed disc with gas/dust ~ 100, but an equally good fit is possible with a disc with gas/dust ~ 22, in which dust settling is present. The main advantage of the settled model is that the fit to the observed ISO-SWS spectrum is greatly improved, and it seems probable that some degree of dust settling and gas-depletion is present in the disc. These discs have a radial surface density profile as derived by Hughes et al. [2008b], with an exponentially-tapered outer edge.

A model fit to the same data with power-law radial density profile gives a gas/dust ratio of ~ 9. This power-law model gives the best fit to the observed SED data, although it does very badly when it comes to fitting the radial intensity distribution of the resolved millimetre continuum. This is due to the flat density power index required to fit the SED and the observed CO 3-2 emission, and presents a challenge for future modelling efforts.

The emitted line fluxes are in general sensitive to the degree of dust settling in the disc. This is a firm result in my models, and has serious implications for attempts to derive the disc gas mass and other properties from line observations. This settling flux enhancement arises from changes to the vertical temperature and chemical structure, as settled dust grains allow stellar UV to penetrate deeper into the disc. The effect is strongest in lines which are formed in the warm gas in the inner disc (e.g. a factor ~ 30 increase in the H_2 S(1) line), but the low excitation molecular lines are also affected, e.g. a factor ~ 2 increase in the ^{13}CO 1-0 line.

I explore the effects of the observed UV variability in this object on the gas chemistry in my models, and conclude that this effect is not large enough to affect the observable line fluxes beyond the current range of instrumental uncertainty.

I also examine the effect of X-rays on the gas chemistry of the models, and find that while X-rays present a significant source of gas-heating in the disc surface layers, the observed X-ray luminosity of $L_X = 10^{29.6}$ erg s^{-1} does not significantly alter the gas chemistry or line emission. Any effects are smaller than those expected as a result of the observed UV variability in this object.

It is difficult to reach any firm conclusions regarding the evolutionary state of the disc of HD 163296. There is some evidence to suggest that the disc is gas-depleted. This is in contrast to the result found for the Herbig Ae star HD 169142 by Meeus

et al. [2010], where despite indications that the disc is transitional, it was found to be gas-rich. I note that there are uncertainties associated with my gas/dust values arising from uncertainties in the disc dust composition, and the associated opacity law. This is reflected by the factor of ~ 3 spread in the range of derived dust masses found in the literature for this object [Natta et al., 2004, Tannirkulam et al., 2008a, Mannings and Sargent, 1997, Isella et al., 2007]. All of my derived dust masses are within the range $(5 - 17) \times 10^{-4} M_{\odot}$ from the literature. I also note the restrictions placed on my conclusions by the assumption of constant dust grain properties throughout the disc, and it has been suggested that the dust properties in discs should in general be variable with radius [Birnstiel et al., 2010, Guilloteau et al., 2011].

It is difficult to fit HD 163296 into the standard evolutionary picture developed over the past decade. I am unable to find a single disc model which fits perfectly the entire wealth of observational data for this object. As well as the gas/dust ratio, there is uncertainty regarding the disc flaring, which itself is strongly tied in to the disc gas heating and line emission, as well as being indicative of the disc's evolutionary state. Evidence of in-falling material and the presence of a bipolar outflow in HD 163296 seem to indicate that the star is actively accreting material, typical of a young object with a gas-rich disc. However, it has been suggested that the observed disc geometry and flaring could indicate a star at a later stage of its evolution. This would be consistent with the evidence for grain growth from my modelling, with all the models requiring large grains to fit the observations. There is also possible further evidence for particle growth from high resolution optical spectra of this object. This is consistent with possible evidence for dust settling and gas-depletion from this study, but is hard to reconcile with evidence for substantial ongoing activity in the inner disc.

My final approach has been to focus-in still further, and study the contribution of a single gas species to the disc heating and cooling balance. I have modified the ProDiMo code to include the bound-bound and bound-free transitions of atomic hydrogen, and attempted to assess the impact of these changes. This is developing work, and further testing and analysis is necessary before drawing any firm conclusions from the results.

In addition to the existing model of HD 163296, I have used the B[e] object HD 45677 as a case study with which to explore the effects of introducing the new hydrogen transitions to ProDiMo. The results are found to be strongly dependent on the EUV intensity, with a net heating effect which is strongly reduced in the absence

of the spectral EUV component. This presents a challenge for future modelling efforts, since it is unclear to what extent the stellar EUV should be expected to irradiate the disc gas. Absorption by intermediate circumstellar material would strongly attenuate the EUV intensity, and so care must be taken when attempting to model the disc hydrogen emission.

Self-consistent models of HD 45677 lead to vertically extended discs with hot gas (~ 5000 K) throughout, with very little H_2 present. The hydrogen cooling is dominated by the Lyman-α line and Lyman-continuum, with the line emission dominant in the tenuous surface layers, and the continuum taking over at higher densities, where the lines are optically thick.

The Brackett and Pfund series line fluxes predicted by the models are several orders of magnitude lower than observed in the ISO-SWS spectrum of HD 45677. The behaviour of the lines with increasing disc gas mass indicates that they are optically thick, with the lower excitation lines showing the greatest degree of saturation with increasing gas mass.

It is clear from my modelling efforts that I was justified in my original assertion that studying the gas in protoplanetary discs offers a much more powerful probe of the disc conditions than focussing merely on the dust emission. But with great power comes great responsibility, and it is important to bear in mind the implications of this expanded analysis. From a modelling perspective, including the gas introduces a whole host of potential parameter degeneracies. This is most obvious in my model fits to observations of HD 163296, where reasonable fits to the same set of data were possible with quite different model parameters. This is similar to the findings of Woitke et al. [2011] for the T Tauri star RECX 15. In particular, the variation of the line fluxes with dust settling in my models presents a significant obstacle in terms of deriving disc gas masses from observations.

Another challenge highlighted by my models of HD 163296, and hinted at by my preliminary work studying HD 45677, is the difficulty in trying to fit numerous observations simultaneously with a single continuous disc model. It is unlikely that discs in nature would be so well-behaved, and so it is desirable to introduce more complex models, with multiple disc zones, and gas and dust properties varying with radius. But this in turn introduces further parameter degeneracies, and it seems appropriate to urge caution when claiming a precise derivation of the disc properties in such a scenario. Even so, this will be an important next step and a focus for further

study. The other obvious line of study is to continue my work on the atomic hydrogen transitions. This will have to include a detailed analysis of the stellar EUV, and its effect on a wide range of disc models, as well as looking at the influence of X-rays, and explaining the gulf between the observed hydrogen emission and that predicted by the models in their current form.

Bibliography

E. Abrahamsson, R. V. Krems, and A. Dalgarno. Fine-Structure Excitation of O I and C I by Impact with Atomic Hydrogen. *The Astrophysical Journal*, 654:1171–1174, January 2007. doi: 10.1086/509631.

B. Acke, J. Bouwman, A. Juhász, T. Henning, M. E. van den Ancker, G. Meeus, A. G. G. M. Tielens, and L. B. F. M. Waters. Spitzer's View on Aromatic and Aliphatic Hydrocarbon Emission in Herbig Ae Stars. *The Astrophysical Journal*, 718:558–574, July 2010. doi: 10.1088/0004-637X/718/1/558.

F. C. Adams, C. J. Lada, and F. H. Shu. Spectral evolution of young stellar objects. *The Astrophysical Journal*, 312:788–806, January 1987. doi: 10.1086/164924.

G. Aresu, I. Kamp, R. Meijerink, P. Woitke, W.-F. Thi, and M. Spaans. X-ray impact on the protoplanetary disks around T Tauri stars. *Astronomy and Astrophysics*, 526:A163+, February 2011. doi: 10.1051/0004-6361/201015449.

H. H. Aumann. IRAS observations of matter around nearby stars. *Astronomical Society of the Pacific*, 97:885–891, October 1985. doi: 10.1086/131620.

E. H. Avrett and D. G. Hummer. Non-coherent scattering, II: Line formation with a frequency independent source function. *Monthly Notices of the Royal Astronomical Society*, 130:295–+, 1965.

R. J. Barber, J. Tennyson, G. J. Harris, and R. N. Tolchenov. A high-accuracy computed water line list. *Monthly Notices of the Royal Astronomical Society*, 368:1087–1094, May 2006. doi: 10.1111/j.1365-2966.2006.10184.x.

S. Beckwith, A. I. Sargent, N. Z. Scoville, C. R. Masson, B. Zuckerman, and T. G. Phillips. Small-scale structure of the circumstellar gas of HL Tauri and R Monocerotis. *The Astrophysical Journal*, 309:755–761, October 1986. doi: 10.1086/164645.

S. V. W. Beckwith and A. I. Sargent. Particle emissivity in circumstellar disks. *The Astrophysical Journal*, 381:250–258, November 1991. doi: 10.1086/170646.

S. V. W. Beckwith, A. I. Sargent, R. S. Chini, and R. Guesten. A survey for circumstellar disks around young stellar objects. *The Astronomical Journal*, 99:924–945, March 1990. doi: 10.1086/115385.

K. L. Bell, K. A. Berrington, and M. R. J. Thomas. Electron impact excitation of the ground-state ˆ3P fine-structure levels in atomic oxygen. *Monthly Notices of the Royal Astronomical Society*, 293:L83–L87, February 1998. doi: 10.1046/j.1365-8711.1998.01364.x.

K. R. Bell, P. M. Cassen, H. H. Klahr, and T. Henning. The Structure and Appearance of Protostellar Accretion Disks: Limits on Disk Flaring. *The Astrophysical Journal*, 486:372–+, September 1997. doi: 10.1086/304514.

M. Benisty, A. Natta, A. Isella, J.-P. Berger, F. Massi, J.-B. Le Bouquin, A. Mérand, G. Duvert, S. Kraus, F. Malbet, J. Olofsson, S. Robbe-Dubois, L. Testi, M. Vannier, and G. Weigelt. Strong near-infrared emission in the sub-AU disk of the Herbig Ae star HD 163296: evidence of refractory dust? *Astronomy and Astrophysics*, 511:A74+, February 2010. doi: 10.1051/0004-6361/200912898.

M. S. Bessell. UBVRI photometry. II - The Cousins VRI system, its temperature and absolute flux calibration, and relevance for two-dimensional photometry. *Publications of the Astronomical Society of the Pacific*, 91:589–607, October 1979. doi: 10.1086/130542.

T. Birnstiel, C. P. Dullemond, and F. Brauer. Gas- and dust evolution in protoplanetary disks. *Astronomy and Astrophysics*, 513:A79+, April 2010. doi: 10.1051/0004-6361/200913731.

J. Bouwman, A. de Koter, M. E. van den Ancker, and L. B. F. M. Waters. The composition of the circumstellar dust around the Herbig Ae stars AB Aur and HD 163296. *Astronomy and Astrophysics*, 360:213–226, August 2000.

I. Brott and P. H. Hauschildt. A PHOENIX Model Atmosphere Grid for Gaia. In C. Turon, K. S. O'Flaherty, and M. A. C. Perryman, editors, *The Three-Dimensional Universe with Gaia*, volume 576 of *ESA Special Publication*, pages 565–+, January 2005.

N. Calvet, A. Patino, G. C. Magris, and P. D'Alessio. Irradiation of accretion disks around young objects. I - Near-infrared CO bands. *The Astrophysical Journal*, 380:617–630, October 1991. doi: 10.1086/170618.

G. Chambaud, B. Levy, P. Millie, E. Roueff, and F. Tran Minh. *Journal of Physics B Atomic Molecular Physics*, 13:4205, 1980.

E. I. Chiang and P. Goldreich. Spectral Energy Distributions of T Tauri Stars with Passive Circumstellar Disks. *The Astrophysical Journal*, 490:368–+, November 1997. doi: 10.1086/304869.

S.-I. Chu and A. Dalgarno. The rotational excitation of carbon monoxide by hydrogen atom impact. *Royal Society of London Proceedings Series A*, 342:191–207, February 1975. doi: 10.1098/rspa.1975.0020.

M. Clampin, J. E. Krist, D. R. Ardila, D. A. Golimowski, G. F. Hartig, H. C. Ford, G. D. Illingworth, F. Bartko, N. Benítez, J. P. Blakeslee, R. J. Bouwens, T. J. Broadhurst, R. A. Brown, C. J. Burrows, E. S. Cheng, N. J. G. Cross, P. D. Feldman, M. Franx, C. Gronwall, L. Infante, R. A. Kimble, M. P. Lesser, A. R. Martel, F. Menanteau, G. R. Meurer, G. K. Miley, M. Postman, P. Rosati, M. Sirianni, W. B. Sparks, H. D. Tran, Z. I. Tsvetanov,

R. L. White, and W. Zheng. Hubble Space Telescope ACS Coronagraphic Imaging of the Circumstellar Disk around HD 141569A. *The Astronomical Journal*, 126:385–392, July 2003. doi: 10.1086/375460.

A. N. Cox, editor. *Allen's Astrophysical Quantities*. Springer-Verlag New York, fourth edition, 1999.

G. V. Coyne and A. Kruszewski. Wavelength dependence of polarization. XVII. Be-type stars. *The Astronomical Journal*, 74:528–532, May 1969. doi: 10.1086/110830.

M. J. Creech-Eakman, E. I. Chiang, R. M. K. Joung, G. A. Blake, and E. F. van Dishoeck. ISO LWS Spectra of T Tauri and Herbig AeBe stars. *Astronomy and Astrophysics*, 385:546–562, April 2002. doi: 10.1051/0004-6361:20020157.

W. Cunto, C. Mendoza, F. Ochsenbein, and C. J. Zeippen. Topbase at the CDS. *Astronomy and Astrophysics*, 275:L5, August 1993.

M. C. Cushing, W. D. Vacca, and J. T. Rayner. Spextool: A Spectral Extraction Package for SpeX, a 0.8-5.5 Micron Cross-Dispersed Spectrograph. *Publications of the Astronomical Society of the Pacific*, 116:362–376, April 2004. doi: 10.1086/382907.

P. D'Alessio, J. Canto, N. Calvet, and S. Lizano. Accretion Disks around Young Objects. I. The Detailed Vertical Structure. *The Astrophysical Journal*, 500:411–+, June 1998. doi: 10.1086/305702.

P. D'Alessio, N. Calvet, L. Hartmann, S. Lizano, and J. Cantó. Accretion Disks around Young Objects. II. Tests of Well-mixed Models with ISM Dust. *The Astrophysical Journal*, 527: 893–909, December 1999. doi: 10.1086/308103.

E. Dartois, A. Dutrey, and S. Guilloteau. Structure of the DM Tau Outer Disk: Probing the vertical kinetic temperature gradient. *Astronomy and Astrophysics*, 399:773–787, February 2003. doi: 10.1051/0004-6361:20021638.

D. de Winter and M. E. van den Ancker. The peculiar B[e] star HD 45677. II. Photometric behaviour and spectroscopic properties. *Astronomy and Astrophysics Supplement Series*, 121:275–299, February 1997. doi: 10.1051/aas:1997320.

D. de Winter, M. E. van den Ancker, A. Maira, P. S. Thé, H. R. E. T. A. Djie, I. Redondo, C. Eiroa, and F. J. Molster. A photometric catalogue of southern emission-line stars. *Astronomy and Astrophysics*, 380:609–614, December 2001. doi: 10.1051/0004-6361:20011476.

W. R. F. Dent, J. S. Greaves, and I. M. Coulson. CO emission from discs around isolated HAeBe and Vega-excess stars. *Monthly Notices of the Royal Astronomical Society*, 359: 663–676, May 2005. doi: 10.1111/j.1365-2966.2005.08938.x.

D. Devine, C. A. Grady, R. A. Kimble, B. Woodgate, F. C. Bruhweiler, A. Boggess, J. L. Linsky, and M. Clampin. A Lyα Bright Jet from a Herbig AE Star. *The Astrophysical Journal Letters*, 542:L115–L118, October 2000. doi: 10.1086/312939.

J. Dorschner, B. Begemann, T. Henning, C. Jaeger, and H. Mutschke. Steps toward interstellar silicate mineralogy. II. Study of Mg-Fe-silicate glasses of variable composition. *Astronomy and Astrophysics*, 300:503–+, August 1995.

C. Doucet, E. Pantin, P. O. Lagage, and C. P. Dullemond. Mid-infrared imaging of the circumstellar dust around three Herbig Ae stars: HD 135344, CQ Tau, and HD 163296. *Astronomy and Astrophysics*, 460:117–124, December 2006. doi: 10.1051/0004-6361:20054371.

B. T. Draine and F. Bertoldi. Structure of Stationary Photodissociation Fronts. *The Astrophysical Journal*, 468:269–+, September 1996. doi: 10.1086/177689.

B. T. Draine and H. M. Lee. Optical properties of interstellar graphite and silicate grains. *The Astrophysical Journal*, 285:89–108, October 1984. doi: 10.1086/162480.

M.-L. Dubernet and A. Grosjean. Collisional excitation rates of H_2O with H_2 . I. Pure rotational excitation rates with para-H_2 at very low temperature. *Astronomy and Astrophysics*, 390: 793–800, August 2002. doi: 10.1051/0004-6361:20020800.

C. P. Dullemond, G. J. van Zadelhoff, and A. Natta. Vertical structure models of T Tauri and Herbig Ae/Be disks. *Astronomy and Astrophysics*, 389:464–474, July 2002. doi: 10.1051/0004-6361:20020608.

A. Dutrey, S. Guilloteau, and M. Guelin. Chemistry of protosolar-like nebulae: The molecular content of the DM Tau and GG Tau disks. *Astronomy and Astrophysics*, 317:L55–L58, January 1997.

C. Eiroa, F. Garzón, A. Alberdi, D. de Winter, R. Ferlet, C. A. Grady, A. Cameron, J. K. Davies, H. J. Deeg, A. W. Harris, K. Horne, B. Merín, L. F. Miranda, B. Montesinos, A. Mora, R. Oudmaijer, J. Palacios, A. Penny, A. Quirrenbach, H. Rauer, J. Schneider, E. Solano, Y. Tsapras, and P. R. Wesselius. EXPORT: Near-IR observations of Vega-type and pre-main sequence stars. *Astronomy and Astrophysics*, 365:110–114, January 2001. doi: 10.1051/0004-6361:20000029.

J. A. Eisner, J. R. Graham, R. L. Akeson, and J. Najita. Spatially Resolved Spectroscopy of Sub-AU-Sized Regions of T Tauri and Herbig Ae/Be Disks. *The Astrophysical Journal*, 692: 309–323, February 2009. doi: 10.1088/0004-637X/692/1/309.

A. Faure, N. Crimier, C. Ceccarelli, P. Valiron, L. Wiesenfeld, and M. L. Dubernet. Quasi-classical rate coefficient calculations for the rotational (de)excitation of H{2}O by H{2}. *Astronomy and Astrophysics*, 472:1029–1035, September 2007. doi: 10.1051/0004-6361:20077678.

D. A. Fischer and J. Valenti. The Planet-Metallicity Correlation. *The Astrophysical Journal*, 622:1102–1117, April 2005. doi: 10.1086/428383.

E. L. Fitzpatrick. Correcting for the Effects of Interstellar Extinction. *Publications of the Astronomical Society of the Pacific*, 111:63–75, January 1999. doi: 10.1086/316293.

B. P. Flannery, W. Roberge, and G. B. Rybicki. The penetration of diffuse ultraviolet radiation into interstellar clouds. *The Astrophysical Journal*, 236:598–608, March 1980. doi: 10.1086/157778.

D. R. Flower. *Journal of Physics B Atomic Molecular Physics*, 34:2731–2738, 2001.

D. R. Flower and J. M. Launay. Molecular collision processes. II - Excitation of the fine-structure transition of C/+/ in collisions with H2. *Journal of Physics B Atomic Molecular Physics*, 10:3673–3681, December 1977. doi: 10.1088/0022-3700/10/18/024.

V. C. Geers, J.-C. Augereau, K. M. Pontoppidan, C. P. Dullemond, R. Visser, J. E. Kessler-Silacci, N. J. Evans, II, E. F. van Dishoeck, G. A. Blake, A. C. A. Boogert, J. M. Brown, F. Lahuis, and B. Merín. C2D Spitzer-IRS spectra of disks around T Tauri stars. II. PAH emission features. *Astronomy and Astrophysics*, 459:545–556, November 2006. doi: 10.1051/0004-6361:20064830.

V. C. Geers, E. F. van Dishoeck, K. M. Pontoppidan, F. Lahuis, A. Crapsi, C. P. Dullemond, and G. A. Blake. Lack of PAH emission toward low-mass embedded young stellar objects. *Astronomy & Astrophysics*, 495:837–846, March 2009. doi: 10.1051/0004-6361:200811001.

A. E. Glassgold and W. D. Langer. The C/+/-CO transition in interstellar clouds. *The Astrophysical Journal*, 197:347–350, April 1975. doi: 10.1086/153519.

A. E. Glassgold and J. R. Najita. The Effects of X-Rays on the Diffuse Gas in Protoplanetary Disks. In R. Jayawardhana and T. Greene, editors, *Young Stars Near Earth: Progress and Prospects*, volume 244 of *Astronomical Society of the Pacific Conference Series*, pages 251–+, 2001.

C. A. Grady, K. S. Bjorkman, D. Shepherd, R. E. Schulte-Ladbeck, M. R. Perez, D. de Winter, and P. S. The. Detection of accreting gas toward HD 45677 - A newly recognized, Herbig Be proto-planetary system. *The Astrophysical Journal Letters*, 415:L39–L42, September 1993. doi: 10.1086/187027.

C. A. Grady, D. Devine, B. Woodgate, R. Kimble, F. C. Bruhweiler, A. Boggess, J. L. Linsky, P. Plait, M. Clampin, and P. Kalas. STIS Coronagraphic Imaging of the Herbig AE Star: HD 163296. *The Astrophysical Journal*, 544:895–902, December 2000. doi: 10.1086/317222.

S. Green, S. Maluendes, and A. D. McLean. Improved collisional excitation rates for interstellar water. *The Astrophysical Journal Supplement Series*, 85:181–185, March 1993. doi: 10.1086/191760.

S. Guilloteau, A. Dutrey, V. Piétu, and Y. Boehler. A dual-frequency sub-arcsecond study of proto-planetary disks at mm wavelengths: first evidence for radial variations of the dust properties. *Astronomy and Astrophysics*, 529:A105+, May 2011. doi: 10.1051/0004-6361/201015209.

H. M. Günther and J. H. M. M. Schmitt. The enigmatic X-rays from the Herbig star HD 163296: Jet, accretion, or corona? *Astronomy and Astrophysics*, 494:1041–1051, February 2009. doi: 10.1051/0004-6361:200811007.

T. J. Harries. Synthetic line profiles of rotationally distorted hot-star winds. *Monthly Notices of the Royal Astronomical Society*, 315:722–734, July 2000. doi: 10.1046/j.1365-8711.2000.03505.x.

T. J. Harries, J. D. Monnier, N. H. Symington, and R. Kurosawa. Three-dimensional dust radiative-transfer models: the Pinwheel Nebula of WR 104. *Monthly Notices of the Royal Astronomical Society*, 350:565–574, May 2004. doi: 10.1111/j.1365-2966.2004.07668.x.

L. Hartmann. *Accretion Processes in Star Formation*. June 1998.

T. Henning, B. Begemann, H. Mutschke, and J. Dorschner. Optical properties of oxide dust grains. *Astronomy and Astrophysics Supplement Series*, 112:143–+, July 1995.

F. Hersant, V. Wakelam, A. Dutrey, S. Guilloteau, and E. Herbst. Cold CO in circumstellar disks. On the effects of photodesorption and vertical mixing. *Astronomy & Astrophysics*, 493:L49–L52, January 2009. doi: 10.1051/0004-6361:200811082.

M. R. Hogerheijde and F. F. S. van der Tak. An accelerated Monte Carlo method to solve two-dimensional radiative transfer and molecular excitation. With applications to axisymmetric models of star formation. *Astronomy and Astrophysics*, 362:697–710, October 2000.

D. J. Hollenbach, M. W. Werner, and E. E. Salpeter. Molecular Hydrogen in H i Regions. *The Astrophysical Journal*, 163:165–+, January 1971. doi: 10.1086/150755.

A. M. Hughes, D. J. Wilner, I. Kamp, and M. R. Hogerheijde. A Resolved Molecular Gas Disk around the Nearby A Star 49 Ceti. *The Astrophysical Journal*, 681:626–635, July 2008a. doi: 10.1086/588520.

A. M. Hughes, D. J. Wilner, C. Qi, and M. R. Hogerheijde. Gas and Dust Emission at the Outer Edge of Protoplanetary Disks. *The Astrophysical Journal*, 678:1119–1126, May 2008b. doi: 10.1086/586730.

A. M. Hughes, D. J. Wilner, S. M. Andrews, C. Qi, and M. R. Hogerheijde. Empirical Constraints on Turbulence in Protoplanetary Accretion Disks. *The Astrophysical Journal*, 727:85–+, February 2011. doi: 10.1088/0004-637X/727/2/85.

A. Isella, L. Testi, A. Natta, R. Neri, D. Wilner, and C. Qi. Millimeter imaging of HD 163296: probing the disk structure and kinematics. *Astronomy and Astrophysics*, 469:213–222, July 2007. doi: 10.1051/0004-6361:20077385.

G. Israelian, M. Friedjung, J. Graham, G. Muratorio, C. Rossi, and D. de Winter. The atmospheric variations of the peculiar B[e] star HD 45677 (FS Canis Majoris). *Astronomy and Astrophysics*, 311:643–650, July 1996.

C. Jager, H. Mutschke, and T. Henning. Optical properties of carbonaceous dust analogues. *Astronomy and Astrophysics*, 332:291–299, April 1998.

P. Jankowski and K. Szalewicz. *J. Chem. Phys.*, 123:104301, 2005.

R. Jaquet, V. Staemmler, M. D. Smith, and D. R. Flower. Excitation of the fine-structure transitions of O(ˆ3P_j) in collisions with ortho- and para-H_2. *Journal of Physics B Atomic Molecular Physics*, 25:285–297, 1992. doi: 10.1088/0953-4075/25/1/030.

B. Jonkheid, C. P. Dullemond, M. R. Hogerheijde, and E. F. van Dishoeck. Chemistry and line emission from evolving Herbig Ae disks. *Astronomy and Astrophysics*, 463:203–216, February 2007. doi: 10.1051/0004-6361:20065668.

I. Kamp and F. Bertoldi. CO in the circumstellar disks of Vega and beta Pictoris. *Astronomy and Astrophysics*, 353:276–286, January 2000.

I. Kamp and C. P. Dullemond. The Gas Temperature in the Surface Layers of Protoplanetary Disks. *The Astrophysical Journal*, 615:991–999, November 2004. doi: 10.1086/424703.

I. Kamp and G.-J. van Zadelhoff. On the gas temperature in circumstellar disks around A stars. *Astronomy and Astrophysics*, 373:641–656, July 2001. doi: 10.1051/0004-6361:20010629.

I. Kamp, C. P. Dullemond, M. Hogerheijde, and J. E. Enriquez. Chemistry and Line Emission of Outer Protoplanetary Disks. In D. C. Lis, G. A. Blake, and E. Herbst, editors, *Astrochemistry: Recent Successes and Current Challenges*, volume 231 of *IAU Symposium*, pages 377–386, 2005. doi: 10.1017/S1743921306007393.

I. Kamp, I. Tilling, P. Woitke, W.-F. Thi, and M. Hogerheijde. Radiation thermo-chemical models of protoplanetary disks. II. Line diagnostics. *Astronomy and Astrophysics*, 510: A18+, January 2010. doi: 10.1051/0004-6361/200913076.

I. Kamp, P. Woitke, C. Pinte, I. Tilling, W.-F. Thi, F. Menard, G. Duchene, and J.-C. Augereau. Continuum and line modelling of discs around young stars. II. Line diagnostics for GASPS from the DENT grid. *Astronomy and Astrophysics*, 532:A85+, August 2011. doi: 10.1051/0004-6361/201016399.

S. J. Kenyon and L. Hartmann. Spectral energy distributions of T Tauri stars - Disk flaring and limits on accretion. *The Astrophysical Journal*, 323:714–733, December 1987. doi: 10.1086/165866.

D. W. Koerner, A. I. Sargent, and S. V. W. Beckwith. A rotating gaseous disk around the T Tauri star GM Aurigae. *Icarus*, 106:2–+, November 1993. doi: 10.1006/icar.1993.1154.

J. M. Launay and E. Roueff. Fine structure excitation of carbon and oxygen by atomic hydrogen impact. *Astronomy and Astrophysics*, 56:289–292, April 1977.

Y. H. Le Teuff, T. J. Millar, and A. J. Markwick. The UMIST database for astrochemistry 1999. *Astronomy and Astrophysics Supplement Series*, 146:157–168, October 2000. doi: 10.1051/aas:2000265.

D. Lorenzetti, T. Giannini, B. Nisini, M. Benedettini, D. Elia, L. Campeggio, and F. Strafella. The complete far infrared spectroscopic survey of Herbig AeBe stars obtained by ISO-LWS. *Astronomy and Astrophysics*, 395:637–645, November 2002. doi: 10.1051/0004-6361:20020977.

D. Lynden-Bell and J. E. Pringle. The evolution of viscous discs and the origin of the nebular variables. *MNRAS*, 168:603–637, September 1974.

F. Malbet, R. Lachaume, and J.-L. Monin. The vertical structure of T Tauri accretion disks. II. Physical conditions in the disk. *Astronomy and Astrophysics*, 379:515–528, November 2001. doi: 10.1051/0004-6361:20011339.

V. Mannings. Submillimetre Observations of Herbig Ae/be Systems. *Monthly Notices of the Royal Astronomical Society*, 271:587–+, December 1994.

V. Mannings and J. P. Emerson. Dust in discs around T Tauri stars: Grain growth? *Monthly Notices of the Royal Astronomical Society*, 267:361–378, March 1994.

V. Mannings and A. I. Sargent. A High-Resolution Study of Gas and Dust around Young Intermediate-Mass Stars: Evidence for Circumstellar Disks in Herbig AE Systems. *The Astrophysical Journal*, 490:792–+, December 1997. doi: 10.1086/304897.

V. Mannings, D. W. Koerner, and A. I. Sargent. A rotating disk of gas and dust around a young counterpart to β Pictoris. *Nature*, 388:555–557, August 1997. doi: 10.1038/41505.

C. Martin-Zaïdi, J.-C. Augereau, F. Ménard, J. Olofsson, A. Carmona, C. Pinte, and E. Habart. Where is the warm H_2? A search for H_2 emission from disks around Herbig Ae/Be stars. *Astronomy and Astrophysics*, 516:A110+, June 2010. doi: 10.1051/0004-6361/200913776.

N. J. Mayne and T. J. Harries. On the properties of discs around accreting brown dwarfs. *Monthly Notices of the Royal Astronomical Society*, 409:1307–1329, December 2010. doi: 10.1111/j.1365-2966.2010.17400.x.

N. J. Mayne, T. J. Harries, J. Rowe, and D. M. Acreman. Bayesian fitting of Taurus brown dwarf spectral energy distributions. *ArXiv e-prints*, March 2012.

G. Meeus, L. B. F. M. Waters, J. Bouwman, M. E. van den Ancker, C. Waelkens, and K. Malfait. ISO spectroscopy of circumstellar dust in 14 Herbig Ae/Be systems: Towards an understanding of dust processing. *Astronomy and Astrophysics*, 365:476–490, January 2001. doi: 10.1051/0004-6361:20000144.

G. Meeus, C. Pinte, P. Woitke, B. Montesinos, I. Mendigutía, P. Riviere-Marichalar, C. Eiroa, G. S. Mathews, B. Vandenbussche, C. D. Howard, A. Roberge, G. Sandell, G. Duchêne, F. Ménard, C. A. Grady, W. R. F. Dent, I. Kamp, J. C. Augereau, W. F. Thi, I. Tilling, J. M. Alacid, S. Andrews, D. R. Ardila, G. Aresu, D. Barrado, S. Brittain, D. R. Ciardi, W. Danchi, D. Fedele, I. de Gregorio-Monsalvo, A. Heras, N. Huelamo, A. Krivov, J. Lebreton, R. Liseau, C. Martin-Zaidi, A. Mora, M. Morales-Calderon, H. Nomura, E. Pantin, I. Pascucci, N. Phillips, L. Podio, D. R. Poelman, S. Ramsay, B. Riaz, K. Rice, E. Solano, H. Walker, G. J. White, J. P. Williams, and G. Wright. Gas in the protoplanetary

disc of HD 169142: Herschel's view. *Astronomy and Astrophysics*, 518:L124+, July 2010. doi: 10.1051/0004-6361/201014557.

J. Meijer, C. Dominik, A. de Koter, C. P. Dullemond, R. van Boekel, and L. B. F. M. Waters. A parameter study of self-consistent disk models around Herbig AeBe stars. *Astronomy and Astrophysics*, 492:451–461, December 2008. doi: 10.1051/0004-6361:20077967.

R. Meijerink, A. E. Glassgold, and J. R. Najita. Atomic Diagnostics of X-Ray-Irradiated Protoplanetary Disks. *The Astrophysical Journal*, 676:518–531, March 2008. doi: 10.1086/527411.

R. Meijerink, K. M. Pontoppidan, G. A. Blake, D. R. Poelman, and C. P. Dullemond. Radiative Transfer Models of Mid-Infrared H_2O Lines in the Planet-Forming Region of Circumstellar Disks. *The Astrophysical Journal*, 704:1471–1481, October 2009. doi: 10.1088/0004-637X/704/2/1471.

D. Mihalas. *Stellar atmospheres /2nd edition/*. San Francisco, W. H. Freeman and Co., 1978. 650 p., 1978.

C. E. Millar and J. M. Marlborough. Rates of Energy Gain and Loss in the Circumstellar Envelopes of Be Stars: The Poeckert-Marlborough Model. *The Astrophysical Journal*, 494: 715, February 1998. doi: 10.1086/305229.

M. Min, C. P. Dullemond, C. Dominik, A. de Koter, and J. W. Hovenier. Radiative transfer in very optically thick circumstellar disks. *Astronomy and Astrophysics*, 497:155–166, April 2009. doi: 10.1051/0004-6361/200811470.

M. Min, H. Canovas, G. D. Mulders, and C. U. Keller. The effects of disk and dust structure on observed polarimetric images of protoplanetary disks. *Astronomy and Astrophysics*, 537: A75, January 2012. doi: 10.1051/0004-6361/201117333.

J. D. Monnier, J.-P. Berger, R. Millan-Gabet, W. A. Traub, F. P. Schloerb, E. Pedretti, M. Benisty, N. P. Carleton, P. Haguenauer, P. Kern, P. Labeye, M. G. Lacasse, F. Malbet, K. Perraut, M. Pearlman, and M. Zhao. Few Skewed Disks Found in First Closure-Phase Survey of Herbig Ae/Be Stars. *The Astrophysical Journal*, 647:444–463, August 2006. doi: 10.1086/505340.

B. Montesinos, C. Eiroa, A. Mora, and B. Merín. Parameters of Herbig Ae/Be and Vega-type stars. *Astronomy and Astrophysics*, 495:901–917, March 2009. doi: 10.1051/0004-6361:200810623.

G. Muratorio, C. Rossi, and M. Friedjung. Analysis of the circumstellar environment of the B[e] star HD 45677 (FS Canis Majoris). *Astronomy and Astrophysics*, 450:593–606, May 2006. doi: 10.1051/0004-6361:20053338.

J. R. Najita, J. S. Carr, A. E. Glassgold, and J. A. Valenti. Gaseous Inner Disks. In B. Reipurth, D. Jewitt, and K. Keil, editors, *Protostars and Planets V*, pages 507–522, 2007.

A. Natta, L. Testi, R. Neri, D. S. Shepherd, and D. J. Wilner. A search for evolved dust in Herbig Ae stars. *Astronomy and Astrophysics*, 416:179–186, March 2004. doi: 10.1051/0004-6361:20035620.

V. Ossenkopf and T. Henning. Dust opacities for protostellar cores. *Astronomy and Astrophysics*, 291:943–959, November 1994.

R. D. Oudmaijer, J. Palacios, C. Eiroa, J. K. Davies, D. de Winter, R. Ferlet, F. Garzón, C. A. Grady, A. Cameron, H. J. Deeg, A. W. Harris, K. Horne, B. Merín, L. F. Miranda, B. Montesinos, A. Mora, A. Penny, A. Quirrenbach, H. Rauer, J. Schneider, E. Solano, Y. Tsapras, and P. R. Wesselius. EXPORT: Optical photometry and polarimetry of Vega-type and pre-main sequence stars. *Astronomy and Astrophysics*, 379:564–578, November 2001. doi: 10.1051/0004-6361:20011331.

O. Panić and M. R. Hogerheijde. Characterising discs around Herbig Ae/Be stars through modeling of low-J ^{12}CO lines. *Astronomy and Astrophysics*, 0:in preparation, 0 2009.

O. Panić, M. R. Hogerheijde, D. Wilner, and C. Qi. Gas and dust mass in the disc around the Herbig Ae star HD 169142. *Astronomy and Astrophysics*, 491:219–227, November 2008. doi: 10.1051/0004-6361:20079261.

V. Piétu, S. Guilloteau, and A. Dutrey. Sub-arcsec imaging of the AB Aur molecular disk and envelope at millimeter wavelengths: a non Keplerian disk. *Astronomy and Astrophysics*, 443:945–954, December 2005. doi: 10.1051/0004-6361:20042050.

V. Piétu, A. Dutrey, and S. Guilloteau. Probing the structure of protoplanetary disks: a comparative study of DM Tau, LkCa 15, and MWC 480. *Astronomy and Astrophysics*, 467:163–178, May 2007. doi: 10.1051/0004-6361:20066537.

C. Pinte, F. Ménard, G. Duchêne, and P. Bastien. Monte Carlo radiative transfer in protoplanetary disks. *Astronomy and Astrophysics*, 459:797–804, December 2006. doi: 10.1051/0004-6361:20053275.

C. Pinte, D. L. Padgett, F. Ménard, K. R. Stapelfeldt, G. Schneider, J. Olofsson, O. Panić, J. C. Augereau, G. Duchêne, J. Krist, K. Pontoppidan, M. D. Perrin, C. A. Grady, J. Kessler-Silacci, E. F. van Dishoeck, D. Lommen, M. Silverstone, D. C. Hines, S. Wolf, G. A. Blake, T. Henning, and B. Stecklum. Probing dust grain evolution in IM Lupi's circumstellar disc. Multi-wavelength observations and modelling of the dust disc. *Astronomy and Astrophysics*, 489:633–650, October 2008. doi: 10.1051/0004-6361:200810121.

C. Pinte, P. Woitke, F. Ménard, G. Duchêne, I. Kamp, G. Meeus, G. Mathews, C. D. Howard, C. A. Grady, W.-F. Thi, I. Tilling, J.-C. Augereau, W. R. F. Dent, J. M. Alacid, S. Andrews, D. R. Ardila, G. Aresu, D. Barrado, S. Brittain, D. R. Ciardi, W. Danchi, C. Eiroa, D. Fedele, I. de Gregorio-Monsalvo, A. Heras, N. Huelamo, A. Krivov, J. Lebreton, R. Liseau, C. Martin-Zaïdi, I. Mendigutía, B. Montesinos, A. Mora, M. Morales-Calderon, H. Nomura, E. Pantin, I. Pascucci, N. Phillips, L. Podio, D. R. Poelman, S. Ramsay, B. Riaz, K. Rice, P. Riviere-Marichalar, A. Roberge, G. Sandell, E. Solano, B. Vandenbussche, H. Walker, J. P. Williams, G. J. White, and G. Wright. The Herschel view of GAS in Protoplanetary Systems

(GASPS). First comparisons with a large grid of models. *Astronomy and Astrophysics*, 518: L126, July 2010. doi: 10.1051/0004-6361/201014591.

T. Posch, F. Kerschbaum, D. Fabian, H. Mutschke, J. Dorschner, A. Tamanai, and T. Henning. Infrared Properties of Solid Titanium Oxides: Exploring Potential Primary Dust Condensates. *The Astrophysical Journal Supplement Series*, 149:437–445, December 2003. doi: 10.1086/379167.

J. E. Pringle. Accretion discs in astrophysics. *Annual Review of Astronomy and Astrophysics*, 19:137–162, 1981. doi: 10.1146/annurev.aa.19.090181.001033.

J. T. Rayner, D. W. Toomey, P. M. Onaka, A. J. Denault, W. E. Stahlberger, W. D. Vacca, M. C. Cushing, and S. Wang. SpeX: A Medium-Resolution 0.8-5.5 Micron Spectrograph and Imager for the NASA Infrared Telescope Facility. *Publications of the Astronomical Society of the Pacific*, 115:362–382, March 2003. doi: 10.1086/367745.

I. Rechenberg. *Computer Methods in Applied Mechanics and Engineering*, 186:125, 2000.

B. Reipurth, A. Pedrosa, and M. T. V. T. Lago. Hα emission in pre-main sequence stars. I. an atlas of line profiles. *Astronomy and Astrophysics Supplement Series*, 120:229–256, December 1996.

S. Renard, F. Malbet, M. Benisty, E. Thiébaut, and J.-P. Berger. Milli-arcsecond images of the Herbig Ae star HD 163296. *Astronomy and Astrophysics*, 519:A26+, September 2010. doi: 10.1051/0004-6361/201014910.

J. Rodmann, T. Henning, C. J. Chandler, L. G. Mundy, and D. J. Wilner. Large dust particles in disks around T Tauri stars. *Astronomy and Astrophysics*, 446:211–221, January 2006. doi: 10.1051/0004-6361:20054038.

M. Röllig, N. P. Abel, T. Bell, F. Bensch, J. Black, G. J. Ferland, B. Jonkheid, I. Kamp, M. J. Kaufman, J. Le Bourlot, F. Le Petit, R. Meijerink, O. Morata, V. Ossenkopf, E. Roueff, G. Shaw, M. Spaans, A. Sternberg, J. Stutzki, W.-F. Thi, E. F. van Dishoeck, P. A. M. van Hoof, S. Viti, and M. G. Wolfire. A photon dominated region code comparison study. *Astronomy and Astrophysics*, 467:187–206, May 2007. doi: 10.1051/0004-6361:20065918.

A. E. Rydgren and D. S. Zak. On the spectral form of the infrared excess component in T Tauri systems. *Astronomical Society of the Pacific*, 99:141–145, February 1987. doi: 10.1086/131967.

G. Sandell, D. A. Weintraub, and M. Hamidouche. A Submillimeter Mapping Survey of Herbig AeBe Stars. *The Astrophysical Journal*, 727:26–+, January 2011. doi: 10.1088/0004-637X/727/1/26.

R. Schinke, V. Engel, U. Buck, H. Meyer, and G. H. F. Diercksen. Rate constants for rotational transitions of CO scattered by para-hydrogen. *The Astrophysical Journal*, 299:939–946, December 1985. doi: 10.1086/163760.

A. Schneider, C. Melis, and I. Song. TW HYA Association Membership and New WISE-detected Circumstellar Disks. *The Astrophysical Journal*, 754:39, July 2012. doi: 10.1088/0004-637X/754/1/39.

F. L. Schöier, F. F. S. van der Tak, E. F. van Dishoeck, and J. H. Black. An atomic and molecular database for analysis of submillimetre line observations. *Astronomy and Astrophysics*, 432: 369–379, March 2005a. doi: 10.1051/0004-6361:20041729.

F. L. Schöier, F. F. S. van der Tak, E. F. van Dishoeck, and J. H. Black. An atomic and molecular database for analysis of submillimetre line observations. *Astronomy and Astrophysics*, 432: 369–379, March 2005b. doi: 10.1051/0004-6361:20041729.

J. L. Servoin and B. Piriou. Infrared Reflectivity and Raman Scattering of Mg_2SiO_4 Single Crystal. *Physica Status Solidi (b)*, 55:677–686, February 1973.

N. I. Shakura and R. A. Syunyaev. Black holes in binary systems. Observational appearance. *Astronomy and Astrophysics*, 24:337–355, 1973.

A. M. Shaw. *Astrochemistry: from astronomy to astrobiology*. June 2006.

L. Siess, E. Dufour, and M. Forestini. An internet server for pre-main sequence tracks of low- and intermediate-mass stars. *Astronomy and Astrophysics*, 358:593–599, June 2000.

T. A. A. Sigut and C. E. Jones. The Thermal Structure of the Circumstellar Disk Surrounding the Classical Be Star γ Cassiopeiae. *The Astrophysical Journal*, 668:481–491, October 2007. doi: 10.1086/521209.

M. L. Sitko, W. J. Carpenter, R. L. Kimes, J. L. Wilde, D. K. Lynch, R. W. Russell, R. J. Rudy, S. M. Mazuk, C. C. Venturini, R. C. Puetter, C. A. Grady, E. F. Polomski, J. P. Wisnewski, S. M. Brafford, H. B. Hammel, and R. B. Perry. Variability of Disk Emission in Pre-Main-Sequence and Related Stars. I. HD 31648 and HD 163296: Isolated Herbig Ae Stars Driving Herbig-Haro Flows. *The Astrophysical Journal*, 678:1070–1087, May 2008. doi: 10.1086/529003.

R. L. Smith, K. M. Pontoppidan, E. D. Young, M. R. Morris, and E. F. van Dishoeck. High-Precision $C^{17}O$, $C^{18}O$, and $C^{16}O$ Measurements in Young Stellar Objects: Analogues for Co Self-shielding in the Early Solar System. *The Astrophysical Journal*, 701:163–175, August 2009. doi: 10.1088/0004-637X/701/1/163.

K. M. Strom, S. E. Strom, S. Edwards, S. Cabrit, and M. F. Skrutskie. Circumstellar material associated with solar-type pre-main-sequence stars - A possible constraint on the timescale for planet building. *The Astronomical Journal*, 97:1451–1470, May 1989. doi: 10.1086/115085.

O. Struve. On the Origin of Bright Lines in Spectra of Stars of Class B. *The Astrophysical Journal*, 73:94, March 1931. doi: 10.1086/143298.

J. P. Swings. Spectrographic observations of the peculiar Be star with infrared excess HD 45677. *Astronomy and Astrophysics*, 26:443–455, August 1973.

A. Tannirkulam, J. D. Monnier, T. J. Harries, R. Millan-Gabet, Z. Zhu, E. Pedretti, M. Ireland, P. Tuthill, T. ten Brummelaar, H. McAlister, C. Farrington, P. J. Goldfinger, J. Sturmann, L. Sturmann, and N. Turner. A Tale of Two Herbig Ae Stars, MWC 275 and AB Aurigae: Comprehensive Models for Spectral Energy Distribution and Interferometry. *The Astrophysical Journal*, 689:513–531, December 2008a. doi: 10.1086/592346.

A. Tannirkulam, J. D. Monnier, R. Millan-Gabet, T. J. Harries, E. Pedretti, T. A. ten Brummelaar, H. McAlister, N. Turner, J. Sturmann, and L. Sturmann. Strong Near-Infrared Emission Interior to the Dust Sublimation Radius of Young Stellar Objects MWC 275 and AB Aurigae. *The Astrophysical Journal Letters*, 677:L51–L54, April 2008b. doi: 10.1086/587873.

J. Tennyson, N. F. Zobov, R. Williamson, O. L Polyansky, and P. F. Bernath. *J. Phys. Chem. Ref. Data*, 30:735, 2001.

W. F. Thi, E. F. van Dishoeck, G. A. Blake, G. J. van Zadelhoff, J. Horn, E. E. Becklin, V. Mannings, A. I. Sargent, M. E. van den Ancker, A. Natta, and J. Kessler. H_2 and CO Emission from Disks around T Tauri and Herbig Ae Pre-Main-Sequence Stars and from Debris Disks around Young Stars: Warm and Cold Circumstellar Gas. *The Astrophysical Journal*, 561:1074–1094, November 2001. doi: 10.1086/323361.

W.-F. Thi, G.-J. van Zadelhoff, and E. F. van Dishoeck. Organic molecules in protoplanetary disks around T Tauri and Herbig Ae stars. *Astronomy and Astrophysics*, 425:955–972, October 2004. doi: 10.1051/0004-6361:200400026.

A. G. G. M. Tielens. Interstellar Polycyclic Aromatic Hydrocarbon Molecules. *Annual Review of Astronomy and Astrophysics*, 46:289–337, September 2008. doi: 10.1146/annurev.astro.46.060407.145211.

I. Tilling, P. Woitke, G. Meeus, A. Mora, B. Montesinos, P. Riviere-Marichalar, C. Eiroa, W.-F. Thi, A. Isella, A. Roberge, C. Martin-Zaidi, I. Kamp, C. Pinte, G. Sandell, W. D. Vacca, F. Ménard, I. Mendigutía, G. Duchêne, W. R. F. Dent, G. Aresu, R. Meijerink, and M. Spaans. Gas modelling in the disc of HD 163296. *ArXiv e-prints*, November 2011.

W. D. Vacca, M. C. Cushing, and J. T. Rayner. A Method of Correcting Near-Infrared Spectra for Telluric Absorption. *Publications of the Astronomical Society of the Pacific*, 115:389–409, March 2003. doi: 10.1086/346193.

M. E. van den Ancker, J. Bouwman, P. R. Wesselius, L. B. F. M. Waters, S. M. Dougherty, and E. F. van Dishoeck. ISO spectroscopy of circumstellar dust in the Herbig Ae systems AB Aur and HD 163296. *Astronomy and Astrophysics*, 357:325–329, May 2000.

E. F. van Dishoeck, B. Jonkheid, and M. C. van Hemert. Photoprocesses in protoplanetary disks. *Faraday Discussions*, May 2008.

F. van Leeuwen, editor. *Hipparcos, the New Reduction of the Raw Data*, volume 350 of *Astrophysics and Space Science Library*, 2007.

G.-J. van Zadelhoff, E. F. van Dishoeck, W.-F. Thi, and G. A. Blake. Submillimeter lines from circumstellar disks around pre-main sequence stars. *Astronomy and Astrophysics*, 377: 566–580, October 2001. doi: 10.1051/0004-6361:20011137.

J. E. Vernazza, E. H. Avrett, and R. Loeser. Structure of the solar chromosphere. III - Models of the EUV brightness components of the quiet-sun. *The Astrophysical Journal Supplement Series*, 45:635–725, April 1981. doi: 10.1086/190731.

R. Visser, E. F. van Dishoeck, and J. H. Black. The photodissociation and chemistry of CO isotopologues: applications to interstellar clouds and circumstellar disks. *ArXiv e-prints*, June 2009.

S. G. Warren and R. E. Brandt. Optical constants of ice from the ultraviolet to the microwave: A revised compilation. *Journal of Geophysical Research*, 113:D14220, 2008.

E. J. Wassell, C. A. Grady, B. Woodgate, R. A. Kimble, and F. C. Bruhweiler. An Asymmetric Outflow from the Herbig Ae Star HD 163296. *The Astrophysical Journal*, 650:985–997, October 2006. doi: 10.1086/507268.

M. Wernli, P. Valiron, A. Faure, L. Wiesenfeld, P. Jankowski, and K. Szalewicz. Improved low-temperature rate constants for rotational excitation of CO by H2. *Astronomy and Astrophysics*, 446:367–372, January 2006. doi: 10.1051/0004-6361:20053919.

N. J. Wilson and K. L. Bell. Effective collision strengths for ground-state and $2s^2 2p$-$2s2p^2$ fine-structure transitions in CII. *Monthly Notices of the Royal Astronomical Society*, 337: 1027–1034, December 2002. doi: 10.1046/j.1365-8711.2002.05982.x.

T. L. Wilson and R. Rood. Abundances in the Interstellar Medium. *Annual Review of Astronomy and Astrophysics*, 32:191–226, 1994. doi: 10.1146/annurev.aa.32.090194.001203.

J. P. Wisniewski, M. Clampin, C. A. Grady, D. R. Ardila, H. C. Ford, D. A. Golimowski, G. D. Illingworth, and J. E. Krist. The HD 163296 Circumstellar Disk in Scattered Light: Evidence of Time-Variable Self-Shadowing. *The Astrophysical Journal*, 682:548–558, July 2008. doi: 10.1086/589629.

P. Woitke, I. Kamp, and W.-F. Thi. Radiation thermo-chemical models of protoplanetary disks I. Hydrostatic disk structure and inner rim. *ArXiv e-prints*, April 2009a.

P. Woitke, W.-F. Thi, I. Kamp, and M.R. Hogerheijde. . *Astronomy and Astrophysics*, 0: accepted, June 2009b.

P. Woitke, C. Pinte, I. Tilling, F. Ménard, I. Kamp, W.-F. Thi, G. Duchêne, and J.-C. Augereau. Continuum and line modelling of discs around young stars - I. 300000 disc models for HERSCHEL/GASPS. *Monthly Notices of the Royal Astronomical Society*, 405:L26–L30, June 2010. doi: 10.1111/j.1745-3933.2010.00852.x.

P. Woitke, B. Riaz, G. Duchêne, I. Pascucci, A.-R. Lyo, W. R. F. Dent, N. Phillips, W.-F. Thi, F. Ménard, G. J. Herczeg, E. Bergin, A. Brown, A. Mora, I. Kamp, G. Aresu, S. Brittain, I. de Gregorio-Monsalvo, and G. Sandell. The unusual protoplanetary disk around the T

Tauri star ET Chamaeleontis. *Astronomy and Astrophysics*, 534:A44+, October 2011. doi: 10.1051/0004-6361/201116684.

J. Woodall, M. Agúndez, A. J. Markwick-Kemper, and T. J. Millar. The UMIST database for astrochemistry 2006. *Astronomy and Astrophysics*, 466:1197–1204, May 2007. doi: 10.1051/0004-6361:20064981.

P. M. Woods and K. Willacy. Carbon Isotope Fractionation in Protoplanetary Disks. *The Astrophysical Journal*, 693:1360–1378, March 2009. doi: 10.1088/0004-637X/693/2/1360.

C.-C. Wu, T. B. Ake, A. Boggess, R. C. Bohlin, C. L. Imhoff, A. V. Holm, Z. G. Levay, R. J. Panek, F. H. Schiffer, III, and B. E. Turnrose. The IUE ultraviolet spectral atlas. *NASA IUE Newsl., No. 22, 2+324 pp.*, 22, 1983.

C.-C. Wu, G. A. Reichert, T. B. Ake, A. Boggess, A. V. Holm, C. L. Imhoff, Y. Kondo, J. M. Mead, and S. N. Shore. International Ultraviolet Explorer (IUE) ultraviolet spectral atlas of selected astronomical objects. *NASA Reference Publication*, 1285, November 1992.

B. Yang, P. C. Stancil, N. Balakrishnan, and R. C. Forrey. Rotational Quenching of CO due to H_2 Collisions. *The Astrophysical Journal*, 718:1062–1069, August 2010. doi: 10.1088/0004-637X/718/2/1062.

S. Yi, P. Demarque, Y.-C. Kim, Y.-W. Lee, C. H. Ree, T. Lejeune, and S. Barnes. Toward Better Age Estimates for Stellar Populations: The Y^2 Isochrones for Solar Mixture. *The Astrophysical Journal Supplement Series*, 136:417–437, October 2001. doi: 10.1086/321795.

B. Zuckerman, T. Forveille, and J. H. Kastner. Inhibition of Giant Planet Formation by Rapid Gas Depletion around Young Stars. *Nature*, 373:494–+, February 1995. doi: 10.1038/373494a0.

Publications

Tilling et al., “Gas modelling in the disc of HD 163296”. In *Astronomy & Astrophysics*, 2011.

Kamp, Tilling, Woitke, Thi & Hogerheijde, “Radiation thermo-chemical models of protoplanetary disks: II. Line diagnostics”. In *Astronomy & Astrophysics*, 2010.

Woitke, Pinte, Tilling et al., “Continuum and line modelling of discs around young stars - I. 300000 disc models for HERSCHEL/GASPS”. In *Monthly Notices of the Royal Astronomical Society*, 2010.

Kamp, Woitke, Pinte, Tilling et al., “Continuum and line modeling of disks around young stars II. Line diagnostics for GASPS from the DENT grid”. In *Astronomy & Astrophysics*, 2011.

Mathews et al., “GAS in Protoplanetary Systems (GASPS). I. First results”. In *Astronomy & Astrophysics*, 2010.

Pinte et al., “The Herschel view of GAS in Protoplanetary Systems (GASPS). First comparisons with a large grid of models”. In *Astronomy & Astrophysics*, 2010.

Thi et al., “Herschel-PACS observation of the 10 Myr old T Tauri disk TW Hya. Constraining the disk gas mass”. In *Astronomy & Astrophysics*, 2010.

Meeus et al., “Gas in the protoplanetary disc of HD 169142: Herschel’s view”. In *Astronomy & Astrophysics*, 2010.